# Flow-Induced Vibrations of Fibre-Reinforced Polymer Hydraulic Gates

J. C. A. Veldhuizen

Delft University of Technology

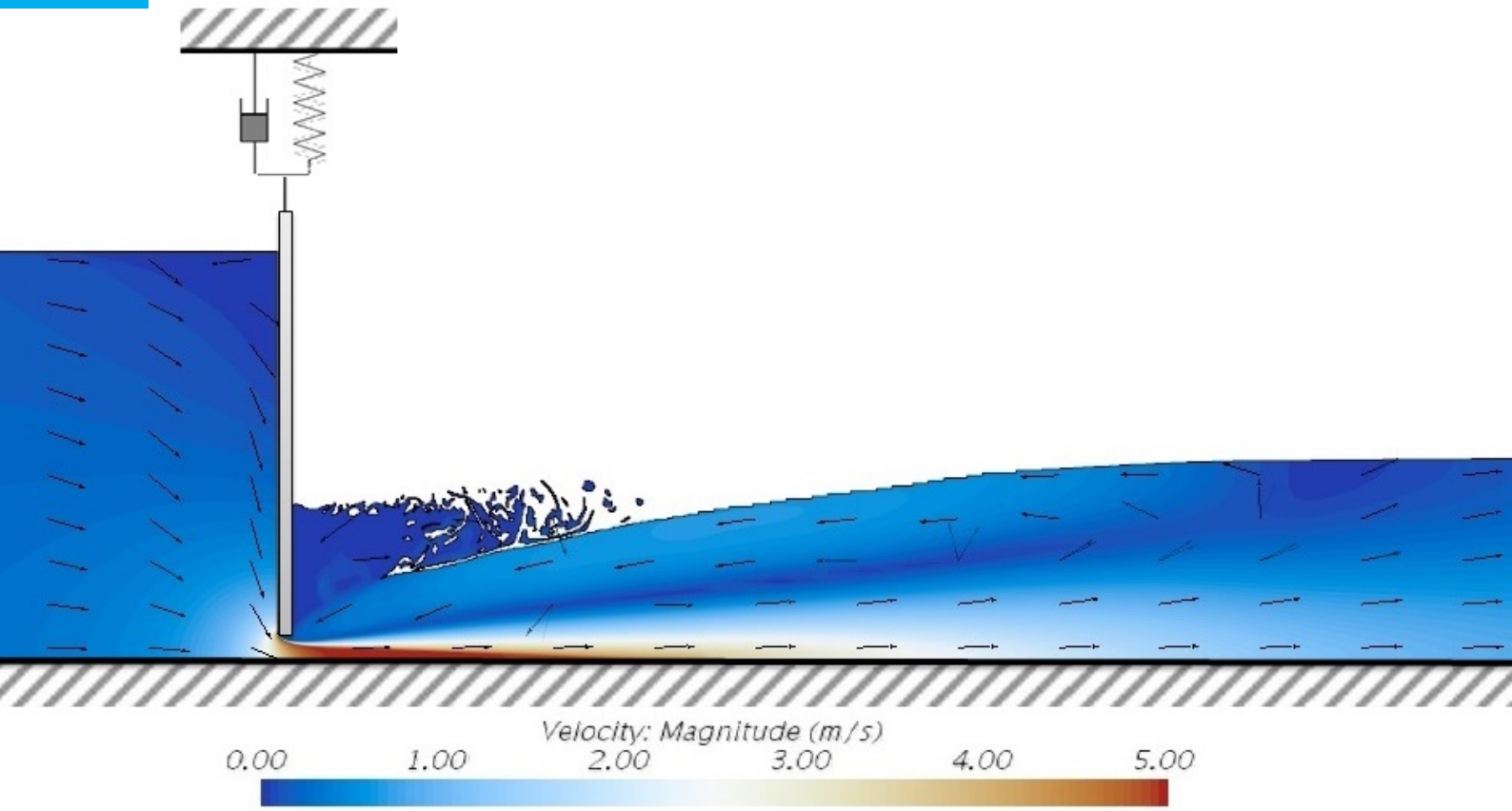


TU Delft Delft University of Technology

Challenge the future

# Flow-Induced Vibrations of Fibre-Reinforced Polymer Hydraulic Gates

by

**J. C. A. Veldhuizen**

in partial fulfilment of the requirements for the degree of

**Master of Science**
in Civil Engineering

at the Delft University of Technology,

**Graduation committee**:

| | | | |
|---|---|---|---|
| Chair: | Prof. dr. ir. S. N. Jonkman, | Hydraulic Structures and Flood Risk, | TU-Delft |
| Daily supervisor: | Ir. W. F. Molenaar, | Hydraulic Structures and Flood Risk, | TU-Delft |
| Daily supervisor: | Ir. O. C. Tieleman, | Hydraulic Structures and Flood Risk, | TU-Delft |
| Technical supervisor | Dr. ir. F. P. van der Meer, | Structural Mechanics, | TU-Delft |
| Company supervisor: | Dr. ir. A. Heinsbroek, | Industrial Hydrodynamics, | Deltares |



TU Delft Delft University of Technology



This thesis is being supported by Deltares as a part of the knowledge program "Natte Kunstwerken van de Toekomst". The support provided by Deltares is gratefully acknowledged.

# ABSTRACT

Hydraulic structures that are surrounded by flowing water can experience undesirable Flow-Induced Vibrations. These vibrations have a record of negative consequences such as the failure of a steel Tainter-gate in the Folsom dam (California USA) that led to the highly undesirable uncontrolled release of fourty percent of Folsom lake.

As traditional steel hydraulic gates (HGs) require a lot of expensive maintenance other materials have been researched to replace steel HGs. One of the possible materials which could replace steel in HGs is Fibre-Reinforced Polymer (FRP). This material is relatively new in Civil Engineering but has proven its potential in aerospace engineering thanks to its high strength and low weight. Although opinions regarding the high durability and low maintenance costs are not yet aligned, the material has the potential to decrease the costs over the whole life cycle. Previously performed research has proven the technical and financial feasibility of the application of FRP in HGs.

Until now FRP has not been applied to HGs on a large scale. Most of the HGs made of FRP do not have a surface larger than four square metres [21]. Therefore, not much is known yet regarding the influence of the use of FRP on the stability and structural reliability of HGs. For instance the largest FRP lock gates in the world, at Sluis III in Tilburg, have been designed and placed without checking the influence of a ship collision on the structural safety of the HGs. This has just recently been researched by Edmondson [1].

The most important cause of vibrations is self-excitation. This is a mechanism in which the forces acting on the HG are amplified by the movement of the HG itself which then further increases the vibration intensity. This mechanism potentially results in structural failure of HGs. Therefore, prevention of this type of excitations should be priority number one in the design stage of HGs (Kolkman and Jongeling [2]). One of the vertical self-excitation mechanisms is the galloping-type vibration and is addressed in this thesis.

The paper regarding the quasi-static analysis of galloping-type vibrations written by Thang and Naudascher [3] is taken as a starting point for this research. Experiments and findings presented by Thang and Naudascher [3] are carefully analysed and agree well with results found by using Computational Fluid Dynamics (CFD) software. In this research their technique to mimic a vertical velocity of the HG in a quasi-static way has been further developed in order to actually simulate the possible occurrence of galloping-type vibrations of a dynamic one degree of freedom system for different HG positions and accompanying vertical velocities of the HG.

As Glass Fibre-Reinforced Polymer (GFRP) is used most often in structural engineering due to its low cost and reasonable performance, this material is used in the case study of this thesis. This case study shows that the use of GFRP in a solid plate results in thicker HGs compared to those made of steel. Therefore, CFD computations have been performed for two HGs with different thicknesses, being five and ten centimetres respectively. CFD computations were used to obtain a force matrix that served as an input for the simulation of vertical vibrations of the one degree of freedom system. This research has shown that the force matrix, obtained using CFD software, can used to derive the hydrodynamic damping coefficients due to flow and hydrodynamic stiffness coefficients due to flow and buoyancy for a range of combinations of opening heights and accompanying vertical velocities of the HG.

Next an analysis is performed to determine the dynamic response of the HG, which is modelled as an one degree of freedom system, to the flow-induced loading for different opening heights and a range of external (structural) damping coefficients. These results were further processed to determine the required external damping coefficient for a number of initial opening heights. The damping coefficient that was required to obtain a fully stable situation for all initial opening heights complied with the results found by determining the negative hydrodynamic damping coefficients due to flow. Therefore, this research has shown that the stability to galloping-type vibrations and the required external damping coefficient can be derived from the force matrix obtained using CFD.

The influence of the larger thickness on the stability against vertical galloping-type vibrations of HGs is significant. First of all a larger thickness results in a higher negative hydrodynamic damping coefficient. This increases the susceptibility to self-excitation and consequently requires more external (structural) damping to neutralise the negative effects of the negative hydrodynamic damping. The found negative hydrodynamic damping for the thick HG is larger than the negative hydrodynamic damping found for the thin HG. The increase is found to be equal to the linear scaling of the increase in thickness of the HG, i.e. a twice as large thickness results in a twice as large negative hydrodynamic damping.

Secondly a larger thickness results in a larger range of opening heights at which this negative hydrodynamic damping occurs, further increasing the susceptibility to galloping-type vibrations. Furthermore, this research has shown that the required external damping coefficient to prevent galloping-type vibrations, does not necessarily has to be larger than the maximum negative hydrodynamic damping coefficient due to flow since the highest negative hydrodynamic damping coefficient may well occur for a small range of opening heights and accompanying vertical velocities.

A second case study which includes a realistic design of both an FRP HG and a steel HG is performed. The FRP HG consists of a laminate structure with different layers and accompanying fibre directions and the steel HG consists of a vertical plate stiffened using three stiffeners as shown in figure 1.

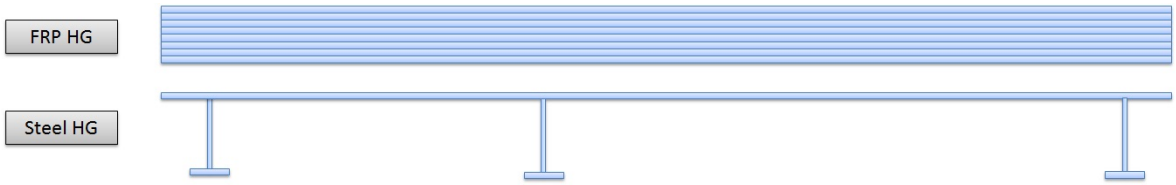


Figure 1: Designs of the GFRP HG and steel HG

The research performed has shown that the FRP laminate experienced roughly twice as high negative hydrodynamic damping values than the typical steel HG. This means that the FRP laminate requires twice as much external damping to neutralise the significantly higher negative hydrodynamic damping due to flow. The steel HG experiences a larger range of negative hydrodynamic damping albeit with much lower negative hydrodynamic damping coefficients than the FRP laminate HG.

Concluding this research, results show that FRP HGs are more susceptible to galloping-type vibrations than traditional steel HGs, meaning that either the design of the HG has to be altered or much more external damping, in this case twice as much, is required to compensate for the negative hydrodynamic damping due to flow, with respect to steel HGs.

# ACKNOWLEDGEMENTS

Before you lays the final product of my graduation research. This thesis is written as a partial fulfilment for the degree of Master of Science in Structural Engineering at the faculty of Civil Engineering at the Delft University of Technology. This research has been performed in cooperation with Deltares. The guidance, assistance and pleasant working environment provided by Deltares are gratefully acknowledged.

Hereby, I would like to seize the opportunity to thank the graduation committee involved in this research. Thank you, Bas, for your enthusiasm and valuable input during meetings. Thank you, Anton, for our weekly meetings and your feedback on the bigger picture as well as detailed parts of this thesis. Thank you, Orson, for our meetings which I have experienced as both pleasant and educative. Thank you, Wilfred, for your support and constructive feedback and thank you, Frans, for your advice and expertise in the field of Fibre-Reinforced Polymers.

I would also like to thank you, Tommaso Boschetti, for your open door policy, enthusiasm and helpfulness in the application of Computational Fluid Dynamics during this research and thank you, Tom O'Mahoney, for your guidance as my supervisor during the first months of this research.

Special thanks go out to my parents and brothers for supporting me in pursuing my ambition to become a civil engineer, twice.

*Jelmer Veldhuizen*
*Delft,* $23^{rd}$ *of October, 2017*

# NOMENCLATURE

Table 1: Abbreviations

| | | |
|---|---|---|
| CFRP | = | Carbon Fibre-Reinforced Polymer |
| EP | = | Epoxy |
| FIV | = | Flow-Induced Vibrations |
| FRP | = | Fibre-Reinforced Polymer |
| FSI | = | Fluid-Structure Interaction |
| GFRP | = | Glass Fibre-Reinforced Polymer |
| HG | = | Hydraulic gate |
| UP | = | Unsaturated Polyester |
| VE | = | Vinyl Ester |

Table 2: Dimensionless numbers used in FSI

| | | |
|---|---|---|
| C | = | The Courant number |
| $C_D$ | = | Drag force coefficient |
| $C_F$ | = | Coefficient accounting for the component of the flow force |
| $C_L$ | = | Lift-coefficient |
| D | = | The displacement number |
| Fr | = | The Froude number |
| Re | = | The Reynolds number |
| S | = | The Strouhal number |
| $T_f$ | = | The fluid timescale |
| $T_s$ | = | The solid timescale |
| $U_r$ | = | The reduced velocity |

Table 3: Units

| | | | |
|---|---|---|---|
| Hertz | [Hz] | = | $[1/s]$ |
| Newton | [N] | = | $[kgm/s^2]$ |
| Pascal | [Pa] | = | $[N/m^2]$ |

Table 4: Alphabetical symbols part 1

| | | | |
|---|---|---|---|
| $A$ | = | Amplitude of vibration | $[m]$ |
| $A_1$ | = | Derivative of the lift-coefficient as a function of the inclination angle | [-] |
| $A_{cross-section}$ | = | Water piercing surface of the hydraulic gate | $[m^2]$ |
| c | = | Damping | [Ns/m] |
| | = | Coefficient of added mass | [kg/m] |
| $C_r$ | = | Radiation coefficient | [N] |
| $c_r$ | = | Pressure wave celerity in water | [m/s] |
| $c_w$ | = | Added hydrodynamic water damping | [Ns/m] |
| $d$ | = | Thickness of the hydraulic gate | $[m]$ |
| D | = | Drag force | [N] |
| E | = | Young's modulus / modulus of elasticity | [Pa] |
| $E_{11}$ | = | Modulus of elasticity parallel to the fibre | [Pa] |
| $E_{22}$ | = | Modulus of elasticity perpendicular to the fibre | [Pa] |
| $E_{tot}$ | = | Total energy in the system | [Nm] |
| $E_{kin}$ | = | Kinetic energy in the system | [Nm] |
| $E_{pot}$ | = | Potential energy in the system | [Nm] |
| $F_{dynamic}$ | = | Dynamic flow force due to inertia | [N] |
| $F(y, \frac{dy}{dt})$ | = | Force as a function of the position and vertical velocity | [N] |
| $f_f$ | = | Frequency of fluid fluctuations | [Hz] |
| $f_n$ | = | Fundamental frequency | [Hz] |
| $f_s$ | = | Frequency of the solid | [Hz] |
| $F_{static}$ | = | Static flow force | [N] |
| F(t) | = | Time-dependent force | [N] |
| $F_y$ | = | Force in y-direction | $[N]$ |
| g | = | Gravitational acceleration | $[m/s^2]$ |
| h | = | Height of a structure | [m] |
| | = | Water depth | [m] |
| $h_i$ | = | Local piezometric head at the gate underside | $[m]$ |
| $h_1$ | = | Upstream water level | $[m]$ |
| $h_2$ | = | Downstream water level | $[m]$ |
| I | = | Moment of inertia | $[m^4]$ |
| J | = | Mass moment of inertia | $[kgm^2]$ |
| k | = | Stiffness | [N/m] |
| $k_h$ | = | Horizontal seismic coefficient | [-] |
| $k_{sudden}$ | = | Sudden stiffness due to flow | [N/m] |
| $k_{w-flow}$ | = | Stiffness due to flow | [N/m] |
| $k_w$ | = | Added hydrodynamic stiffness | [N/m] |
| L | = | Length measure, such as the height of the solid in case of vertical vibrations | [m] |
| | | The thickness of the solid in case of horizontal vibrations0 | [m] |
| | | Lift force | [N] |
| m | = | Mass | [kg] |
| $m_w$ | = | Added hydrodynamic mass | [kg] |
| $m_w(z)$ | = | Added water mass as a function of the water depth | $[kg/m^2]$ |

Table 5: Alphabetical symbols part 2

| | | | |
|---|---|---|---|
| $mm$ | = | Number of columns in the force matrix | [−] |
| $nn$ | = | Number of rows in the force matrix | [−] |
| p | = | Hydrodynamic pressure | [Pa] |
| s | = | Opening height of the HG | [m] |
| t | = | Time | [s] |
| | = | Thickness of a structure | [m] |
| $T_n$ | = | Fundamental period | [s] |
| $t_s$ | = | Thickness of the solid | [m] |
| $T_n$ | = | Fundamental resonance period | [s] |
| $U_0$ | = | Flow velocity | [m/s] |
| $U_{x_i}$ | = | Component of the flow velocity in $x_i$-direction | [m/s] |
| $V$ and $V_1$ | = | Flow velocity in the Vena Contracta | [m/s] |
| $V_f$ | = | Fibre volume fraction | [-] |
| w | = | Width of a structure | [m] |
| x | = | Direction of the coordinate system | [-] |
| y | = | Displacement | [m] |
| | = | Direction of the coordinate system | [-] |
| Y | = | Amplitude of vibration | [m] |
| | | Position of the oscillator | [$m$] |
| $y_0$ | = | Initial opening height | [m] |
| $y_{min}$ | = | Minimal used opening height | [$m$] |
| z | = | Vertical coordinate in the water column | [m] |
| | = | Direction of the coordinate system | [-] |
| $z_j$ | = | Distance to neutral axis for the j$^{th}$ layer | [m] |

Table 6: Greek symbols

| | | | |
|---|---|---|---|
| $\alpha$ | = | Approach angle of the flow | [°] |
| $\gamma$ | = | Fluctuations in gap width due to movement of the gate | [m] |
| $\gamma_{12}$ | = | Shear strain | [-] |
| $\delta$ | = | Opening height of a static HG | [m] |
| $\epsilon_{11}$ | = | Strain parallel to the fibres | [-] |
| $\epsilon_{22}$ | = | Strain perpendicular to the fibres | [-] |
| $\Theta$ | = | Angle of the fibre alignment in relation to the global frame | [°] |
| $\mu$ | = | Dynamic viscosity of the fluid | [$Ns/m^2$] |
| $\nu_{12}$ | = | Poison ratio | [-] |
| $\xi_0$ | = | Vibration amplitude | [m] |
| $\pi$ | = | Pi | [-] |
| $\rho$ | = | Density | [$kg/m^3$] |
| $\rho_f$ | = | Density of the fluid | [$kg/m^3$] |
| $\rho_s$ | = | Density of the solid | [$kg/m^3$] |
| $\sigma$ | = | Stress | [Pa] |
| $\sigma_y$ | = | Yield stress | [Pa] |
| $\sigma_{11}$ | = | Normal stress parallel to the fibres | [$N/mm^2$] |
| $\sigma^*_{11,ult}$ | = | Ultimate tensile stress parallel to the fibre at failure | [Pa] |
| $\sigma_{22}$ | = | Normal stress perpendicular to the fibres | [$N/mm^2$] |
| $\sigma^*_{22,ult}$ | = | Ultimate tensile stress perpendicular to the fibre at failure | [Pa] |
| $\tau_{12}$ | = | Shear stress | [$N/mm^2$] |
| $\phi$ | = | Phase shift | [$rad$] |
| $\psi$ | = | Dimensionless measure of the vibration frequency | [-] |
| $\omega_n$ | = | Natural angular frequency | [rad/s] |

Table 7: Combined alphabetical and Greek symbols

| | | | |
|---|---|---|---|
| $\Delta D$ | = | Dissipated energy | [J] |
| $\Delta H$ | = | Hydraulic head | [m] |
| $\Delta t$ | = | Time step size | [s] |
| $\Delta_{x_i}$ | = | Mesh size in $x_i$-direction | [m] |
| $\Delta y$ | = | Difference between the maximal and minimal used opening height | $[m]$ |
| $\frac{dy}{dt}_0$ | = | Initial vertical velocity | $[m/s]$ |
| $\frac{dy}{dt}_{min}$ | = | Minimal used vertical velocity | $[m/s]$ |
| $\Delta\frac{dy}{dt}$ | = | Difference between the maximal and minimal used velocities | $[m/s]$ |

# CONTENTS

# 1

# INTRODUCTION

This research presents a method to predict the susceptibility to galloping-type vibrations of hydraulic gates (HGs) with a vertical degree of freedom in the design stage.

This chapter is used to discuss the background of this research and accompanying problem definition. Based on the problem definition a research question and sub-questions are stated

## 1.1. BACKGROUND

HGs may experience undesirable Flow-Induced Vibrations (FIV). An example can be found in the failure of one of the steel Tainter-gates of the Folsom dam located in California (USA), which led to the release of about forty percent of the water that was stored in Folsom Lake. According to the analysis performed by Anami *et al.* [8], small vibration amplitudes resulted in extreme hydrodynamic pressure fluctuations of around 1.6 times the static load, which led to the failure of one of the Tainter-gates. Figure 1.1 and figure 1.2 show pictures of the gate during and after the release of water. Also, according to Erdbrink [7] hydraulic structures are susceptible to FIV that is not yet properly addressed in guidelines but may result in failure of the structure and therefore possibly lead to flooding.

Figure 1.1: Folsom dam after the Tainter-gate failed [9]

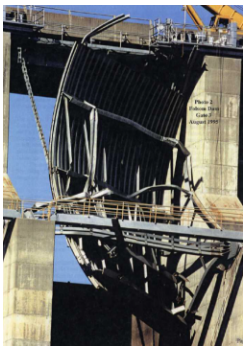

Figure 1.2: Close-up of the Tainter-gate after failure [9]

The guideline "Dynamic behaviour of hydraulic structures" [2] is written based on years of measurements of primarily steel hydraulic structures and offers a means to predict possible undesirable vibrations during the design stage. Fibre-Reinforced Polymer (FRP) promises to become an important construction material in the field of hydraulic structures due to its high strength, high durability and low maintenance costs. It has also been considered to be used for replacing the HGs of the Eastern Scheldt storm surge barrier due to unexpected required continuous maintenance of the existing steel HGs, which is extremely expensive. Research has shown that replacing the current HGs with HGs made of FRP is both technically and financially feasible (Straten [10] and Veraart [11]).

According to Ross [12], FRP hydraulic structures generally have a lower natural frequency. Since excitation frequencies in case of HGs typically are lower than the mechanical natural frequency it is to be expected that HGs made of FRP may be more susceptible to FIV.

## 1.2. PROBLEM DEFINITION

In August 2017 Edmondson [1] presented his research on the response of FRP lock gates on ship collision. His case study involved the FRP lock gates of Sluis III in Tilburg (NL), which recently have been installed and currently are the largest FRP lock gates in the world. Up until his research the response of the FRP lock gates to ship collision was unknown. Fortunately his research has shown that the FRP lock gates can withstand a ship collision, but the outcome could have been different as well. The fact that the largest FRP lock gates in the world have been designed and built without checking the possible failure due to ship collision is a clear example that the application of FRP in large scale HGs is still requiring a lot of research.

Currently it is not possible to predict the dynamic behaviour of HGs made of FRP. Designers are thus unable to consider undesirable vibrations of the structure which in turn may result in required adjustments of the construction itself or adjustments in the use of the structure. An example of the latter is a change in levelling procedure in a shipping lock. FIV of the steel visor gates at the weir complex in Driel (see figure 1.3 have resulted in required changes in the opening and closing operation, being a minimum opening height of 25 centimetres, i.e. the gates need to be opened and can be kept at a constant opening height of minimal 25 centimetres. A smaller third gate is used for discharges smaller than the discharge occurring for an opening height of 25 centimetres, being 100 $m^3/s$. The necessity of this third gate has not been forseen and required adjustments to the structure.

Figure 1.3: Weir complex in Driel [13]

A literature review on failure of HGs made of FRP has not shown reports of HGs which failed due to FIV yet, although the increasing use of FRPs in HGs combined with the lack of experience and knowledge regarding the dynamic stability and safety of FRP HGs may, without further research, result failure of HGs and consequently potential catastrophes such as floods. The dynamic stability and safety is especially crucial for hydraulic structures which only have one line of defence. A shipping lock for instance has at least two HGs, while a discharge sluice only consists of one HG.

Therefore, failure of a hydraulic structure with one line of defence will have a much larger impact as witnessed with the broken weir in Grave (figure 1.4) in December 2016, where a ship sailed into the weir resulting in large water level drops and obstruction of river transport. Repairs of the weir were completed after half a year, i.e. negative consequences have been experienced for the same period.

The most important cause of vibrations is the self-excitation [2]. According to Vijay *et al.* [14]: "Structures such as hydraulic gates have a tendency to exhibit self-excited vibrations during overflow and underflow scenarios." Also Ishii and Naudascher [15] researched self-excitation of HGs and reported on a vicious circle of Tainter-gate vibrations in which a fluctuating discharge due to opening or closing of the gate resulted in fluctuating pressures, leading to gate vibrations and therefore again a fluctuating discharge.

Figure 1.4: The broken weir at Grave

Figure 1.5: Consequences of the water level drops

Often the exact excitation mechanism responsible for flow-induced vibrations HGs is not known. Also sometimes scientists do not agree on the governing mechanism responsible for vibrations. For instance Kolkman and Jongeling [2] attributes vibrations for HGs with a vertical degree of freedom to the so-called bath-plug mechanism, which is one of the self-excitation mechanisms. Thang and Naudascher [3] states that the cause of vibrations can be traced back to negative hydrodynamic damping for galloping-type vibrations, which also is one of the self-excitation mechanisms. Since vertical vibrations and especially self-excited mechanisms may result in failure of HGs this thesis will focus on galloping-type vibrations in which Thang and Naudascher [3] will serve as a valuable starting point for this research.

## 1.3. RESEARCH QUESTION

Based on state of the art research it is concluded that the influence of FRP on the dynamic assessment of HGs, and more specifically galloping-type vibrations, has not yet been properly addressed. Therefore, the research question is formulated as:

**Research question:** What influence does the choice for Fibre-Reinforced Polymer have on the occurrence of flow-induced galloping-type vibrations of hydraulic gates with underflow?

The answer to this research question is primarily based on conclusions the following sub-questions:

**Regarding the influences of FRP on dynamic properties of HGs:**

1. What does the choice of Fibre-Reinforced Polymer mean for the dynamic properties of a hydraulic gate?

**Regarding the dynamic behaviour of hydraulic gates with a vertical degree of freedom:**

2. How can the dynamic behaviour of a hydraulic gate with underflow be predicted?

3. What is the influence of the vertically moving structure on the flow-induced loading?

   **Regarding the influence of water on dynamical properties:**

4. Which added terms can be computed using transient CFD computations?

## 1.4. RESEARCH METHOD

First of all a literature study is performed in which fluid-structure-interaction (chapter 3) is reviewed regarding the causes for and influences of flow-induced vibrations, the influence of (flowing) water on dynamic properties of a structure and related performed research on flow-induced vibrations. Applications and properties of FRP are elaborated (chapter 2) including performed research (theses) regarding the use of FRP in hydraulic gates.

The influence of this material on hydraulic gates is studied in terms of dynamic properties including the influence of the surrounding water (chapter 4). Based on conclusions from combining knowledge obtained from the steps as described above, important possible differences between hydraulic gates made of steel and FRP are described.

The paper regarding self-excited vibrations of vertical lift gates written by Thang and Naudascher [3] is used as a starting point for the analysis using Computational Fluid Dynamics (CFD) software (chapter 5). Also results from the paper are used to validate the outcome of the CFD computations.

Hydrodynamic forces obtained using CFD computations are then used as input for the equation of motion of a mass-spring-damper system which is solved using a MATLAB script (chapter 6). This will result in the response of the system to the hydrodynamic forces. Parameters in which an FRP hydraulic gate can differ from a steel hydraulic gate are varied and differences between the two are discussed. Also influences of variations of the dynamic properties of a mass-spring-damper system on the stability of the dynamic system is addressed. Finally a basic design of a traditional steel structure is made and the response to flow-induced dynamic loading is compared to a HG made of FRP having the same bending stiffness.

## 1.5. REPORT STRUCTURE

The flowchart for the research performed in this thesis is shown in figure 1.6

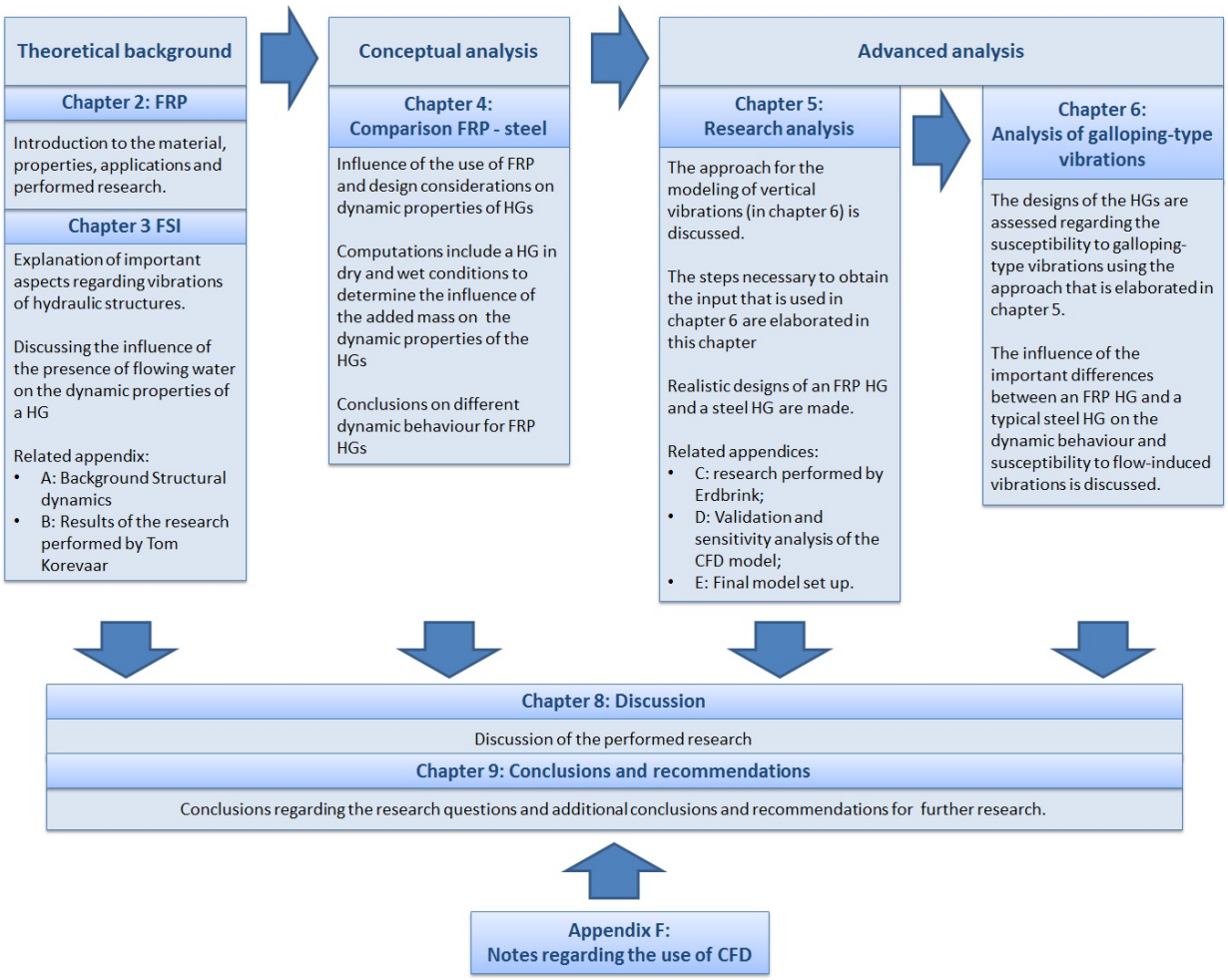


Figure 1.6: Flowchart for this report

# 2

# FIBRE-REINFORCED POLYMERS

Fibre-Reinforced Polymer (FRP) promises to become an important construction material. Since this material is relatively new in application in the field of civil engineering this section is dedicated to introducing the material and determining the possible influence the choice of this material has on dynamic properties of hydraulic gates. The main sources for this section are the lecture notes and presentations on FRP made by Kolstein [18].

In section 2.1 general information regarding FRP is provided. Applications of FRPs in civil engineering are shown in section 2.2. Used materials in FRPs are shown in section 2.3. Mechanical and dynamic properties of FRPs are elaborated in section 2.4 in which the most important aspects regarding the dynamic behaviour of a structure. An extensive literature study is performed by Gómez [19]. Therefore, materials and properties of FRP are only described briefly in this chapter. Performed research on the application and dynamic properties of FRPs are mentioned in section 2.5. Conclusions regarding FRPs are drawn in section 2.6.

## 2.1. GENERAL INFORMATION

Fibre-Reinforced Polymers are being used for a vast number of structural applications such as wings of an air plane, the body of a Formula 1 car and the blades of wind turbines. FRP structures are increasingly being applied in civil engineering due to a decrease in costs and its use offers opportunities when innovative solutions are required [18]. The use of FRP comes with great advantages as well as disadvantages. It offers a high strength/weight ratio which leads to slender and low weight structures resulting in a smaller required foundation, lighter machinery and other advantages, this concatenation of effects is called the" snowball effect". The possible prefabrication of structures or elements allow for a controlled environment with the right working conditions and quicker on-site build which reduces the inconvenience caused by the construction works. The controlled working environment also contributes to the high quality of the finished FRP structure. FRP is also known for its high durability and low required maintenance which is a big advantage in for example the case of a highly corrosive environment. Another advantage is the high design freedom and formability which is desirable in case of non-standard shaped structures. The design freedom may also allow for the optimisation of a design in which possible drawbacks of the design can be eliminated.

As with all other building materials, FRPs have some drawbacks. One of the disadvantages of FRPs is that the high strength / weight ratio results in slender structures which is not a bad thing in itself but slender members give relatively large deflections due to their high strength and moderate stiffness. Also FRP structures are not as ductile as steel, i.e. failure occurs for smaller strains than for steel, resulting in a smaller deformation capacity. This results in special care during the design of such structures and high safety factors, which makes the structure more expensive. Together with relatively high material costs this often results in higher initial costs of the realised structure when compared to a steel variant. In cases of possible fire outbreaks FRP might not be the best construction material due to its low fire resistance. For this thesis the fire safety of FRP is not of interest. FRPs might also require a surface protection due to its vulnerability to humidity, alkaline attack and UV radiation.

## 2.2. FRP IN CIVIL ENGINEERING APPLICATIONS

FRP has been used for the construction of both pedestrian and road bridges. The use of FRP in bridges has resulted in tremendous reduction of their weight. In case of the Friedberg Bridge [20] in Germany the use of FRP has resulted in a reduction of 83% of the weight of the bridge deck compared to a pre-stressed concrete variant (14 kN/m against 84 kN/m) and a reduction of 73% compared to a steel-concrete composite deck (14 kN/m against 62 kN/m). In Nørre Aaby (Denmark) a pedestrian bridge entirely made out of FRP is placed weighing only 60 kN, which is incredibly light compared to a reinforced concrete alternative having an approximated weight of 1200 kN. This is a major reduction of 95 % of the weight.

FRP is also used for the load bearing structures inside buildings, for the strengthening of already existing structures and important for this thesis; FRP is also used for shipping lock doors. Recently the largest FRP lock doors in the world have been installed in the Netherlands in the shipping lock complex named "Sluis III". FRPs have been used in Japan for small scale hydraulic gates since the 1960's [21]. They have also been used in wicket gates [14]. FRPs are often used in piles, sheet piles and piers or other corrosive (e.g. marine) environments [22]

Currently there are no guidelines for the application of FRP in hydraulic structures. Tomiyama and Nishizaki [21] states that in the future, it will be a necessity to have guidelines available for the application of FRP in hydraulic gates so that the visibility and use of FRP in this field of work can take flight.

## 2.3. MATERIALS

In general FRP consists of a matrix material and a reinforcement. Fibres, being the reinforcement, provide strength and stiffness while the main purpose of the matrix material, being the resin or polymer, is to provide stability for the reinforcing fibres. The mechanical properties of the matrix material are considerably lower than those of the reinforcement. There are a lot of different types of fibres of which glass fibre is most commonly used. Aramid fibres and carbon fibres have a better performance than glass fibres but also come at a higher price of 15 to 40 times higher than glass fibres [18]. Aramid fibres and carbon fibres are increasingly being used while natural fibres have a limited use due to its low performance. Properties of the reinforcing fibres are show in figure 2.1.

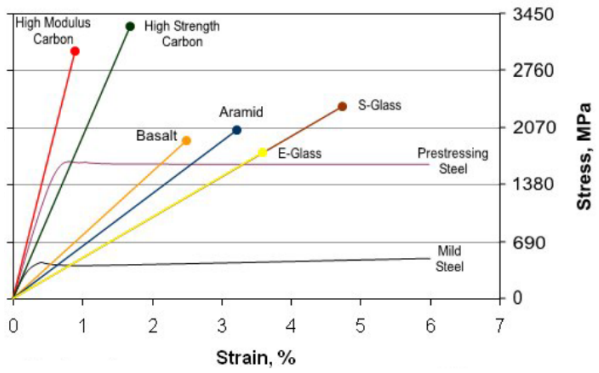


Figure 2.1: Mechanical properties of reinforcing fibres [18]

Resins and polymers are divided in two different types. The most commonly used resins are resins of the thermosetting type, which means that after the curing of the resin it cannot be reformed or softened using heat. Some thermosetting resins are: Unsaturated Polyester (UP), Vinyl Ester (VE) and Epoxy (EP). Of which Unsaturated Polyester is the most commonly used resin in FRP structures and EP is the most advanced but also most expensive resin. Thermoplastic type resins have the property of softening when reheated which can be useful when reshaping of the material is desired but is resulting in poor fire safety performance. Properties of resins and polyesters are shown in figure 2.2.

In case of a sandwich panel also a core is present. Sandwich panels improve the efficiency of the FRP structure in which the core is primarily used to increase the bending stiffness. Another advantage of a core material can be the increased thermal insulation.

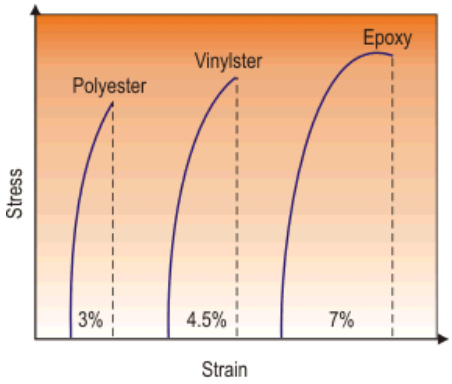


Figure 2.2: Mechanical properties of resins or polyesters [18]

## 2.4. PROPERTIES OF FRP

The mechanical properties of Fibre-Reinforced Polymers are mainly depending on the collaboration of the fibres and the resin / polymer. The tensile strength of the composite material is not only depending on the material properties of both the fibres and the resin / polymer, fibre orientation and the fibre content but adhesion between the resin and the fibres, mechanical compatibility between the fibres and the resin also play an important role. As mentioned before; for a more elaborated literature study on the mechanical properties of FRP it is advisable to consult Gómez [19].

### 2.4.1. DYNAMIC PROPERTIES

As mentioned in appendix A dynamic systems can often be schematised as a multi degree of freedom system. In this system the mass, stiffness and damping are the three key factors. The mass of an FRP structure is based on the material use and therefore easily definable.

The stiffness of an FRP structure is primarily depending on the geometry of the structure, properties of the used fibres and the direction of the fibres. The Young's modulus of the FRP structure, in case of a unidirectional material, can be determined using the rule of mixtures: $E_L = E_f * V_f + E_f * (1 - V_f)$. In which subscript L denotes the direction of the fibres, subscript f denotes the fibres, $V_f$ denotes the fibre volume fraction and subscript m the matrix material. The rule of mixture is valid for axial loading and flexural loading in case of negligible shear effects [23].

Damping of an FRP structure is not that easily definable since according to the article " Damping properties " in Donaldson and Miracle [23], on pages 632 until 663, it is depending on a large number of factors, being:

- Proportions and material properties of the reinforcing fibres and matrix material;
- Orientation of the fibres;
- Surface treatment of the reinforcing fibres;
- Damping contributions of cracks and debonds;
- Temperature;
- Frequency and amplitude of the loading.

### 2.4.2. INTERNAL FORCES RELATED TO STRAINS

This section is dedicated to relations between internal forces and strains and is mainly based on van der Meer and Pavlovic [20]. In the local coordinate system the relation between the strains and stresses can be written in matrix form as:

$$\begin{bmatrix} \epsilon_{11} \\ \epsilon_{22} \\ \gamma_{12} \end{bmatrix} = \begin{bmatrix} \frac{1}{E_{11}} & -\frac{\nu_{21}}{E_{11}} & 0 \\ -\frac{\nu_{21}}{E_{11}} & \frac{1}{E_{22}} & 0 \\ 0 & 0 & \frac{1}{G_{12}} \end{bmatrix} \begin{bmatrix} \sigma_{11} \\ \sigma_{22} \\ \tau_{12} \end{bmatrix} \tag{2.1}$$

| | | | | |
|---|---|---|---|---|
| In which: | $\epsilon_{11}$ | = | Strain parallel to the fibres | [-] |
| | $\epsilon_{22}$ | = | Strain perpendicular to the fibres | [-] |
| | $\gamma_{12}$ | = | Shear strain | [-] |
| | $E_{11}$ | = | Young's modulus parallel to the fibres | $[N/mm^2]$ |
| | $E_{22}$ | = | Young's modulus perpendicular to the fibres | $[N/mm^2]$ |
| | $\nu_{12}$ | = | Poison ratio | [-] |
| | $\sigma_{11}$ | = | Normal stress parallel to the fibres | $[N/mm^2]$ |
| | $\sigma_{22}$ | = | Normal stress perpendicular to the fibres | $[N/mm^2]$ |
| | $\tau_{12}$ | = | Shear stress | $[N/mm^2]$ |

The matrix presented in equation 2.1 can be rewritten into:

$$\begin{bmatrix}\sigma_{11}\\ \sigma_{22}\\ \tau_{12}\end{bmatrix} = \begin{bmatrix}\frac{1}{E_{11}} & -\frac{\nu_{21}}{E_{11}} & 0\\ -\frac{\nu_{21}}{E_{11}} & \frac{1}{E_{22}} & 0\\ 0 & 0 & \frac{1}{G_{12}}\end{bmatrix}^{-1} \begin{bmatrix}\epsilon_{11}\\ \epsilon_{22}\\ \gamma_{12}\end{bmatrix} \tag{2.2}$$

Which also can be written as:

$$\bar{\sigma} = \bar{\mathbf{Q}}\epsilon \tag{2.3}$$

In which the overbar indicating the local frame. The local frame can be rewritten into the global frame by means of a transformation matrix, being T.

$$\sigma = T\bar{\mathbf{Q}}T^T\epsilon \tag{2.4}$$

In which Q can be written as:

$$\mathbf{Q} = T\bar{\mathbf{Q}}T^T \tag{2.5}$$

with

$$T = \begin{bmatrix} cos^2 & sin^2 & -2sin\theta cos\theta \\ sin^2 & cos^2 & 2sin\theta cos\theta \\ sin\theta cos\theta & -sin\theta cos\theta & cos^2\theta - sin^2\theta \end{bmatrix} \tag{2.6}$$

In which $\theta$ represents the angle of the fibre alignment in relation to the global frame.

Internal forces, being the axial forces ($N_{xx}$ and $N_{yy}$), shear force ($V_{xy}$), bending moments ($M_{xx}$ and $M_{yy}$) and torsion ($M_{xy}$) are related to internal strains ($\epsilon_{xx}$, $\epsilon_{yy}$ and $\gamma_{xy}$) and curvatures ($\kappa_{xx}$, $\kappa_{yy}$ and $\kappa_{xy}$). Matrices of these relations are found in equation 2.7.

$$\begin{bmatrix}N_{xx}\\ N_{yy}\\ V_{xy}\\ M_{xx}\\ M_{yy}\\ M_{xy}\end{bmatrix} = \begin{bmatrix}\mathbf{A} & \mathbf{B}\\ \mathbf{B} & \mathbf{D}\end{bmatrix} \begin{bmatrix}\epsilon_{xx}\\ \epsilon_{yy}\\ \gamma_{xy}\\ \kappa_{xx}\\ \kappa_{yy}\\ \kappa_{xy}\end{bmatrix} \tag{2.7}$$

Matrix **A**, **B** and **D** are all three by three matrices. In which the **B**-matrix, being the bending/membrane coupling, is zero. For a layered laminate the A-matrix, being the axial stiffness matrix, is computed as follows:

$$\mathbf{A} = \sum_{j=1}^{n} (z_j - z_{j-1})\mathbf{Q}_j \tag{2.8}$$

The **D**-matrix, being the bending stiffness matrix, is computed as:

$$\mathbf{D} = \sum_{j=1}^{n} \frac{1}{3}(z_j^3 - z_{j-1}^3)\mathbf{Q}_j \tag{2.9}$$

| | | | | |
|---|---|---|---|---|
| In which: | j | = | Concerning laminate layer | [-] |
| | n | = | Number of layers in the laminate | [-] |
| | $z_j$ | = | Distance to neutral axis for the $j^{th}$ layer | [m] |
| | $\mathbf{Q}_j$ | = | **Q**-matrix for the $j^{th}$ layer | [-] |

## 2.5. RELATED RESEARCH

Hydraulic gates made out of FRP have been the topic of earlier research already. Straten [10] has looked at the feasibility of FRP slides in the Eastern Scheldt storm surge barrier. He concludes that a FRP variant of the sliding doors can become financially interesting due to a pay back time of 50 years. He recommends that a dynamic assessment of the final design of the structure (see figure 2.3) is performed to analyse the fatigue behaviour and possibly improve the design.

Zorgdrager [24] has studied the feasibility of FRP lock gates in large locks. His case study concerned the Beatrixsluis located in Nieuwegein. His design (see figure 2.4)is estimated to have lower life cycle costs after a period of 30 years, compared to a steel variant. According to Zorgdrager [24] the major drawbacks of FRP at this moment are: absence of ductility, low material stiffness, lack of (public) knowledge of long term performance and detailing. He states that these problems occurring with FRP should be solved before FRP can be applied in projects with larger consequences in case of failure of the lock gates. Recommendations are made concerning the study on vibrations of FRP valves in lock gates due to high flow velocities and low self-weight.

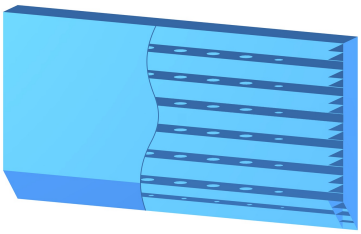

Figure 2.3: Final design Straten [10]

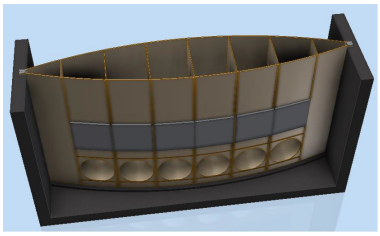

Figure 2.4: Final design Zorgdrager [24]

Kok [25] has looked at the feasibility of the use of FRP in large hydraulic structures. His case study concerned the design of an FRP lifting gate located at the Hartel Canal Barrier at Spijkernisse. He did a variant study and came up with the design as shown in figure 2.5. This final design turned out to be cheaper than a steel variant, both in the build as well as maintenance. He states that the span of an FRP hydraulic gate is only limited by practical possibilities of the manufacturer rather than on material properties of FRP. In his reasearch Kok [25] did not look at the dynamic behaviour of the gate. He also recommends that more design codes should become available for the relatively new material FRP.

Gómez [26] researched the dynamic behaviour of large hydraulic structures in FRP His case study involved a new lift gate (see figure 2.6)for the guard and ship lock in the Julianakanaal. In his analysis he performed a dynamic analysis using both the 1DOF as well as the continuous beam model. He states that since FRP is a new material its dynamic behaviour is not fully known. He recommends that a 2D model for vertical vibrations only should be considered. Also the influence of the hoisting mechanism on the eigen frequency is not taken into account and recommended to be implemented in further research.

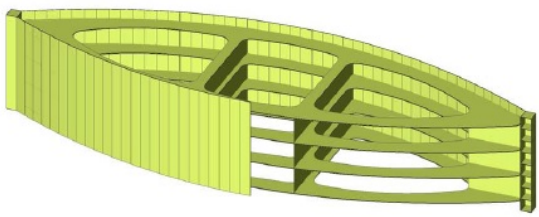

Figure 2.5: Final design Kok [25]

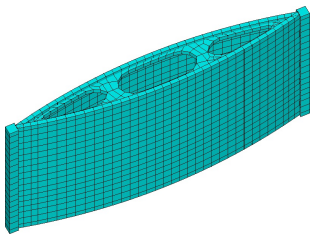

Figure 2.6: Final design Gómez [26]

Ross [12] investigated the flow-induced dynamic behaviour of FRP hydraulic gates using the guideline written by Kolkman and Jongeling [2]. The starting point of his research was the rising segment gate design made by Tuin [27] (see figure 2.7). He states that FRP results in different geometry and dynamic properties of the gate compared to steel. Another important statement that Ross [12] makes is that knowledge of dynamic behaviour is lacking for FRP hydraulic gates. FRP hydraulic gates generally have a lower natural frequency than a steel hydraulic gate resulting in less stable behaviour since the excitation frequencies generally are relatively low. He found solutions for problems concerning the dynamic stability of the design although he acknowledges that maybe not all problems are found or solved. He recommends to perform model testing.

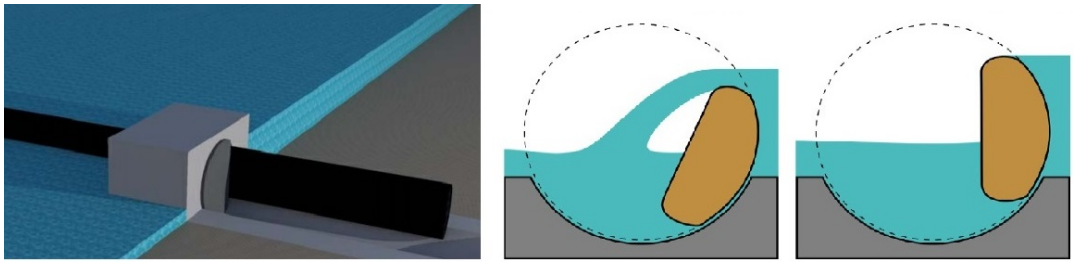

Figure 2.7: Design used by Ross [12]

Edmondson [1] researched the influence of a ship collision on the structural safety of the HGs at Sluis III in Tilburg. These HGs have been designed and built before this assessment is performed. Edmondson [1] has performed his analysis modelling the ship collision in Finite Element Method (FEM) software. Edmondson [1] concludes that the HGs are able to withstand the ship collision.

## 2.6. CONCLUSIONS

The main conclusions that can be drawn from this chapter are the following:

- FRPs have been used in Japan for small scale hydraulic gates ever since the 1960's
- FRPs possess a higher tensile strength than steel;
- FRPs have relatively large deflections due to their high strength and moderate stiffness;
- FRPs show brittle failure and have a lower deformation capacity than steel;
- FRPs have excellent material damping properties and fatigue resistance;
- Material properties strongly depend on the location and direction of the reinforcing fibres;
- Despite the higher building costs for an FRP structure the high durability of FRPs may result in lower maintenance costs and therefore a cheaper solution, especially for structures located in corrosive environments;
- The application of FRP in civil engineering results in much lighter structures than their counterparts made out of other materials, which results in a snowball effect regarding the other structural components which on their turn can be much lighter / smaller as well. Resulting in a more competitive price when compared to other building materials;
- Only limited research has been performed on the dynamic behaviour of FRP HGs. Therefore, this research can be used to fill knowledge gaps in the field of flow-induced vibrations of FRP HGs;
- The previously performed research regarding flow-induced vibrations, as discussed 2.5, mostly concerned the check on stability by comparing the natural frequencies of the HG with the excitation frequency. Also this means that there are knowledge gaps. The knowledge obtained in this research can contribute to a better understanding of flow-induced vibrations of FRP HGs;
- In order for the use of FRPs as a building material to take flight more guidelines should be available for the assessment of FRPs used in hydraulic gates;
- The performed research as described in this section concern large HGs. For HGs with a smaller width the chosen geometries in this section it is expected that a sandwich structure or a plate stiffened with ribs is applied.

# 3

# FLUID-STRUCTURE INTERACTION

In order to understand the dynamic behaviour of hydraulic gates this chapter is dedicated to the basic principles of Fluid-Structure interaction, abbreviated as FSI. Excitation sources for vibrations of hydraulic gates are elaborated in section 3.1. Dimensionless numbers used in FSI are mentioned in section 3.2. The influence of the surrounding water on the dynamic properties of hydraulic gates is explained in section 3.4. Research related to the research performed in this thesis is addressed in section 3.5. Conclusions regarding FSI for hydraulic gates are drawn in section 3.6.

## 3.1. SOURCES OF EXCITATION

This section is used for the elaboration of some basic aspects concerning FSI. The main source for this section is written by Kolkman and Jongeling [2]. Fluid-Structure Interaction is a part of the field of fluid dynamics and focuses on the interaction between a moving or deforming structure and the flow trough or around it. This means that the flowing water not only has an influence on the structure but the structure also influences the flow, resulting in a coupling between the two.

As described in the guideline written by Kolkman and Jongeling [2], the excitation sources can be classified in five different types, being the following:

- Type 1: Excitation by initial turbulence and by turbulence in the wake;
- Type 2: Excitation due to flow instability;
- Type 3: Self-excitation;
- Type 4: Amplification of the excitation due to the resonant rise of the water;
- Type 5: Unstable fluid resonance with self-excitation.

**Type 1: Excitation by initial turbulence and by turbulence in the wake.** Pressure fluctuations due to turbulence in the approaching flow might lead to a dynamic load on the structure which may have a dominant frequency close to one of the natural frequencies of the structure. Turbulence and therefore a dynamic and possibly periodic load also occurs in the wake downstream of the structure, i.e. vortex trail, due to the presence of the structure itself. For hydraulic gates this excitation source is negligible since its excitation frequencies usually are much lower than the natural frequencies of hydraulic gates [2]. An example of how to determine the frequency of vortex excitation is shown below. Figure 3.1 shows the figure that can be used to determine turbulence excitation frequencies.

The dimensionless Strouhal number is used to describe fluctuating flow mechanisms and is computed as follows:

$$S = \frac{fh}{V_1} \tag{3.1}$$

| | | | | |
|---|---|---|---|---|
| In which: | f | = | Frequency of oscillation | [Hz] or [1/s] |
| | h | = | Height of the culvert | [m] |
| | $V_1$ | = | Flow velocity in the vena contracta | [m/s] |

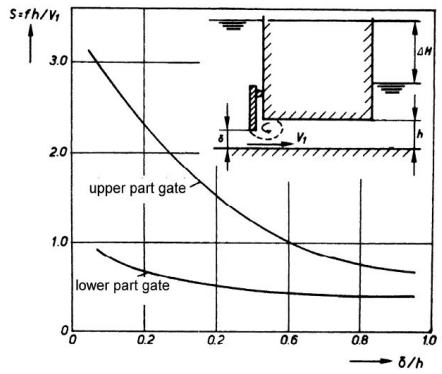


Figure 3.1: Strouhal numbers for horizontal excitation of hydraulic gates in culverts [2]

A simple example follows:

| | | | | | |
|---|---|---|---|---|---|
| $\Delta$ H | = | Hydraulic head | = | 1 | [m] |
| h | = | Height of the culvert | = | 1 | [m] |
| $\delta$ | = | Gap height | = | 0.4 | [m] |
| S | = | Strouhal number for horizontal vortex shedding of culvert gates | = | 0.5 | [-] |

with:

$$V_1 = \sqrt{2g\Delta H} = \sqrt{2 * 9.81 * 1} = 4.43\ [m/s] \tag{3.2}$$

Resulting in:

$$f = \frac{SV_1}{h} = \frac{0.5 * 4.43}{1} = 2.21\ [Hz] \tag{3.3}$$

Figure 3.2 is used to determine the Strouhal number for vertical excitation frequencies and is used in a similar way as figure 3.1.

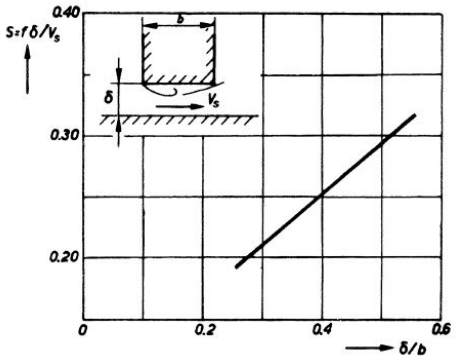


Figure 3.2: Strouhal numbers for vertical excitation of the bottom edge of a hydraulic gate [2]

It is recommended to have a resonance frequency that is a factor two to three times higher than the dominant excitation frequency of turbulence in the flow in order to avoid vibrations.

**Type 2: Excitation due to flow instability.** The flow is influenced significantly by the points of separation and reattachment. Since the points of separation and reattachment of the flow for round shaped structures are undetermined the flow instability is accompanied by pressure differences and therefore a dynamic load on the structure. The points of separation and reattachment of the flow may also shift periodically due to the vibration of the structure itself.

In the case of hydraulic gates with reattaching flow the area between the shifting points of separation and reattachment may be subjected to a relative under pressure resulting in large dynamic loads on the structure. There are a lot of situations in which flow instability occurs.

**Type 3: Self-excitation.** Self-excitation, i.e. movement-induced excitation, occurs in cases when the dynamic load and the vibration of the structure both are a harmonic function in time with the dynamic load being in-phase with the velocity of the vibrating structure and the load amplitude being coupled to the vibration amplitude. The interaction between the vibration and dynamic loading results in the exponential growth of the vibration amplitude up to the point where the vibration amplitude is limited by for instance a wall. Self-excitation or movement-induced excitation is also referred to as negative damping, self-excitation vibration or feedback vibration. Self-excitation does not occur for non-vibrating structures, i.e. self-excitation only occurs when a gate is starting to vibrate (even with small amplitudes) due to turbulence and vortex shedding.

A lot of mechanisms may induce self-excitation vibration. Due to the possible occurrence of large vibration amplitudes, self-excitation should be prevented and, therefore, in the design of a hydraulic structure this type of excitation is priority number one.

According to Kolkman [16] there are a few important aspects related to self-excitation:

- The shape of the gate or valve;
- The stiffness of the structure;
- Damping in the structure or external dampers;

There are three main types of self-excitation of which the first two types have by far not been studied as much as for instance vortex shedding and galloping [7]. Types of self-excitation:

**Self-excitation due to varying gap height.** This type is related to vertical vibrations of the gate for small values of the gap height. For movement of the gate in upward direction the gap height and subsequently the discharge increase, results in a decrease of the local hydraulic head and therefore a decrease of the suction force which increases the upward movement of the gate. Figure 3.3 is used to determine susceptibility to self-excitation due to varying discharge coefficient.

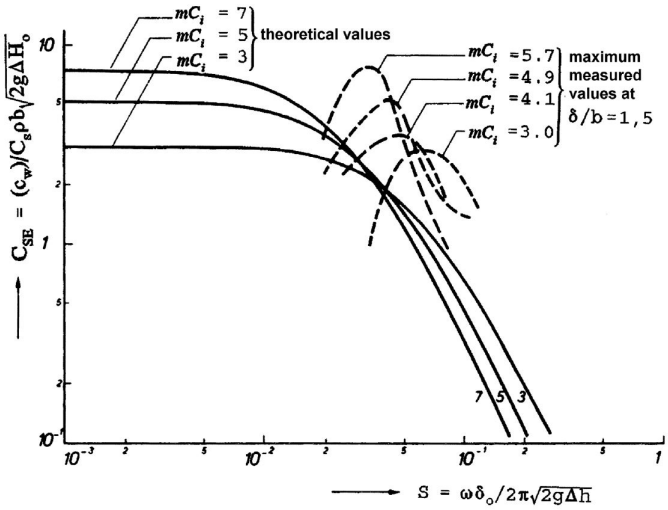


Figure 3.3: Extend of vertical self-excitation [2]

Vertical self-excitation occurs at rather low Strouhal numbers which are depending on the gap width. The figure can be used to determine the most sensitive (structural) resonance frequencies. An example follows:

$$S = \frac{f\delta}{\sqrt{2g\Delta H}} \tag{3.4}$$

| | | | | | | |
|---|---|---|---|---|---|---|
| In which: | f | = | $\omega/(2\pi)$ | = | Resonance frequency | [Hz] |
| | $\delta$ | = | Gap width | [m] | | |
| | $\Delta H$ | = | Hydraulic head over the gate | [m] | | |

For a Strouhal number of 0.05, a hydraulic head of 10 metres and a opening height of 0.2 metres the resonance frequency which is most susceptible to vertical self-excitation becomes 3.5 Hertz.

**Self-excitation due to varying discharge coefficient.** This type is related to horizontal vibrations of the gate in which movement of the gate in downstream direction results in contraction of the flow and therefore a decreasing discharge coefficient (see figure 3.4). This leads to pressure fluctuations in phase with the vibration velocity [7]. This type of self-excitation may occur for Strouhal numbers based on edge width between 0.1 and 1.4 [2]. Figure 3.5 is used to determine susceptibility to self-excitation due to varying discharge coefficient. It is important to note that in the right part of 3.4 only the flow which has an influence on the varying discharge coefficient are shown.

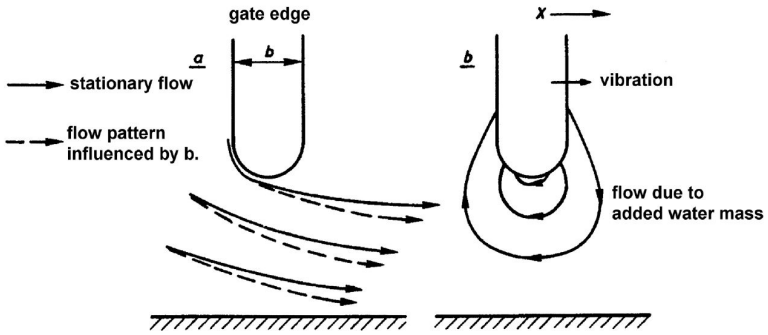


Figure 3.4: Influence of added mass flow on stationary flow [2]

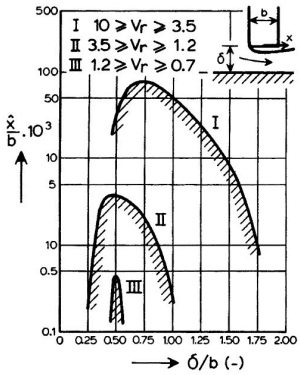


Figure 3.5: Figure used for determining susceptibility to horizontal self-excitation [2]

The Strouhal number is the inverse of the reduced velocity and is now based on the edge thickness since the thickness greatly influences the return current due to the added mass. Equation 3.5 presents the computation of the Strouhal number.

$$S = V_r^{-1} = \frac{fb}{\sqrt{2g\Delta H}} \tag{3.5}$$

In which: $\Delta H$ = Hydraulic head over the gate [m]
Other parameters are shown in the top right of figure 3.5.

**Galopping.** The low-frequency vibrations of electric transmission lines with amplitudes up to three metres have been described by den Hartog [17]. Galloping may occur in cases in which the lift force is depending on the angle of approach of the flow. den Hartog [17] describes the condition for instability as following:

$$\frac{\partial L}{\partial \alpha} + D < 0 \tag{3.6}$$

| | | | | |
|---|---|---|---|---|
| In which: | L | = | Lift force | [N] |
| | $\alpha$ | = | Approach angle of the flow | [°] |
| | D | = | Drag force | [N] |

Which can also be written as [7]:

$$\frac{\partial C_L}{\partial \alpha} + C_D < 0 \tag{3.7}$$

| | | | | |
|---|---|---|---|---|
| In which: | $C_L$ | = | Lift force coefficient | [-] |
| | $\alpha$ | = | Approach angle of the flow | [°] |
| | $C_D$ | = | Drag force coefficient | [-] |

The analysis of galloping of HGs is described by Thang and Naudascher [3] and elaborated in section 3.5.2.

**Type 4: Amplification of the excitation due to the resonant rise of the water.** In case of a body of water having a clear resonance frequency being loaded in its resonance frequency, strong oscillations may occur resulting in even larger dynamic loads on the structure. Clear resonance frequencies of water bodies can be found for instance in case of communicating vessels.

**Type 5: Unstable fluid resonance with self-excitation.** Interaction between the fluid and the structure may lead to unstable fluid resonances, resulting in very high (standing) wave amplitudes. This interaction in terms of water surface levels or water pressure and discharge can result in the amplified reflection of waves, being a form of self-excitation.

Based on this classification Erdbrink [7] proposed an adjusted classification of excitation types for hydraulic gates in which type 1 is split in two different types, being turbulence and stable vortex shedding. Types 4 and 5 are combined in the type: Unstable resonance of the fluid.

## 3.2. DIMENSIONLESS NUMBERS USED IN FLUID-STRUCTURE INTERACTION

In Fluid-Structure Interaction regarding the vibrations of hydraulic gates a number of dimensionless parameters are used.

- The Froude number, being Fr, relates flow velocity to wave celerity;
- The Reynolds number, being Re, determines the influence of viscosity in the flow;
- The Strouhal number, being S, is a measure of excitation frequencies;
- The displacement number, being D, relates the displacement field to the solid's length scale;
- The fluid timescale, being $T_f$, is a measure of the speed of fluid dynamics;
- The solid timescale, being $T_s$, is a measure of the speed of solid dynamics;
- The reduced velocity, being $U_r$, relates the time scales of the fluid and solid;
- The Courant number, being C, is a measure of the mesh size in relation to the time step.

These dimensionless numbers are computed as following:

| | | |
|---|---|---|
| Fr | = | $U_0/\sqrt{gh}$ |
| Re | = | $\rho_f U_0 t_s/\mu$ |
| S | = | $f_f t_s/U_0$ |
| D | = | $\xi_0/L$ |
| $T_f$ | = | $t_s/U_0$ |
| | or | $1/f_f$ |
| $T_s$ | = | $1/f_s$ |
| $U_r$ | = | $T_s/T_f$ |
| C | = | $\Delta t \sum_{i=1}^{n} \frac{U_{x_i}}{\Delta x_i}$ |
| In which: | | Subscript i denotes the dimension [-] |
| | | Subscript n denotes the number of dimensions [-] |

The following parameters are used:

| | | | |
|---|---|---|---|
| $U_0$ | = | Flow velocity | [m/s] |
| g | = | Gravitational acceleration | $[m/s^2]$ |
| h | = | Water depth | [m] |
| L | = | Length measure, such as the height of the solid in case of vertical vibrations or the thickness of the solid in case of horizontal vibrations | [m] |
| $\rho_f$ and $\rho_s$ | = | Densities of the fluid and solid respectively | $[kg/m^3]$ |
| $t_s$ | = | Thickness of the solid | [m] |
| $\mu$ | = | Dynamic viscosity of the fluid | $[Ns/m^2]$ |
| $\xi_0$ | = | Vibration amplitude | [m] |
| $f_f$ and $f_s$ | = | Frequency of fluid fluctuations or of vibrations of the solid | [Hz] |
| $\Delta t$ | = | Time step | [s] |
| $U_{x_i}$ | = | Component of the flow velocity in $x_i$-direction | [m/s] |
| $\Delta_{x_i}$ | = | Mesh size in $x_i$-direction | [m] |

## 3.3. ASSUMPTIONS AND SIMPLIFICATIONS

It is assumed that only small vibrations will occur. This means that the displacement number, being D, is much smaller than one: $1 \gg D$. By doing this, one can neglect higher order terms. This assumption is almost always valid since small vibrations are already undesirable and should therefore be avoided before small vibrations can have an increasing amplitude, such as in case of self-excitation.

In the general case neither the fluid flow velocity nor the velocity of the solid is negligible, a fully coupled system between the fluid dynamics and the solid dynamics is present meaning that the movement of the fluid has an influence on the movement of the solid and vice versa. In this case the interface between the fluid and solid are coupled in terms of kinematic conditions and dynamic conditions.

In case of the solid dynamics being slower, but not a lot slower, than the fluid dynamics the solid velocity cannot be neglected. In this situation the deformation or displacement is variable and a constant, so frozen, solid velocity is present. This case can be approached using so-called "psuedo-static aeroelasticity". Psuedo-static aeroelasticity is valid for cases in which the squared reduced velocity is much larger than the displacement number: $U_r^2 \gg D$. In this case the fluid is loading the solid at the fluid-solid as a function of the position and velocity of the fluid-solid interface.

In the case of the solid dynamics being a lot slower than the fluid dynamics one can simplify the situation a lot by neglecting the solid velocity and only looking at situations of the solid in different frozen positions / deformation states, so in this case the solid does not have a velocity. This case can be approached using so-called "quasi-static aeroelasticity". This case is only valid in case the reduced velocity is much larger than the displacement number: $U_r \gg D$. In this case the fluid delivers a load to the interface with the solid given a certain position of the fluid-solid interface.

## 3.4. INFLUENCE OF THE SURROUNDING WATER ON DYNAMIC BEHAVIOUR

This section is used to discuss the influence of the surrounding water on the basic dynamical system, being a one degree of freedom system, which is discussed in appendix A. Background information of structural dynamics can be found in appendix A in which the basic principles are explained. Figure 3.6 shows the situation of the dynamic system in which the rigid body can experience vibrations in the horizontal as well as vertical direction (black arrows) due to the water flow underneath the structure (blue arrow). The stiffness and damping of the suspension are schematised into a spring and a dashpot respectively.

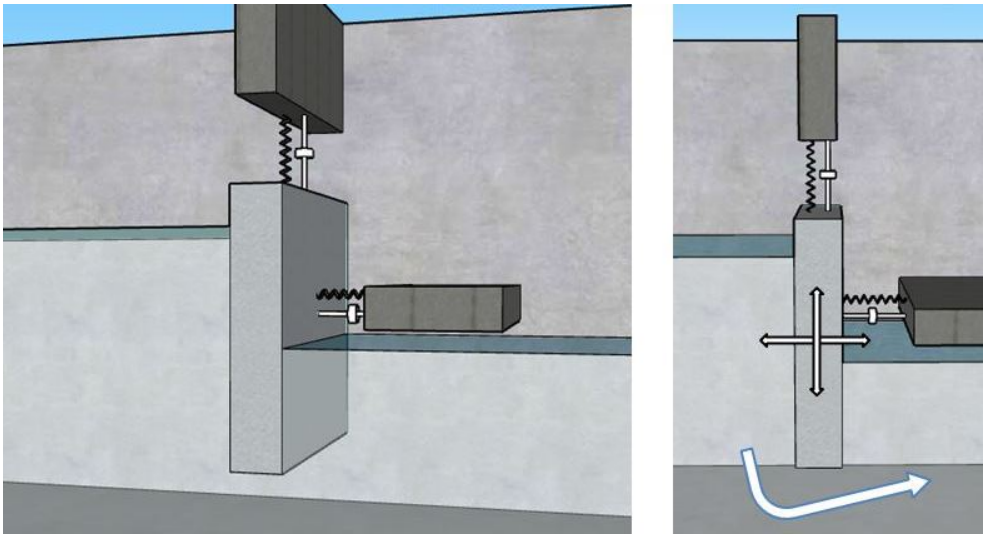

Figure 3.6: Overview of the dynamic situation

### 3.4.1. GENERAL INFORMATION

In general hydraulic structures such as hydraulic gates are surrounded by water. Due to the vibration of the structure the surrounding water is moved back and forth. This surrounding water changes the dynamic properties of the system at hand in terms of the mass, stiffness and damping. This translates into an added water mass, added stiffness and added damping. The added stiffness and added damping may as well be negative, for instance in case of self-excitation, as described in section 3.1.

The model as shown figure 3.7 is obtained when:

- It is assumed that the dynamic force is solely depending on time;
- The linear combination of the dynamic properties of the previous model and the added terms, using the principle of superposition, is valid.

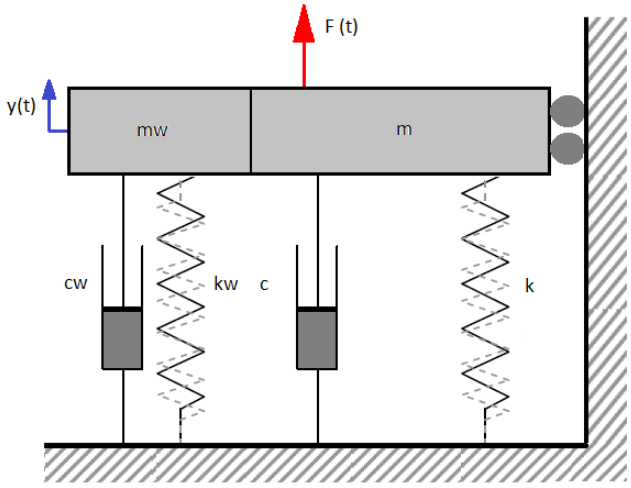


Figure 3.7: Model with added terms for a 1-DOF system

This yields the equation of motion shown in equation 3.8.

$$(m+m_w)\frac{d^2y}{dt^2}+(c+c_w)\frac{dy}{dt}+(k+k_w)y=F(t) \tag{3.8}$$

Which for the undamped situation results in the natural frequency as shown in equation 3.9.

$$f_n=\frac{\omega_n}{2\pi}=\frac{1}{2\pi}\sqrt{\frac{(k+k_w)}{(m+m_w)}} \tag{3.9}$$

This is in fact a very simplified approach, since the added terms are not constant but may vary in time and space and could also be frequency dependent [2]. Also the force might depend not only on time but also on spatial coordinates, time derivatives and other variables. The application of the principle of superposition on flow patterns for permanent flow and the flow due to the vibrating structure resulting in added damping is not yet verified [2].

Section 3.4.2 will be used to elaborate the added terms due to the presence of water around the vibrating structure.

### 3.4.2. COMPUTATION OF THE ADDED HYDRODYNAMIC MASS, STIFFNESS AND DAMPING.

In this section the hydrodynamic mass, stiffness and damping are elaborated. Regarding horizontal vibrations the added mass and damping are mentioned. The added hydrodynamic mass, damping and stiffness are elaborated for vertical vibrations.

ADDED HYDRODYNAMIC MASS FOR A HORIZONTALLY VIBRATING DAM ACCORDING TO WESTERGAARD [5].
Hydrodynamic pressures occurring at horizontally vibrating hydraulic gates have recently been researched by Versluis [28] and Tieleman [6]. Versluis [28] has focussed on the hydrodynamic forces in case of earthquakes and has used the method as described by Westergaard [5] for the case of pressure fluctuations at a vertical dam during earthquakes. In order to obtain the simplest way of determining the added mass assumptions made by Westergaard [5] were the following:

- The dam is rigid (infinitely stiff) and infinitely long, justifying a two-dimensional approach;
- The water reservoir is infinitely long, resulting in a negligible influence of the boundaries;
- There is atmospheric pressure at water level, the impact of waves is neglected and there is no water displacement in vertical direction at the water level;
- The water is incompressible.

The latter two of the assumptions result in the direct response of the system. Therefore, the hydrodynamic pressure fluctuations are independent of the frequency. Tieleman [6] showed that the assumption of incompressible flow holds for excitation frequencies up to around 30% of the fundamental resonance frequency of water which is described as following:

$$f_n = \frac{1}{T_n} = \frac{c_p}{4h} \tag{3.10}$$

| | | | | |
|---|---|---|---|---|
| In which: | $f_n$ | = | Fundamental resonance frequency of water | [Hz] |
| | $T_n$ | = | Fundamental resonance period of water | [s] |
| | $c_r$ | = | Pressure wave celerity in water | [m/s] |
| | h | = | Water depth | [m] |

The celerity of pressure waves, i.e. the speed of sound propagation, in water is approximately 1500 [m/s]. For a chosen water depth of 10 metres one finds that the fundamental resonance frequency of water becomes 37.5 Hertz. So in case of a water depth of 10 metres the assumption of incompressible flow is valid for vibration frequencies up to approximately 11 Hertz. For vibration frequencies higher than 30 % of the fundamental resonance frequency of the fluid fluid compressibility should be included.

Westergaard [5] came up with the following simplified expression to describe hydrodynamic pressures over the depth.

$$p(z) = \frac{7}{8}\rho g k_h \sqrt{zh} \tag{3.11}$$

| | | | | |
|---|---|---|---|---|
| In which: | p(z) | = | Hydrodynamic pressure as a function of the water depth | $[N/m^2]$ |
| | $\rho$ | = | Density of water | $[kg/m^3]$ |
| | g | = | Gravitational acceleration | $[m/s^2]$ |
| | $k_h$ | = | Horizontal seismic coefficient | [-] |
| | z | = | Vertical coordinate in the water column | [m] |
| | h | = | Water depth | [m] |

The horizontal seismic coefficient is computed as the ratio between the ground's horizontal acceleration underneath the dam and the gravitational acceleration, being $a_h/g$. The vertical coordinate, being z, is equal to zero for the water surface and equal to the water depth at the reservoir bed level. The horizontal ground acceleration can be used as a unit acceleration by setting it to one. Dividing equation 3.11 by the gravitational acceleration transforms it into an added mass.

$$m_w(z) = \frac{7}{8}\rho\sqrt{zh} \tag{3.12}$$

| | | | | |
|---|---|---|---|---|
| In which: | $m_w(z)$ | = | Added water mass as a function of the water depth | $[kg/m^2]$ |

When the added mass as a function of the depth is integrated over the depth and multiplied by the width of the structure one will find the added mass of the water for both sides of the hydraulic gate. Important to note is that equation 3.13 holds only for fully closed hydraulic gates, i.e. no water flow can occur underneath the structure. When flow occurs underneath the structure the added mass changes. In equation 3.13 subscript " i " denotes the two sides of the gate.

$$m_w = \sum_{i=1}^{i=2} \int_{z_i=0}^{z_i=h_i} \frac{7}{8} \rho w \sqrt{z_i h_i} dz = \sum_{i=1}^{i=2} \frac{7}{12} \rho w \sqrt{h_i} * [z_i^{1.5}]_0^{h_i} = \sum_{i=1}^{i=2} \frac{7}{12} \rho w h_i^2 \tag{3.13}$$

In which: $m_w$ = Added water mass [kg]
w = Width of the HG [m]

Versluis [28] concludes that the bending stiffness of the hydraulic gate may have a large influence on the hydrodynamic pressure distribution. He also states that surface waves only have a little influence on the pressure distribution resulting in the justified assumption of atmospheric pressure at the water surface. Versluis [28] (Figure 4.7 in his thesis) also shows that for reservoir lengths of four times the water depth, the added water mass is only reduced by approximately 10 %. A reservoir length of six times the water depth results in a negligible decrease of the added water mass.

The equations shown in this paragraph are applicable to hydraulic gates which undergo rigid body vibrations under flow-induced vibrations with a frequency up to 30% of the fundamental resonance frequency of water. According to Tieleman [6] the flexibility of the gate leads to horizontal vibration mode shapes and a three dimensional problem, thus invalidating the assumption of a two dimensional problem. Therefore, Tieleman [6] executed a three dimensional analysis. This is further addressed in section 4.3.3.

#### ADDED HYDRODYNAMIC MASS FOR A HORIZONTALLY VIBRATING HYDRAULIC GATE ACCORDING TO KOLKMAN AND JONGELING [2].

In Kolkman and Jongeling [2] the horizontal added mass is given for certain situations such as a horizontally vibrating gate which is positioned on a floor and the added mass for a horizontally vibrating ship.

Based on extensive measurements performed at Delft Hydraulics, the former name of Deltares, figure 3.8 (figure A3.1 in Kolkman and Jongeling [2]) shows the added mass for different natural gate frequencies (left) and for high frequencies (right), both with water on one side. For cases of fully closed hydraulic gates the left figure can be used. For $\psi = \omega^2 h/g \leq 100$ the added mass is frequency dependent due to the influence of surface wave radiation while for higher frequency vibrations, pressure fluctuations due to surface waves do not penetrate deep into the water column. As stated by Kolkman and Jongeling [2] vibrating structures usually have natural frequencies high enough for the added water mass to become frequency independent. It can be seen that for an increasing vibrating frequency the added mass also increases. Relative differences are largest for gates with a height equal to the flow depth, i.e. $h/d = 1$. As stated in Kolkman and Jongeling [2]: for cases of high frequency vibrations (with $\psi$ values of over 100) of a gate with a height equal to the water depth, i.e. $h1/h2 = 1$, the right part of figure 3.8 corresponds with results found by Westergaard [5] in which a rigid body vibration is assumed. Whether this statement is correct or not will be checked further on in this section.

Figure 3.8 shows that the added mass does not change much with values of $\psi$ larger than ten, which is also mentioned by Kolkman and Jongeling [2], i.e. even though surface wave radiation is not negligible the effect on the added mass is still not clearly visible. The added mass per unit of width for a gate with water on one side as computed using both Westergaard [5] (equation 3.14) and Kolkman and Jongeling [2] (equation 3.15) are now compared to see if they are in fact the same as stated by Kolkman and Jongeling [2].

$$m_w = \frac{7}{12} \rho h_1^2 \approx 0.583 \rho h_1^2 \tag{3.14}$$

$$m_w = C_L \rho h_1^2 = 0.542 \rho h_1^2 \tag{3.15}$$

In which: $m_w$ = Added mass per unit of width

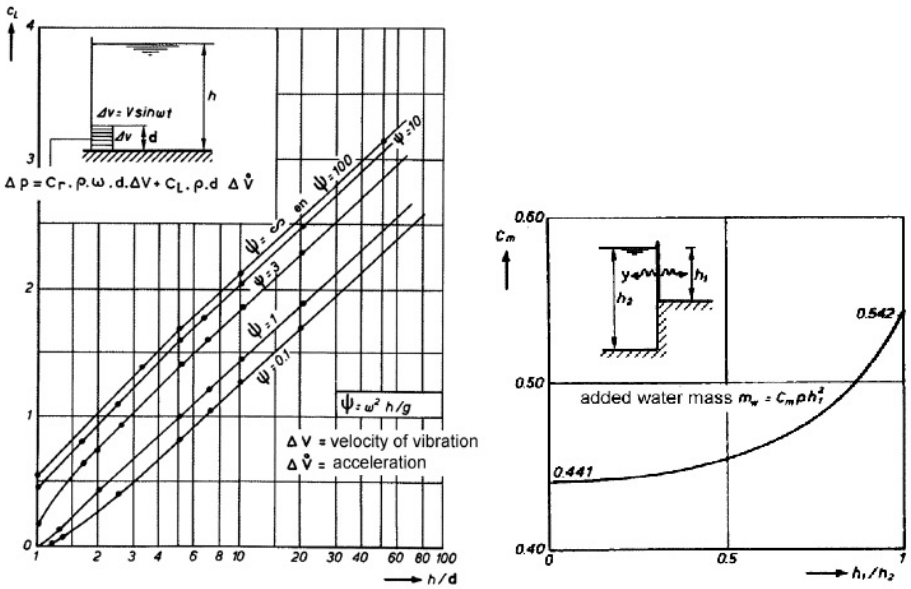


Figure 3.8: (L) Added mass as a function of frequency and (R) for high frequencies [2]

Which shows that there is a small difference between the two computations. This difference might originate from the simplified formula written by Westergaard [5]. Also the negligence of wave radiation using Westergaard [5] while Kolkman and Jongeling [2] take wave radiation into account, incorporated into figure 3.8. Kolkman and Jongeling [2] also neglect pressure variations due to waves. What is interesting to note as well, is that the assumption of incompressible flow as mentioned by Westergaard [5] is only valid for low vibration frequencies, up to about 30 % of the fundamental resonance frequency of the water body [6], while the right part of figure 3.8 is only valid for high vibration frequencies, i.e. $\psi = \omega^2 h/g \geq 100$, in which $\psi$ is a dimensionless measure of the vibration frequency. As mentioned in paragraph 3.4.2 a fundamental resonance frequency of the water body for a depth of 10 metres is equal to 37.5 Hertz with the validity of the assumption of incompressible flow for vibrations up to 11 Hertz. In the case of a 10 metre water depth and a vibration frequency up to 11 Hertz, using Kolkman and Jongeling [2] one finds: $\psi = \omega^2 h/g = 11^2 * 10/g \approx 123$ which is indeed larger than 100. This concludes that for this case the assumption of negligible influence of surface waves which confirms that indeed both computations are similar.

For situations in which the hydraulic gate is almost completely opened, figure 3.9 (figure A3.5 in Kolkman and Jongeling [2] provides a rule of thumb. This holds for large gate openings in which the submerged part of the gate is small compared to the water depth, which will further be referred to as the "ship-type" of added mass.

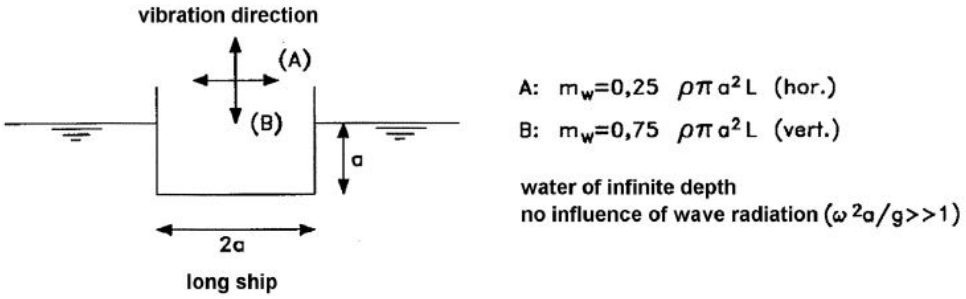


Figure 3.9: Added mass for a vibrating ship [2]

In case of a partially submerged hydraulic gate, water is present beneath the gate since the gate does not touch the floor or sill. When the gate is vibrating horizontally a return current appears. At low vibration frequencies the return current underneath the gate (moving in opposite direction of the vibration direction) is able move all of the displaced water due to the vibrating gate from one side to the other which results in the decrease of radiated waves. The influence of a partially opened hydraulic gate is elaborated further in section 4.3.3.

#### COMPUTATION OF THE ADDED HYDRODYNAMIC WATER MASS FOR A VERTICALLY VIBRATING HYDRAULIC GATE ACCORDING TO KOLKMAN AND JONGELING [2]

Kolkman and Jongeling [2] describes two different calculation methods for determining the hydrodynamic mass for a vertically moving HG, both being two limit cases; an almost closed HG and a HG which is almost fully opened. First of all the hydrodynamic mass for a vertically moving HG can be computed using the formula presented in figure 3.9 for which the same validity holds as described in the previous section.

Secondly the hydrodynamic mass can be computed for the case in which the opening height is small with respect to the thickness of the HG. Figure 3.10 shows an overview of the almost closed HG and accompanying formulas. The $C_L$-coefficient that is mentioned in figure 3.10 can be obtained using figure 3.8 in which the $C_L$-coefficient used in the formula presented in figure 3.10 is equal to the summation of $C_L$-coefficients for the upstream and downstream side of the HG.

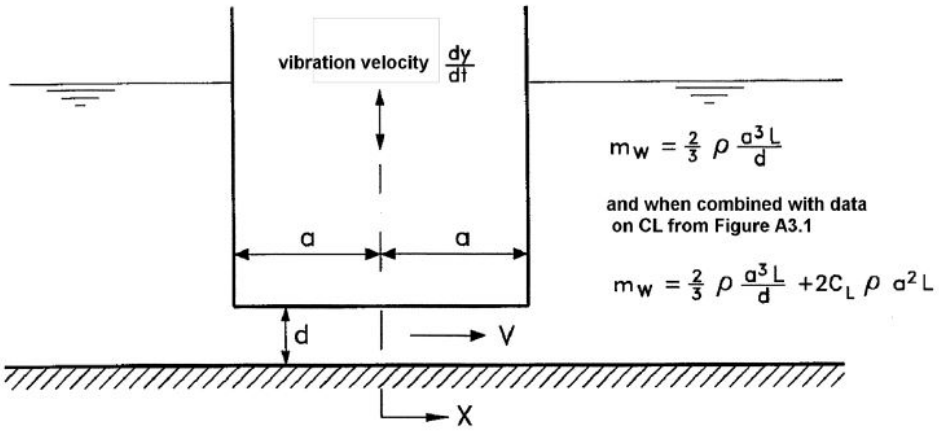


Figure 3.10: Added mass for an almost closed vertically moving HG [2]

### 3.4.3. COMPUTATION OF VERTICAL ADDED HYDRODYNAMIC WATER STIFFNESS ACCORDING TO KOLKMAN AND JONGELING [2]

This section describes the definition of stiffness, stiffness due to buoyancy and flow and the so-called sudden stiffness. By definition stiffness is equal to:

$$k = \frac{\partial F_y}{\partial y} \tag{3.16}$$

| In which: | | | | |
|---|---|---|---|---|
| | $k$ | = | Stiffness | $[N/m]$ |
| | $F_y$ | = | Force in y-direction | $[N]$ |
| | $y$ | = | Position | $[m]$ |

In case of a hydraulic gate which is partially submerged a certain upward water pressure acts on the bottom of the structure. When pushed down the upward force is increased proportional to the vertical displacement. This force divided by gate's displacement results in the so-called " vertical stiffness " and is described by Kolkman and Jongeling [2] as following:

$$k_{w-float} = \rho g A_{cross-section} \tag{3.17}$$

| In which: | | | | |
|---|---|---|---|---|
| | $A_{cross-section}$ | = | The water piercing surface of the hydraulic gate | $[m^2]$ |

The stiffness due to flow can be described as follows:

$$k_{w-flow} = \frac{1}{2}\rho V^2 L^2 \frac{\partial C_{Fy}}{\partial y} \tag{3.18}$$

| In which: | | | | |
|---|---|---|---|---|
| | V | = | Flow velocity | [m/s] |
| | $L^2$ | = | Surface area excited by approach flow | $[m^2]$ |
| | $C_{Fy}$ | = | Coefficient accounting for the component of the flow force in y-direction | |

Since the flow velocity is proportional to the square root of the hydraulic head difference between the upstream and downstream side of the hydraulic gate, the stiffness due to flow is proportional to the hydraulic head difference.

Another contribution to added water stiffness is the so-called " sudden stiffness " which only occurs at gates in cases when the discharge has a large inertia making it unable to directly adapt to the displacement of the gate. This occurs mainly at culvert gates [2] due to the large inertia of the water present in the culvert. For high frequency vibrations the flow is unable to adapt to the fluctuating gap width. Since the flow is unable to directly adapt to an increasing or decreasing gap this means that same discharge flows through a larger or smaller gap, increasing from $\delta$ to $\delta+\gamma$, with $\delta$ being the gap width and $\gamma$ being the fluctuations of the gap height due to the vibrating gate. This means that the flow velocity fluctuates as well and therefore the force changes quadratically (as in equation 3.18) in the following manner:

$$F_{dynamic} = F_{static}\frac{\delta^2}{(\delta+\gamma)^2} \tag{3.19}$$

| In which: | | | | |
|---|---|---|---|---|
| | $F_{dynamic}$ | = | Dynamic flow force due to inertia | [N] |
| | $F_{static}$ | = | Static flow force | [N] |
| | $\delta$ | = | Gap width in static state | [m] |
| | $\gamma$ | = | Fluctuations in gap width due to the opening gate | [m] |

In case of small vibration amplitudes, i.e. $\gamma$ is small compared to $\delta$, and assuming a constant discharge coefficient the differences between the dynamic and static flow force over the displacement can be approximated by:

$$k_{sudden} = 2\frac{F_{static}}{\delta} \tag{3.20}$$

This means that for a smaller gap width the sudden stiffness is larger. The sudden stiffness is positive for gates located at downstream of a culvert and negative for gates located upstream of a culvert. When the negative sudden stiffness is larger than the mechanical stiffness, suction closes the gate.

### COMPUTATION OF ADDED WATER DAMPING FOR A HORIZONTALLY VIBRATING HYDRAULIC GATE ACCORDING TO KOLKMAN AND JONGELING [2]

This section describes the damping presented by Kolkman and Jongeling [2]. By definition damping is the following:

$$c = \frac{\partial F_y}{\partial \frac{dy}{dt}} \tag{3.21}$$

| In which: | | | | |
|---|---|---|---|---|
| | $c$ | = | Damping | $[Ns/m]$ |
| | $F_y$ | = | Force in y-direction | $[N]$ |
| | $\frac{dy}{dt}$ | = | Velocity in y-direction | $[m/s]$ |

Unlike the hydrodynamic mass, damping due to wave radiation decreases for increasing vibration frequencies. This is the case since higher frequency vibrations produce shorter waves which have a smaller influence on the pressure due to a smaller penetration depth. Where the added mass reaches a maximum around $\psi \geq 100$ the damping already approximates zero for values of $\psi \geq 10$ as can be seen in figure 3.11. As mentioned before structures usually vibrate at a high frequency resulting in low water damping due to wave radiation.

Added water damping for a gate with water on one side is computed as following:

$$c_w = C_r \rho \omega h_1^2 \tag{3.22}$$

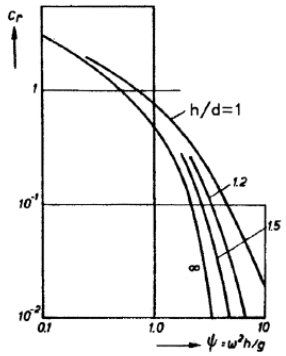


Figure 3.11: Added damping as a function of the natural frequency [2]

In which: $c_w$ = Added water damping per metre width [$Ns/m$]
$C_r$ = Radiation coefficient [N]

Although it seems that the damping increases for larger frequencies, $C_r$ has a larger influence while decreasing for larger values of $\omega$. For a horizontally vibrating deep gate the water damping due to wave radiation on one side is equal to:

$$c_w = \frac{2\rho g^2}{\omega^3} \tag{3.23}$$

For this expression it also holds that for water on both sides of the hydraulic gate the total added water damping is twice as high.

## 3.5. RELATED RESEARCH

In this section two researches regarding fluid-structure interaction are mentioned. First of all a recent experimental research regarding vertical vibrations of a HG with different shapes of the HG's underside is shown in section 3.5.1 after which an interesting research regarding the quasi-static analysis of galloping-type self-excited vibrations is introduced in section 3.5.2.

### 3.5.1. EXPERIMENTS PERFORMED BY TOM KOREVAAR [4]

Tom Korevaar [4] has conducted his experiments regarding vertical vibrations of hydraulic gates due to underflow for different seal shapes, being shown in figure 3.12. The seal is a rubber strip installed on the bottom of the gate used to completely close the HG.

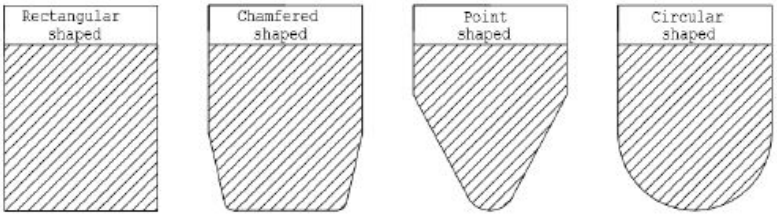


Figure 3.12: Different seal shapes used in the conducted experiments [4]

Results obtained from his experiments are shown in appendix B. Obviously no vertical vibrations occurred for tests with an infinite vertical stiffness. What is interesting to see is that the conducted experiments with the lowest stiffness, being 1.16 N/mm, and therefore the lowest natural frequency show the least peaks in the measured variables while usually a higher natural frequency means a lower susceptibility to vibrations. Percentages of experiments conducted with different stiffnesses which show clear peaks, obtained from table B.1 until table B.5 are the following:

- For experiments with a stiffness of 1.16 N/mm, two experiments out of eleven show clear peaks in the measured variables: 18 %;
- For experiments with a stiffness of 5.34 N/mm, thirteen experiments out of twenty show clear peaks in the measured variables: 65 %;
- For experiments with a stiffness of 15.66 N/mm, five experiments out of nine show clear peaks in the measured variables: 56 %;
- For experiments with a stiffness of 43.20 N/mm, eight experiments out of twelve show clear peaks in the measured variables: 67 %;

Natural frequencies in wet condition computed using the dry natural frequency and theoretical added mass and added stiffness do not comply with results obtained by Korevaar [4]. Korevaar [4] notes that the wet natural frequency due of the hydraulic gate are different from what was expected.

Computing the added mass using the dry and wet natural frequencies as measured by Korevaar [4] and a theoretical added stiffness due to buoyancy would yield a negative added mass for some of the combinations of different opening heights and water levels.

Kolkman and Jongeling [2] is used to determine the natural frequencies for all experimental water levels and gap heights and excitation frequencies. All natural frequencies are lower than the excitation frequencies determined using the graph for the determination of the Strouhal number, being figure 3.2. As mentioned in section 3.1 the resonance frequency should be a factor two to three higher than the dominant excitation frequency, which is not the case for any of the experiments which is done on purpose in order for the flow to generate vibrations.

### 3.5.2. ANALYSIS ON GALLOPING ACCORDING TO THANG AND NAUDASCHER [3]

Thang and Naudascher [3] state that vibrations attributed to varying gap height by Kolkman [16] can definitely be present but do not appear to be the most important source of cross-flow hydraulic gate vibrations since in contrary to self-excited vibrations due to the varying gap width, oscillations might also occur for large gap heights in which no suction occurs. Thang and Naudascher [3] also state that self-excited vibrations of vertical lift gates show behaviour similar to the galloping of rectangular prisms in unconfined flow.

Galloping can be modelled using the quasi-steady approach in which the incidence flow velocity due to movement of the gate is reproduced by positioning the gate under an angle $\alpha$ being computed as: $\alpha = tan^{-1}(\dot{y}/V)$. In which $\dot{y}$ is the velocity of the moving hydraulic gate and $V$ is the velocity of the flowing water in the vena contracta. Figure 3.13 shows an example of the streamline pattern for a vertically moving prism and hydraulic gate with a velocity of half of the flow velocity. In the case of the hydraulic gate the flow velocity in the vena contracta is used. The dashed lines show the stationary situation for a non-moving structure while the continuous line shows the streamlines for the moving structure using the quasi-steady approach. The blue lines indicate the water levels upstream and downstream of the HG. The brown line indicates the bottom of the structure.

Thang and Naudascher [3] determined the lift coefficient as a function of the incidence angle, which depends on the flow velocity and the velocity of the moving hydraulic gate, for different gap heights. The angle at which the HG is positioned is equal to the incidence angle. The expression for the lift coefficient is shown in equation 3.24.

$$C_L = \frac{1}{d}\int_{x=0}^{d} \frac{h_i - h_2}{h_1 - h_2}\,dx \tag{3.24}$$

| | | | | |
|---|---|---|---|---|
| In which: | $C_L$ | = | Mean lift coefficient over the underside of the hydraulic gate | $[-]$ |
| | $d$ | = | Thickness of the hydraulic gate | $[m]$ |
| | $h_i$ | = | Local piezometric head at the gate underside | $[m]$ |
| | $h_1$ | = | Upstream water level | $[m]$ |
| | $h_2$ | = | downstream water level | $[m]$ |

Thang and Naudascher [3] state that an important indicator of instability is the slope of the lift coefficient as a function of the incidence angle about the equilibrium as shown in equation 3.25. The value of $A_1$ determines if the upward force on the HG increases or decreases when the HG is moved from a certain (static) equilibrium position, i.e. if a change in the velocity of the HG results in a larger of smaller upward force and therefore a positive damping or negative damping of the movement.

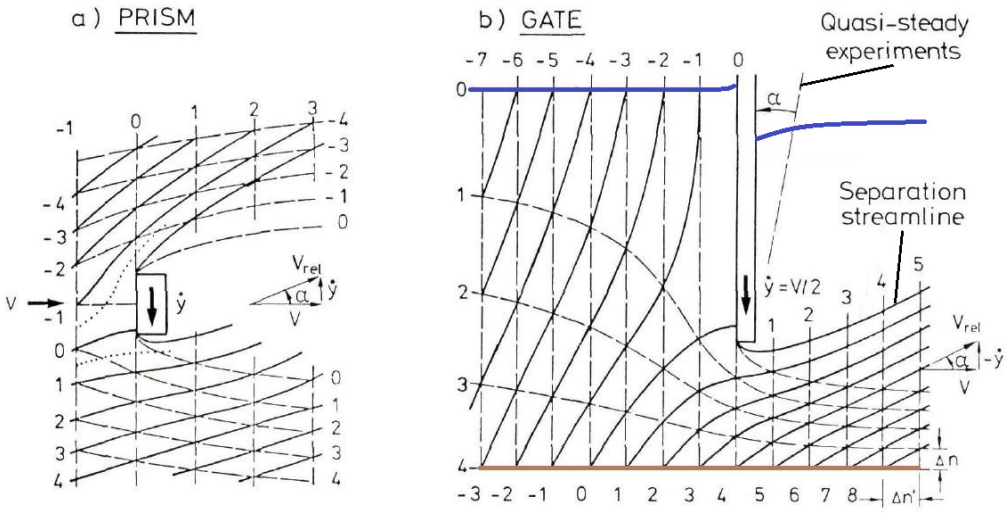


Figure 3.13: Streamline pattern for a prism and a hydraulic gate [3] (adjusted)

$$A_1 = \left.\frac{\partial C_L(\alpha)}{\partial \alpha}\right|_{\alpha=0} \tag{3.25}$$

For $A_1 > 0$ soft-galloping may occur in which vibrations may develop at a certain critical reduced velocity. For $A_1 \leq 0$ the structure is either stable or unstable in the form of hard-galloping based on the shape of the mean-lift curve. The mean-lift curve as a function of the gap ratio and the slope of the lift curve as a function of the incidence angle about the equilibrium are shown in figure 3.14. The figure shows results for four gates with a different inclination angle of the upstream baffle.

Figure 3.15 shows the lift coefficient as a function of the inclination angle for a gap-ratio of 0.65, described as the critical gap-ratio, which is used to determine the third order polynomial approximation and consequently the stability indicator, $A_1$.

Figure 3.16 shows the results obtained from experiments regarding the dimensionless vibration amplitude, $y_0/d$, as a function of the gap ratio. In this figure the full symbols refer to hard-galloping of the hydraulic gate.

Combining figure 3.14 and figure 3.16 the following is concluded by Thang and Naudascher [3]:

- The gate was stable for negative slopes of $C_L$ as a function of $(s/d)$ or negative values of A1 both in rest as with large trigger amplitudes;
- A positive slope for $C_L$ as a function of $(s/d)$ can be used as an instability indicator;
- The $C_L$ curve as a function of $s/d$ can be easily derived from static model tests and used for the possible prediction of self-excited hydraulic gate vibrations;
- For an inclination angle, $e/d$, of 1.0 the gate is completely stable;

## 3.6. CONCLUSIONS

The main conclusions that can be drawn are the following:

- There are many sources of excitation of which the most undesirable type is self-excitation, in which the forces are in phase with the movement of the hydraulic gate and amplify the movement up to the point where the hydraulic gate hits a wall. Preventing self-excitation is the main priority in the design of a hydraulic gate. Therefore, the rest of this thesis will focus on self-excitation;

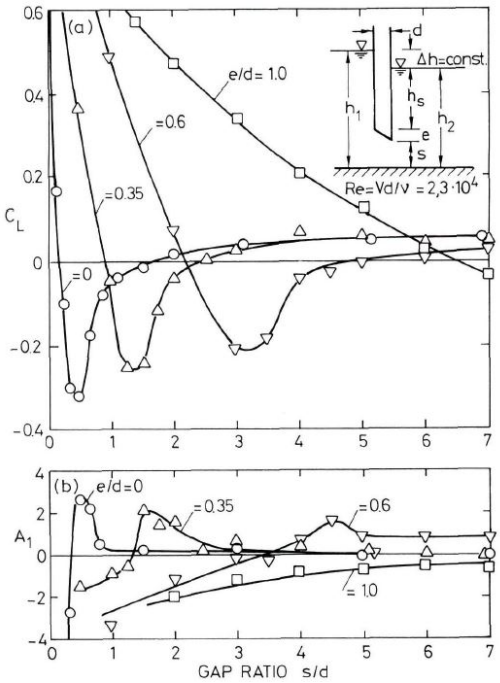


Figure 3.14: Experimentally determined lift coefficients and the stability indicator as a function of the gap ratio, being s/d [3]

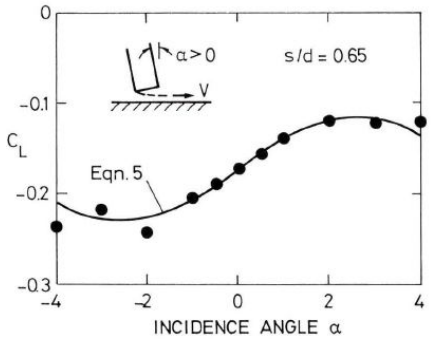


Figure 3.15: Experimentally determined lift coefficients and the fitted curve as a function the inclination angle, being $\alpha$ [3]

- A valuable simplification can be found in the quasi-static aeroelasticity approach. For this approach the fluid dynamics has to be a lot faster than the solid dynamics. Also the reduced velocity has to be much larger than the displacement number, as mentioned in section 3.3. In section 3.5.2 a method using this approach is presented. This method can be used to predicht flow-induced galloping-type vibrations during the design process;
- A a dynamic system can often be modelled as a mass-spring-damper system in which the dynamic properties of a system are parametrised. Resulting from the parametrisation an equation of motion can be drawn up after which the harmonic vibration and accompanying natural frequency can be found;
- The surrounding water influences the dynamic properties of the hydraulic structure in terms of mass, stiffness and damping. This results in a different natural frequency than for the same hydraulic structure in air;

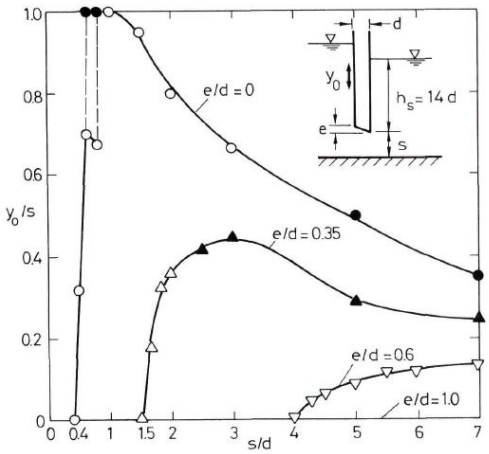


Figure 3.16: Experimentally determined dimensionless oscillation amplitudes as a function of the gap ratio, being s/d [3]

# 4

# COMPARISON OF AN FRP AND STEEL TEST CASE

In order to check what the influence of the use of FRP on the dynamic properties of structures a simple test case is assessed in this chapter. This chapter builds on results from chapter 3 regarding basic principles in fluid-structure interaction, chapter 2 regarding FRP as a building material. General information regarding the chosen test case is shown in section 4.1. In section 4.2 the dynamic properties of a steel plate is compared to a plate made of Glass Fibre-Reinforced Polymer (GFRP) as well as a plate made of Carbon Fibre-Reinforced Polymer (CFRP) in a dry condition. The added mass for the horizontally vibrating HG is computed in section 4.3. In section 4.4 the HGs are compared in a wet condition, i.e. including the influence of the added mass on the dynamic properties of the HGs. The influence of orthotropic material properties of FRP is further elaborated in section 4.5 after which conclusions are drawn in section 4.6.

## 4.1. GENERAL INFORMATION

The geometry of the chosen test case is a vertical HG which is simply supported along both vertical edges. The case is assessed in dry condition and in wet condition. Figure 4.1 shows the situation in wet condition.

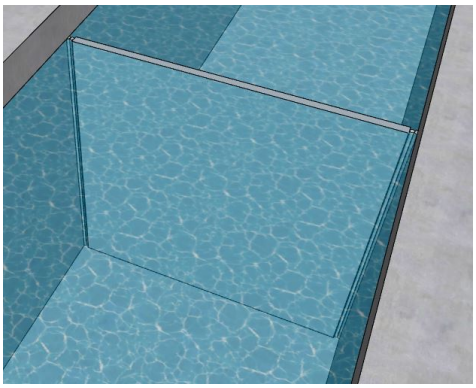

Figure 4.1: Bird's-eye view of the hydraulic gate

Figure 4.2 shows the bird's-eye view of the HG in dry situation.

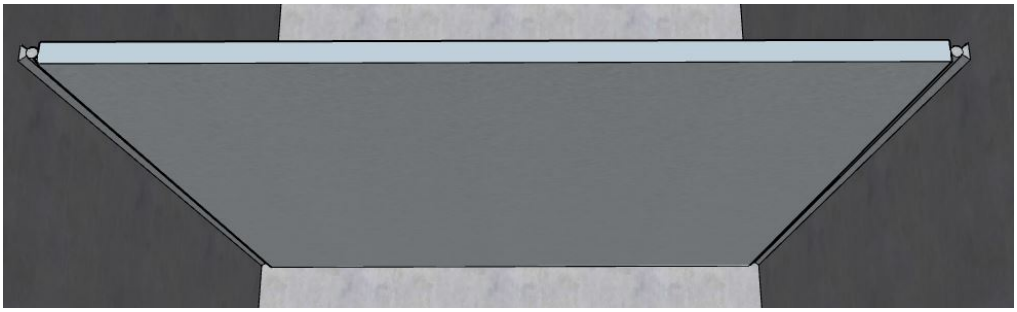

Figure 4.2: Bird's-eye view of the mechanical system

The analytical derivation of the natural frequencies and the deflection due to a line load with a total magnitude of one mega Newton at midspan is performed for a steel HG as well as HGs made out of GFRP and CFRP. In this test case the HG is analysed as a simply supported beam with mode shapes in longitudinal direction. Vibration modes other than beam modes are discussed in section 4.5.

For the two composite materials a HG with the same length and width as the steel HG is assessed. The HG is kept isotropic by aligning all fibres in span direction which is the most beneficial for the stiffness and strength in span direction. The influence of orthotropic properties of FRP is discussed in section 4.5.

## 4.2. ANALYSIS OF A STEEL HG, GFRP HG AND A CFRP HG IN DRY SITUATION

This section concerns the difference in dynamic properties between a steel HG, GFRP HG and CFRP HG in a dry situation. In section 4.2.1 a steel HG is assessed after which the GFRP HG is discussed in section 4.2.2 and a CFRP plate is discussed in section 4.2.3.

### 4.2.1. STEEL HG

The input parameters for the steel HG are shown in table 4.1.

Table 4.1: Input parameters steel plate

| | | | | |
|---|---|---|---|---|
| **Width (span direction)** | w | = | 5.0 | [m] |
| **Height** | h | = | 5.0 | [m] |
| **Density** | $\rho$ | = | $7.85 * 10^3$ | $[kg/m^3]$ |
| **Thickness** | t | = | 0.2 | [m] |
| **Mass** | m | = | $37.5 * 10^3$ | [kg] |
| **Yield stress** | $\sigma_y$ | = | $235 * 10^6$ | [Pa] |
| **Young's modulus** | $E_s$ | = | $210 * 10^9$ | [Pa] |
| **Poisson factor** | $\nu$ | = | 0.3 | [-] |

#### HG ASSESSMENT

The bending stiffness of the HG, denoted as EI, is determined by multiplying the moment of inertia with the Young's modulus: $EI = Eht^3/12 = 7.0 * 10^8 [Nm^2]$. The natural frequencies are computed as done in example 13.2 in Craig Jr. and Kurdila [29]:

$$f_n = \frac{\pi}{2} n^2 \sqrt{\frac{EI}{\rho w^4 th}} \tag{4.1}$$

| | | | | |
|---|---|---|---|---|
| In which: | $f_n$ | = | Natural frequency for mode n | [Hz] |
| | n | = | Vibration mode numbering from one to infinity | [-] |

The first five natural frequencies are computed to be the following:

Table 4.2: Natural frequencies found for the steel HG

| | | | |
|---|---|---|---|
| $f_1$ | = | 18.8 | [Hz] |
| $f_2$ | = | 75.1 | [Hz] |
| $f_3$ | = | 168.9 | [Hz] |
| $f_4$ | = | 300.2 | [Hz] |
| $f_5$ | = | 469.1 | [Hz] |

The bending moment capacity is determined based on a plastic stress state and is computed as follows: $M_{rd} = ht^2\sigma_y/4 = 11.75 * 10^6[Nm]$. The deflection at midspan due to a line load, as mentioned in the first section of this chapter, is determined as follows: $\delta_{max} = Fw^3/(48EI) = 3.7[mm]$.

### 4.2.2. GFRP HG

GFRP is chosen since it is the most commonly used composite material. Glass fibres usually are chosen since they are a lot cheaper than the more advanced aramid and carbon fibres [18] at the cost of a lower Young's modulus and tensile strength. The low price of the glass fibres outweighs lower mechanical properties, making it a more economical building material. The glass fibres are combined with Unsaturated Polyester (UP) resin.

Two GFRP HGs are assessed. One HG has a thickness based on strength, e.g. a required bending moment capacity equal to the bending moment capacity of the steel HG as assessed in section 4.2.1. The other HG is dimensioned on stiffness, e.g. having the same bending stiffness as the steel HG which is assessed in section 4.2.1.

Input parameters concerning material properties of GFRP are primarily acquired using table 5.1 in the lecture notes written by Kolstein [18].

Table 4.3: Input parameters GFRP HG

| | | | | |
|---|---|---|---|---|
| **Width (span direction)** | w | = | 5.0 | [m] |
| **Height** | h | = | 5.0 | [m] |
| **Density** | $\rho$ | = | $2.0 * 10^3$ | $[kg/m^3]$ |
| **Tensile strength parallel to the fibres** | $\sigma^*_{11}ult$ | = | $700 * 10^6$ | [Pa] |
| **Young's modulus parallel to the fibres** | $E_{11}$ | = | $42 * 10^9$ | [Pa] |
| **Tensile strength perpendicular to the fibres** | $\sigma^*_{22}ult$ | = | $30 * 10^6$ | [Pa] |
| **Young's modulus perpendicular to the fibres** | $E_{22}$ | = | $12 * 10^9$ | [Pa] |
| **Poisson ratio** | $\nu_{12}$ | = | 0.3 | [-] |

The tensile strength and Young's modulus of steel are $235 * 10^6 N/m^2$ and $210 * 10^9$ respectively. Therefore, the strength of GFRP in direction of the fibres is a lot higher, the strength perpendicular to the fibre direction is a lot lower and the stiffness (expressed in the Young's modulus) is a lot lower for both in fibre direction and perpendicular to the fibre direction.

The density of the material is determined in the following way:

$$\rho = v_f\rho_f + (1 - v_f)\rho_r = 2.0 * 10^3[kg/m^3] \tag{4.2}$$

| | | | | | | |
|---|---|---|---|---|---|---|
| In which: | $v_f$ | = | Fibre volume fraction | = | 0.6 | [-] |
| | $\rho_f$ | = | Fibre density | = | $2.59 * 10^3$ | $[kg/m^3]$ |
| | $\rho_r$ | = | Resin density | = | $1.2 * 10^3$ | $[kg/m^3]$ |

#### HG ASSESSMENT

The HG which is dimensioned on strength has the same bending moment capacity as the steel HG, i.e. $M_{rd} = 11.8 * 10^6[Nm]$. Since GFRPs fail in a brittle manner without yielding the bending moment capacity is based on elastic deformations and is determined as: $M_{rd} = ht^2\sigma^*_{11}ult/6$, in which the only unknown is the thickness of the HG. Solving for the HG thickness a value of 14 centimetres is found. For this thickness the mass of the HG becomes 7000 kilogram. The bending stiffness is computed as before and is equal to $50 * 10^6[Nm^2]$. The maximum deflection, located at midspan, is computed as done before and becomes 52 millimetres.

When the thickness of the HG is determined based on a stiffness being equal to the one of the steel HG, another required thickness is found. In order to obtain the same bending stiffness for the GRFP HG as for the steel HG the bending stiffness should be $700 * 10^6 [Nm^2]$. Rewriting of the formula for bending stiffness results in a thickness off: $t = (12EI_{steel}/(hE_{11}))^{1/3} = 0.34[m]$. The mass of the HG becomes $17 * 10^3$ kg. The deflection due to the loading is found to be 3.7 millimetres.

The natural frequencies of the HG become:

Table 4.4: Natural frequencies found for the GFRP HG

| **Natural frequency** | | **GFRP - M** | **GFRP - EI** | **Unit** |
|---|---|---|---|---|
| $f_1$ | = | 11.8 | 28.4 | [Hz] |
| $f_2$ | = | 47.2 | 113.7 | [Hz] |
| $f_3$ | = | 106.2 | 255.8 | [Hz] |
| $f_4$ | = | 188.7 | 454.8 | [Hz] |
| $f_5$ | = | 294.9 | 710.7 | [Hz] |

In which: GFRP - M = HG dimensioned on strength.
GFRP - EI = HG dimensioned on stiffness.

### 4.2.3. CFRP HG

CFRP is the most advanced but also the most expensive composite building material. Therefore, it is checked what influence the choice of this material has on the dynamic properties of a structure. As well as for the GFRP HG two HGs are dimensioned; one having the same bending moment capacity as the steel HG and one having the same bending stiffness as the HG.

As for section 4.2.2 the input parameters concerning material properties of CFRP are primarily acquired using table 5.1 in the lecture notes written by Kolstein [18].

Table 4.5: Input parameters CFRP HG

| | | | | |
|---|---|---|---|---|
| **Width (span direction)** | w | = | 5.0 | [m] |
| **Height** | h | = | 5.0 | [m] |
| **Density** | $\rho$ | = | $1.6 * 10^3$ | $[kg/m^3]$ |
| **Tensile strength parallel to the fibres** | $\sigma^*_{11}ult$ | = | $1.5 * 10^9$ | [Pa] |
| **Young's modulus parallel to the fibres** | $E_{11}$ | = | $180 * 10^9$ | [Pa] |
| **Tensile strength perpendicular to the fibres** | $\sigma^*_{22}ult$ | = | $40 * 10^6$ | [Pa] |
| **Young's modulus perpendicular to the fibres** | $E_{22}$ | = | $10 * 10^9$ | [Pa] |
| **Poisson ratio (as mentioned in section 4.2.2)** | $\nu_{12}$ | = | 0.28 | [-] |

The tensile strength and Young's modulus of steel are $235 * 10^6 N/m^2$ and $210 * 10^9$ respectively. Therefore the strength of CFRP is higher in fibre direction, but lower perpendicular to the fibre direction. Also the stiffness (expressed in the Young's modulus) is a little lower in fibre direction but much lower perpendicular to the fibre direction.

#### HG ASSESSMENT

Properties of the HG are computed in a similar way as the GFRP HG. Therefore, the following table is used to display these properties.

Table 4.6: Properties of CFRP HG

| | | | **CFRP - M** | **CFRP - EI** | **Unit** |
|---|---|---|---|---|---|
| **Bending moment capacity** | $M_{rd}$ | = | $12 * 10^6$ | $55 * 10^6$ | [Nm] |
| **Thickness** | t | = | $9.7 * 10^{-2}$ | $2.1 * 10^{-1}$ | [m] |
| **Mass** | m | = | $3.9 * 10^3$ | $8.5 * 10^3$ | [kg] |
| **Bending stiffness** | EI | = | $68 * 10^6$ | $700 * 10^6$ | $[Nm^2]$ |
| **Maximum deflection** | $\delta$ | = | $3.8 * 10^{-2}$ | $3.7 * 10^{-3}$ | [m] |

In which: CFRP - M = HG dimensioned on strength.
CFRP - EI = HG dimensioned on stiffness.

The natural frequencies of the HG become:

Table 4.7: Natural frequencies found for the CFRP HG

| **Natural frequency** | | **CFRP - M** | **CFRP - EI** | **Unit** |
|---|---|---|---|---|
| $f_1$ | = | 18.6 | 40.4 | [Hz] |
| $f_2$ | = | 74.3 | 161.4 | [Hz] |
| $f_3$ | = | 167.2 | 363.2 | [Hz] |
| $f_4$ | = | 297.3 | 645.7 | [Hz] |
| $f_5$ | = | 464.6 | 1,008.9 | [Hz] |

In which: CFRP - M = HG dimensioned on strength.
CFRP - EI = HG dimensioned on stiffness.

### 4.2.4. COMPARISON BETWEEN THE HGS IN DRY CONDITION

This section is used to elaborate similarities of and differences between the HGs. First the HGs are assessed in dry condition after which the HGs are assessed including the influence of water. The steel HG and four composite HGs are compared based on physical properties which are shown in table 4.8.

Table 4.8: Comparison of the HGs in dry condition

| | **Steel** | **GFRP - M** | **GFRP - EI** | **CFRP - M** | **CFRP - EI** | **Unit** |
|---|---|---|---|---|---|---|
| **Thickness** | 0.20 | 0.14 | 0.34 | 0.10 | 0.21 | [m] |
| **Mass** | 39,250 | 7,097 | 17,100 | 3,970 | 8,485 | [kg] |
| **Bending moment cap.** | $11.8 * 10^6$ | $11.8 * 10^6$ | $68.2 * 10^6$ | $11.8 * 10^6$ | $55.4 * 10^6$ | [Nm] |
| **Bending stiffness** | $700 * 10^6$ | $50 * 10^6$ | $700 * 10^6$ | $68 * 10^6$ | $700 * 10^6$ | $[Nm^2]$ |
| **deflection** | 3.7 | 52.1 | 3.7 | 38.1 | 3.7 | [mm] |
| $f_1$ | 18.8 | 11.8 | 28.4 | 18.6 | 40.4 | [Hz] |

In which: GFRP - M = GFRP HG dimensioned on strength.
GFRP - EI = GFRP HG dimensioned on stiffness.
CFRP - M = CFRP HG dimensioned on strength.
CFRP - EI = CFRP HG dimensioned on stiffness.

In order to display the differences between the choice of materials and the influence of dimensioning on strength or stiffness the following figure shows the properties of the HGs as shown in table 4.8 compared to the properties of the steel HG.

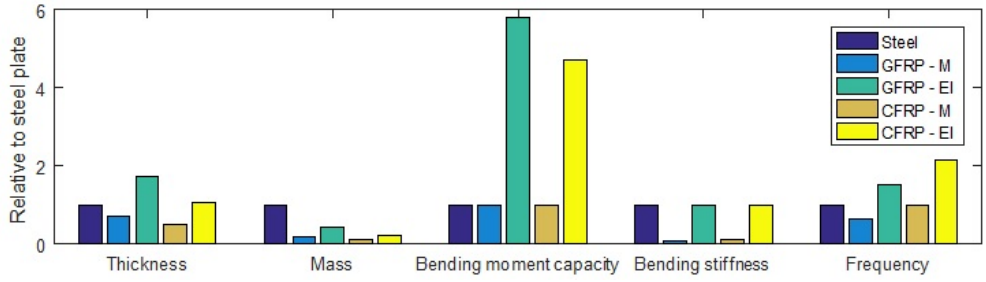


Figure 4.3: Comparison of the HGs

Figure 4.3 clearly shows relative properties of the five plates compared to the properties of the steel HG. Both composite HGs dimensioned on strength result in a lower thickness, mass, bending stiffness and frequency. The unfavourable influence of the lower bending stiffness outweighs the favourable influence of the lower mass resulting in a lower natural frequency than for the steel HG. When dimensioned on stiffness being equal to the one of the steel plate, the Glass Fibre-Reinforced Polymer and Carbon Fibre-Reinforced Polymer plate will have 5.8 and 4.7 times the bending moment capacity of the steel HG, respectively. When dimensioned on the strength being equal to the strength of the steel HG a much lower bending stiffness is found, being only seven and ten percent of the stiffness of the steel HG, respectively. Which directly results in a fourteen and ten times larger deflection, respectively. When dimensioned on strength a significantly lower natural frequency is found while for the HG which is dimensioned on stiffness a significantly higher natural frequency is found.

Since loading due to flow have low excitation frequencies having a structure with a higher natural frequency is vital in order to avoid vibrations. Based on figure 4.3 this implies that the HGs dimensioned on strength are more susceptible to undesirable vibrations than a steel HG while the HGs dimensioned on stiffness would be less susceptible.

## 4.3. COMPUTATION OF ADDED HYDRODYNAMIC MASS

As mentioned in section 3.4 the presence of water influences the dynamic properties of the vibrating structure in terms of an added water mass, added water damping and added water stiffness. This section is used to elaborate the added mass and compare certain formulas and approaches in order to find reasonable values for added terms for situations between limit cases.

### 4.3.1. ADDED MASS ACCORDING TO WESTERGAARD [5], KOLKMAN AND JONGELING [2] AND TIELEMAN [6]

The added mass is computed for a horizontally moving hydraulic gate with a width of five metres and water levels of five metres on both sides using formulas derived by Westergaard [5] and Kolkman and Jongeling [2] and the numerical scheme that is presented by Tieleman [6].

For the chosen hydraulic gate with a width of five metres and water levels on both sides of five metres according to Westergaard [5] the total added water mass becomes:

$$m_w = 2\frac{7}{12} * 1000 * 5 * 5^2 \; = \; 145,830[kg]. \tag{4.3}$$

Assuming that the flexibility of the plate does not play a role, as done in Kolkman and Jongeling [2], (using figure A3.1, figure A3.4 and formula A3.3 in part A of [2]) the added mass is computed as:

$$m_w = 2 * C_L \rho h^2 w = 2 * 0.542 * 1,000 * 5^2 * 5 = 135,500[kg] \tag{4.4}$$

Kolkman and Jongeling [2] describe the influence of a partially opened gate in which neither the case of a fully closed gate nor the case of infinite water depth is truly valid. They [2] also describe a numerical scheme based on potential flow theory in which other structures or partially opened gates may be assessed. This numerical scheme has been used by Tieleman [6] to compare the added mass as described by Kolkman and Jongeling [2] to the potential theory. Kolkman and Jongeling [2] assumes rigid body vibrations in which the gate a a whole moves as a rigid box, while in reality the horizontal movement of the hydraulic gate is caused by bending due to the water loading, since the vertical edges of the hydraulic gate are horizontally constrained by the guiding system.

This section is used to determine the influences of a partially opened gate and what the influence of a bending vibration mode is on the computed added mass. As a test case a gate with a width of five metres, a height of five metres and a thickness of one metre is used. The water levels on both sides of the horizontally vibrating gate are set to be five metres as well.

Figure 4.4 is obtained from computations performed using the numerical scheme provided by Tieleman [6] and shows an added water mass of 67,600 kg per side, being 135,200 kg in total.

The computed values using Westergaard [5] and Kolkman and Jongeling [2] and the numerical scheme presented by Tieleman [6] are shown in table 4.9.

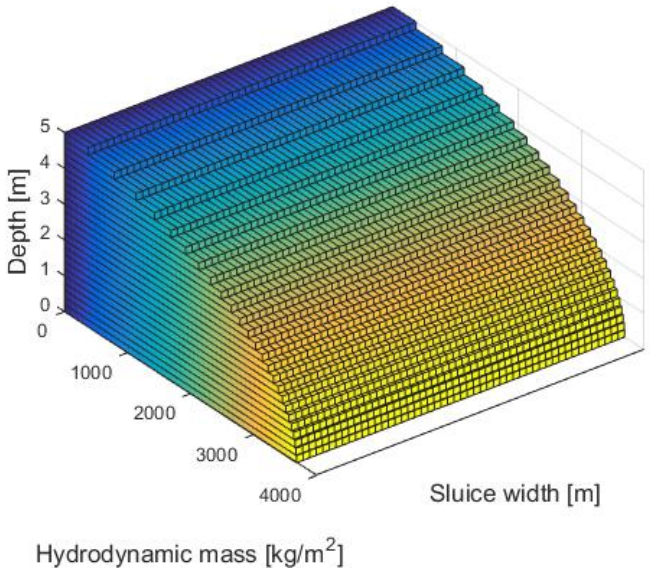


Figure 4.4: Computed added mass for rigid body movements [6]

Table 4.9: Comparison of added masses

| **According to:** | **Added water mass** | **Percentage compared to Kolkman and Jongeling [2]** |
|---|---|---|
| **Kolkman and Jongeling [2]** | 135,500 | 100.0 % |
| **Tieleman [6]** | 135,200 | 99.8 % |
| **Westergaard [5]** | 145,830 | 107.6 % |

When comparing equation 4.3 to equation 4.4, using Westergaard [5] results in a slightly larger added mass. The difference between using figure 3.8 and the potential flow theory as described in Kolkman and Jongeling [2] and elaborated by Tieleman [6] is purely a small numerical deviation due to the grid size used in the computations. The comparison between Tieleman [6] and Westergaard [5] are shown in figure 4.5

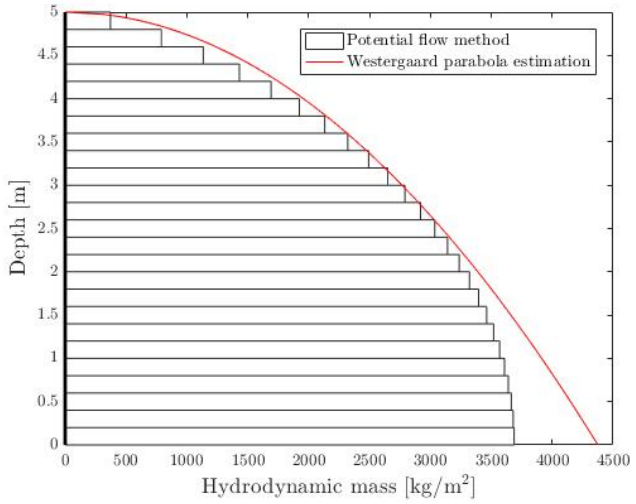


Figure 4.5: Computed added mass by Tieleman [6] compared to Westergaard [5]

Figure 4.5 shows the differences for the function of the added water mass over the water column. It is clear to see that for the top three metres of the water column results are similar while the deviations are considerable for larger water depths.

### 4.3.2. INFLUENCE OF A PARTIALLY OPENED GATE ACCORDING TOTIELEMAN [6]

In this section the influence of a partially opened gate on the added water mass is elaborated. As mentioned in section 3.4.2 for horizontally vibrating hydraulic gates, added water masses can be computed for a closed hydraulic gate and for the "ship" type of vibration. Also an average added mass is determined in both a linear and a quadratic fashion in the following manner:

$$m_{w,linear\ interpolation} = m_{w,ship} * \frac{\delta}{h} + m_{w,closedgate} * (1 - \frac{\delta}{h}) \tag{4.5}$$

and

$$m_{w,quadratic\ interpolation} = \frac{m_{w,ship} * (\frac{\delta}{h})^2 + m_{w,closedgate} * (1 - \frac{\delta}{h})^2}{(\frac{\delta}{h})^2 + (1 - \frac{\delta}{h})^2} \tag{4.6}$$

In which: $\delta$ = Opening height of the gate $[m]$

Results for the different computations are shown in figure 4.6.

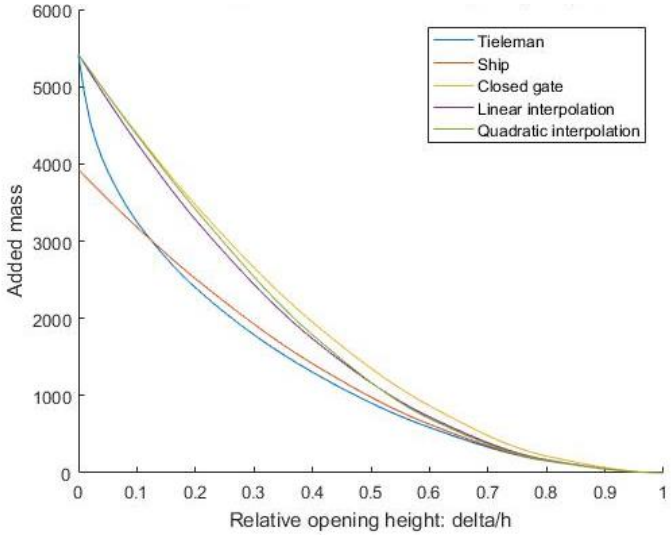


Figure 4.6: Added mass for the different computations

It is noticeable that looking at the gate as if it is closed results in an overestimation of the added mass as the added mass quickly decreases for small relative opening heights already. Figure 4.7 shows the different added masses after subtraction of results from the numerical scheme elaborated by Tieleman [6]. In order to compare the limit cases, being an almost fully opened and a fully closed hydraulic gate, the added masses are normalised by dividing the added masses by results obtained using the numerical scheme provided by Tieleman [6]. Results are shown in table 4.10.

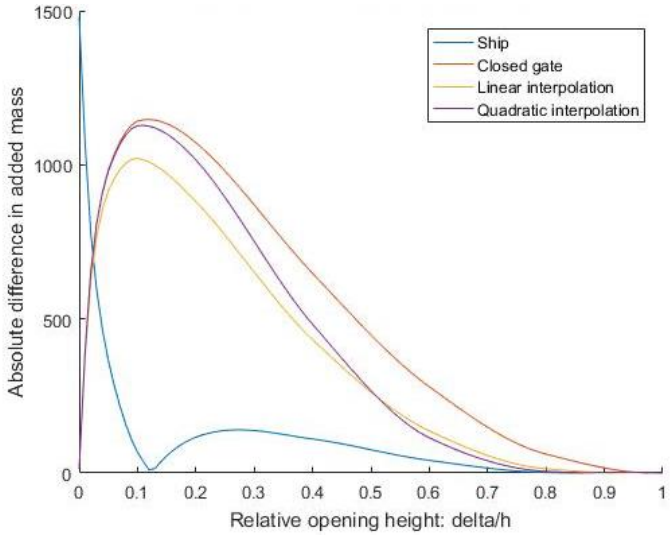


Figure 4.7: Added mass for different relative opening heights and formulas

Table 4.10: Relative added masses compared to Tieleman [6]

| $\delta/h$ [m] | Results from computations [6] divided by the added mass computed for: | | | |
|---|---|---|---|---|
| | Ship | Closed gate | Interpolated average: ship - closed gate | |
| | | | Linear | Quadratical |
| 0.0 | 138 % | 100 % | 100 % | 100 % |
| 0.8 | 99 % | 72 % | 92 % | 97 % |

First of all figure 4.7 and table 4.10 show that for a fully closed gate results are equal for the numerical scheme used by Tieleman [6] and formulas for a closed gate, using Kolkman and Jongeling [2]. The same holds for an almost fully opened hydraulic gate, with a relative opening height of 0.8 metres, in which Tieleman [6] comes up with the same answer as the ship type of added mass as found in Kolkman and Jongeling [2]. One can also conclude that the ship type of the added mass in general shows the best results for a relative opening height of around 0.03 and larger.

### 4.3.3. INFLUENCE OF A BENDING VIBRATION COMPARED TO RIGID BODY VIBRATIONS ACCORDING TO TIELEMAN [6]

First of all the added water mass of the bending hydraulic gate is compared to the added water mass for a hydraulic gate undergoing a rigid body vibration. An impression of the first vibration (beam) mode of the plate in wet condition is shown in figure 4.8. The arrows indicate the vibration direction.

It is easy to understand that the width averaged vibration amplitude, speed and acceleration for a beam undergoing a bending vibration motion are smaller than for a rigid body vibration in which the amplitude, speed and acceleration are equal over the entire structure. This has to do with the fact that close to the boundaries where the structure is supported, the amplitudes, speed an accelerations are considerably smaller than at midspan. Figure 4.9 shows the computed added mass for a bending beam.

The case of a hydraulic gate vibrating in a bending mode of the structure instead of rigid body movement in which the gate is regarded as an infinitely stiff structure, results in a much lower added mass, when compared to rigid body vibrations, of 86,087 kg which is about 64 % of the added mass which will be in the system for rigid body vibrations.

### 4.3.4. INFLUENCE OF BENDING VIBRATION AND A PARTIALLY OPENED GATE ON ADDED MASS

Table 4.11 shows the differences between added masses computed for different opening heights for both a rigid body vibration and bending mode.

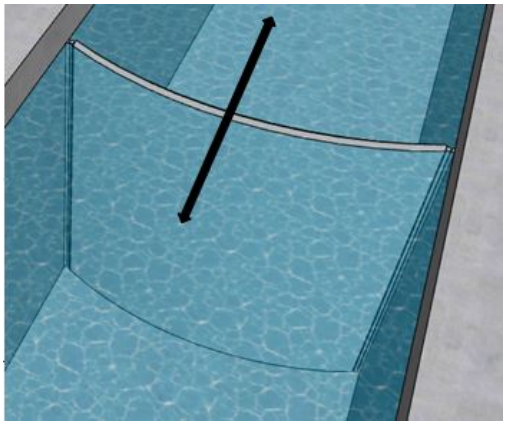

Figure 4.8: First vibration mode

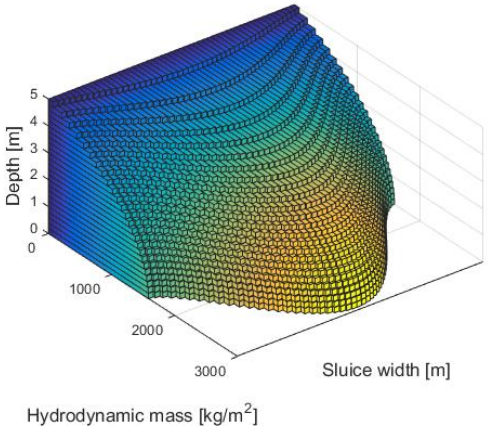


Figure 4.9: Computed added mass for a bending hydraulic gate [6]

Table 4.11: Added mass for multiple gate openings for a bending gate and rigid body movement

| $\delta$ [m] | **Sine shape** | **Rigid body** | |
|---|---|---|---|
| | **Added mass** $*10^3$ **[kg]** | **Added mass** $*10^3$ **[kg]** | **Ratio sine shape / rigid body** |
| 0.0 | 86.1 | 135.2 | 64 % |
| 0.3 | 59.8 | 93.9 | 64 % |
| 0.4 | 55.4 | 87.0 | 64 % |
| 0.5 | 51.7 | 81.2 | 64 % |
| 1.0 | 38.2 | 59.9 | 64 % |
| 2.0 | 20.7 | 32.6 | 64 % |
| 3.0 | 9.4 | 14.7 | 64 % |
| 4.0 | 2.5 | 3.9 | 64 % |

For all opening heights the sine shaped bending mode has an added mass of 64 % of the added mass occurring for a rigid body vibration. This difference is exactly the average value of a half sine with an amplitude of one: $\frac{\int_0^\pi sin(x)}{\pi} = 0.64$.

## 4.4. ANALYSIS OF A STEEL HG, GFRP HG AND A CFRP HG IN WET CONDITION

The influence of the surrounding water is already explained in section 3.4. In section 3.4.2, the added water mass has already been computed for a HG with a width of five metres and water levels on both sides of five metres, being 135,500 kilogram. The added hydrodynamic mass for rigid body vibrations is included since the effect of bending vibrations on the added mass have not been thoroughly researched in this thesis and requires additional research.

In order to check if the results from those computations are valid, it is first checked whether the assumption of negligible influence of radiating surface waves on water pressures fluctuations is valid by checking if: $\psi = \omega^2 h/g \geq 100$ [2], in which $\psi$ is a dimensionless measure of the vibration frequency. For a water depth equal to the height of the HG, being five metres, a minimum natural frequency can be found as: $f_1 = \sqrt{100 * 9,81/h)/(2\pi)} \geq 2.23[Hz]$, which holds for all natural frequencies of the HGs in dry condition. Whether this is valid for the natural frequency including the influence of the surrounding water is discussed later on in this section.

The computed added mass is enormous when compared to the masses as mentioned in table 4.8. A higher mass on its turn would reduce the natural frequency since it is a function of $\sqrt{1/mass}$. Meaning that for an increasing mass the natural frequency decreases.

As mentioned in section 3.4.1 the combined system of the structure and surrounding water is seen as a single degree of freedom system. In order for the continuously distributed mass to be modelled correctly as a concentrated mass in a single degree of freedom system, the mass of the actual system is multiplied with a factor 0.5 as mentioned in appendix A.

The large impact the influence on water has on the dynamic properties of the plate are clearly shown in the following table.

Table 4.12: Comparison of the hgS in wet condition

| | **Steel** | **GFRP - M** | **GFRP - EI** | **CFRP - M** | **CFRP - EI** | **Unit** |
|---|---|---|---|---|---|---|
| **Equivalent dry mass** | 19,625 | 3,548 | 8,550 | 1,954 | 4,242 | [kg] |
| **Mass including added mass** | 155,125 | 139,048 | 144,050 | 137,450 | 139,740 | [kg] |
| **Ratio wet / dry mass** | 7.9 | 39.2 | 16.8 | 70.4 | 32.9 | [-] |
| **New first natural frequency** | 6.7 | 1.9 | 6.9 | 2.2 | 7.0 | [Hz] |
| **Ratio wet / dry natural frequency** | 0.36 | 0.16 | 0.24 | 0.12 | 0.17 | [-] |
| $\psi$ | 896 | 71 | 965 | 99 | 995 | [-] |

In which: GFRP - M = GFRP HG dimensioned on strength.
GFRP - EI = GFRP HG dimensioned on stiffness.
CFRP - M = CFRP HG dimensioned on strength.
CFRP - EI = CFRP HG dimensioned on stiffness.

It is interesting to see that in case of the composite HGs dimensioned on strength the mass including added mass of the surrounding water is up to a factor seventy larger than the dry mass of the composite plates themselves while for the steel plate this " only " is a factor 7.9. As mentioned before, this larger mass directly decreases the natural frequency.

It also becomes clear that the HGs made out of GFRP and CFRP which are dimensioned on strength have a low natural frequency, being 1.9 and 2.2 Hertz, respectively. These frequencies are lower than required for the radiating surface waves to be neglected, being 2.23 Hertz, as calculated in subsection 4.4. Since the $\psi$-values are well over ten, the added mass does not change, as mentioned in section 3.4.2.

Figure 4.10 shows that the total mass for the five HGs when including the added water mass is nearly the same since the self-weight of the HG is small compared to the added mass. Since the added mass is the same for the five HGs and the composite HGs, especially the ones dimensioned on strength, have a lower mass than the steel HG their mass ratio with and without water is higher. This directly results in a larger decrease of their frequency than for the steel HG. Figure 4.11 shows the influence of the added water mass on the HGs in terms of natural frequencies.

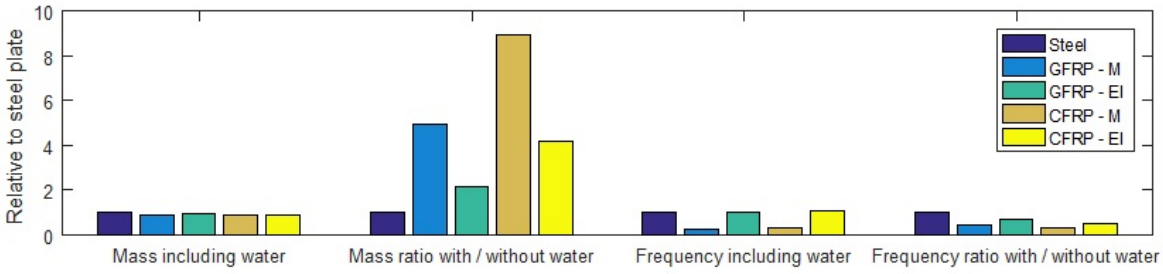


Figure 4.10: Comparison of the HGs in submerged condition

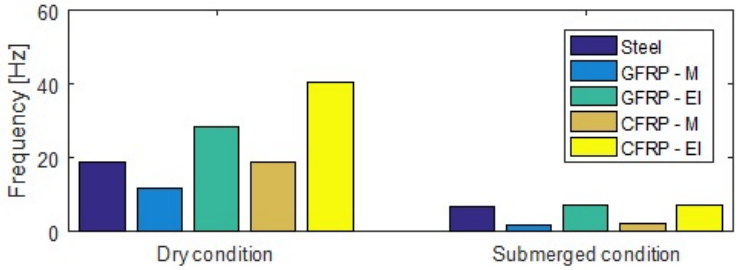


Figure 4.11: Comparison of the first natural frequency of HGs in dry and submerged condition

## 4.5. INFLUENCE OF ORTHOTROPIC MATERIAL PROPERTIES ON THE DYNAMIC BEHAVIOUR

In the previous sections the HGs are analysed as beams which means that only material properties of the structure in span direction, being the fibre direction, are used. Including weaker material properties perpendicular to the fibre direction influences the dynamic properties of the HG. Including fibres in other directions than span direction such as 45° or 90 ° would decrease the stiffness of the structure since mechanical properties such as the Young's modulus and tensile strength of the material are lower in other directions than the direction of the fibres, as seen in table 4.3 and table 4.5. Including fibres in other directions would result in a larger thickness and therefore higher mass for a certain bending stiffness to be equal to the bending stiffness of a HG with fibres only in span direction. As mentioned before in section 4.4 the natural frequency depends on one over the square root of the mass.

In order to find out what the influence of the orthotropic material is on the properties of the HG an analysis is performed using Finite Element Method (FEM) software. The largest influence of the orthotropic properties will be found for the composite material having the largest relative differences between the Young's modulus and tensile strength in direction parallel to the fibres and perpendicular to the fibres, this comparison is made in table 4.13.The plates assessed in this chapter have all fibres aligned in span direction. This directly means that the stiffness of the plates in span direction directly is larger than the stiffness of the plate in transverse direction.

Table 4.13: Comparison of orthotropic properties

| **Ratio** | **GFRP** | **CFRP** |
|---|---|---|
| **Young's modulus** | $42 * 10^9 / 12 * 10^9 = 3.5$ | $180 * 10^9 / 10 * 10^9 = 18$ |
| **Tensile strength** | $700 * 10^6 / 30 * 10^6 = 23.3$ | $1.5 * 10^9 / 40 * 10^6 = 37.5$ |

It is clear to see that for CFRP the influences of the orthotropic material are larger than for GFRP. Therefore, a CFRP plate is assessed using FEM. First of all a plate is assessed as if it is isotropic, i.e. having the same material properties in all directions. These results are compared to results from the analytical assessment of the CFRP plate. After which the orthotropic properties are implemented.

### 4.5.1. ASSESSMENT OF A CFRP PLATE USING FEM

The plate is modelled in the FEM software Ansys ©. In this section the material is assumed to be isotropic. If the plate is analysed as a beam as discussed in appendix A one finds the five beam mode shapes with their accompanying natural frequencies as shown in figures 4.12 until 4.16. Since the transverse stiffness is not infinitely large also mode shapes in transverse direction will occur. In this case the first five beam mode shapes are accompanied by the first, fourth, ninth, fourteenth and twenty-fifth natural frequency.

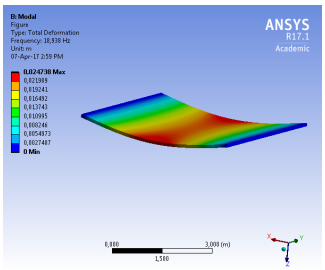


Figure 4.12: First mode shape - isotropic

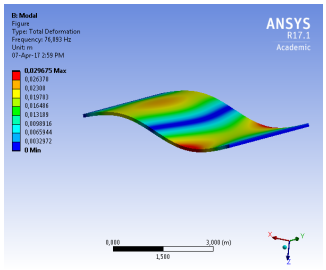


Figure 4.13: Fourth mode shape - isotropic

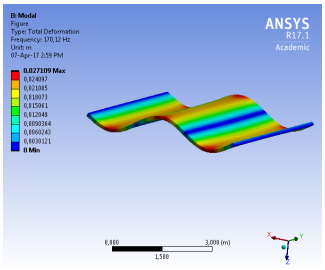


Figure 4.14: Ninth mode shape - isotropic

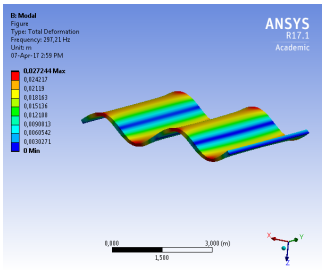


Figure 4.15: Fourteenth mode shape - isotropicy

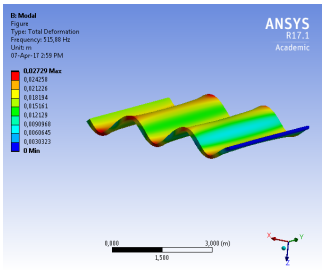


Figure 4.16: Twenty-fifth mode shape - isotropic

The frequencies which are accompanying these five mode shapes are compared to analytical results and shown in table 4.14.

Table 4.14: Comparison of Ansys and analytical results

| **Analytical** | | **Ansys** | | |
|---|---|---|---|---|
| **Mode shape nr.** | **Frequency** | **Mode shape nr.** | **Frequency** | **Relative frequency** |
| **1** | 18.6 | 1 | 18.9 | 102 % |
| **2** | 74.3 | 4 | 76.1 | 102 % |
| **3** | 167.2 | 9 | 170.1 | 102 % |
| **4** | 297.3 | 14 | 297.2 | 100 % |
| **5** | 464.6 | 25 | 515.9 | 111 % |

Until the fourth beam mode results are similar. The fifth beam mode shows a significantly higher frequency for the results obtained from Ansys than the analytical results. The plate has a length over thickness ratio of: $5/0.097 = 52$. As mentioned in equation A.5 in appendix A this would mean that shear deformation should be negligible for the first ten natural frequencies. Since flow-induced vibrations typically have low frequencies usually people are only interested in the first natural frequency of the structure.

Mode shapes of the plate other than those also occurring at a beam are shown in figures 4.17 until 4.23.

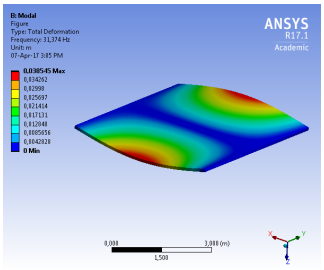


Figure 4.17: Second mode shape - isotropic

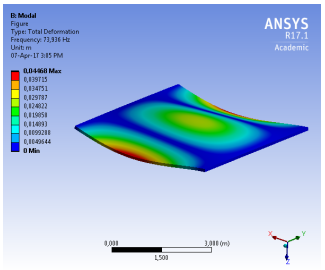


Figure 4.18: Third mode shape - isotropic

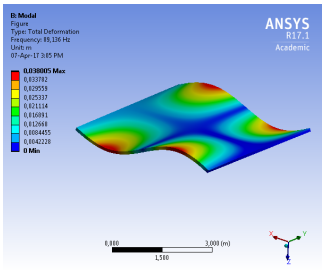


Figure 4.19: Fifth mode shape - isotropic

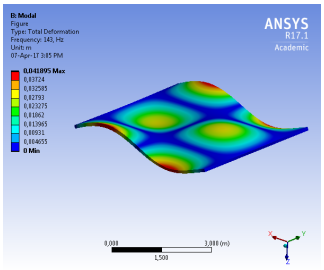


Figure 4.20: Sixth mode shape - isotropic

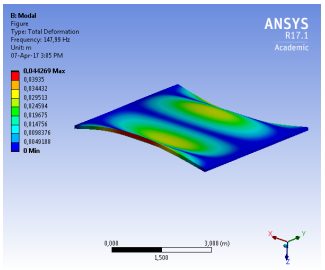


Figure 4.21: Seventh mode shape - isotropic

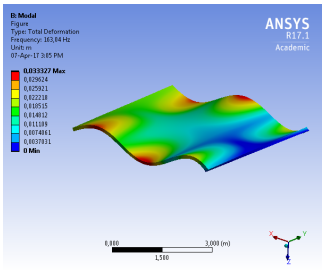


Figure 4.22: Eighth mode shape - isotropic

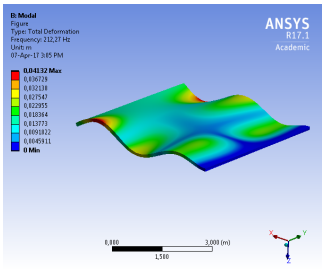


Figure 4.23: Tenth mode shape - isotropic

### 4.5.2. ASSESSMENT OF THE INFLUENCE OF ORTHOTROPIC MATERIAL PROPERTIES OF A CFRP PLATE USING FEM

The first five beam mode shapes are now to be found as the first, seventh, fifteenth, twenty-eighth and forty-first, while the fifth mode shape first was found to be the twenty-fifth mode shape of the plate. This has to do with the lower stiffness in transverse direction, significantly lowering natural frequencies for transverse mode shapes. Table 4.15 shows the influence of the material being orthotropic rather than isotropic in terms of mode numbers of the first five beam mode shapes and their accompanying frequencies.

Table 4.15: Comparison of Ansys results for isotropic and orthotropic material

| **Isotropic** | | **Orthotropic** | | |
|---|---|---|---|---|
| **Mode shape nr.** | **Frequency** | **Mode shape nr.** | **Frequency** | **Relative frequency** |
| 1 | 18.9 | 1 | 18.5 | 98 % |
| 4 | 76.1 | 7 | 72.6 | 95 % |
| 9 | 170.1 | 15 | 158.4 | 93 % |
| 14 | 297.2 | 28 | 268.5 | 90 % |
| 25 | 515.9 | 41 | 374.3 | 73 % |

The most important conclusion one can draw from table 4.15 is that the first beam mode remains the first vibration mode of the plate which validates the beam approach. The first mode shape in transverse direction is shown in figure 4.17 and has an accompanying frequency of 31.4 Hertz in case of isotropic material properties and a frequency of 20.0 Hertz when taking orthotropic material properties into account. For the second vibration mode in transverse direction the plates have an accompanying frequency of 73.9 Hertz and 28.6 Hertz respectively. This shows that mode shapes in transverse direction occur at lower frequencies when taking orthotropic properties into account.

### 4.5.3. INTERNAL FORCES RELATED TO STRAINS FOR THE CFRP PLATE

For the CFRP plate as assessed in section 4.2.3 with a thickness of 9.7 centimetres and all fibres in the same direction the following matrices are obtained:

$$\begin{bmatrix} N_{xx} \\ N_{yy} \\ V_{xy} \end{bmatrix} = \begin{bmatrix} 17.460 * 10^9 & 15 * 10^6 & 0 \\ 15 * 10^6 & 970 * 10^6 & 0 \\ 0 & 0 & 0.679 * 10^9 \end{bmatrix} \begin{bmatrix} \epsilon_{xx} \\ \epsilon_{yy} \\ \gamma_{xy} \end{bmatrix} \tag{4.7}$$

$$\begin{bmatrix} M_{xx} \\ M_{yy} \\ M_{xy} \end{bmatrix} = \begin{bmatrix} 13.690 * 10^6 & 12 * 10^3 & 0 \\ 12 * 10^3 & 761 * 10^3 & 0 \\ 0 & 0 & 0.532 * 10^6 \end{bmatrix} \begin{bmatrix} \kappa_{xx} \\ \kappa_{yy} \\ \kappa_{xy} \end{bmatrix} \tag{4.8}$$

If the first elements of the first column of both the A-matrix in equation 4.7 as well as the the D-matrix in equation 4.8 are multiplied with the width of the plate, being five metres, one obtains: $8.7 * 10^{10}$ Newton and $6.8 * 10^7$ Newton metre squared which are equal to axial stiffness and bending stiffness in longitudinal direction respectively. In which the axial stiffness is computed as: $EA = E_{11}\,th = 1.8 * 10^{11} * 0.097 * 5.0$. Since the Young's modulus perpendicular to the fibre direction, being $E_{22}$, is eighteen times smaller than the Young's modulus parallel to the fibre direction, being $E_{11}$, one can also observe that for both matrices in equations 4.7 and 4.8 the second element of the second column is eighteen times smaller than the first element of the first column.

### 4.5.4. INFLUENCE OF LAMINATES IN DIFFERENT DIRECTIONS

In case the plate would consist of eight layers of equal thickness with fibres aligned in the following manner: $[45°/90°/135°/0°]_s$ in which subscript s denotes that the layers are symmetric over the neutral axis. So the outer layers have fibres parallel to span direction, being x. This layering of fibres in different directions can be seen as quasi-isotropic [18].

$$\begin{bmatrix} N_{xx} \\ N_{yy} \\ V_{xy} \end{bmatrix} = \begin{bmatrix} 7.2546 * 10^9 & 1.9756 * 10^9 & 0 \\ 1.9756 * 10^9 & 7.2546 * 10^9 & 0 \\ 0 & 0 & 2.6395 * 10^9 \end{bmatrix} \begin{bmatrix} \epsilon_{xx} \\ \epsilon_{yy} \\ \gamma_{xy} \end{bmatrix} \tag{4.9}$$

$$\begin{bmatrix} M_{xx} \\ M_{yy} \\ M_{xy} \end{bmatrix} = \begin{bmatrix} 9.2951 * 10^6 & 0.9726 * 10^6 & -0.9091 * 10^6 \\ 0.9726 * 10^6 & 3.2343 * 10^6 & -0.9091 * 10^6 \\ -0.9091 * 10^6 & -0.9091 * 10^6 & 1.4931 * 10^6 \end{bmatrix} \begin{bmatrix} \kappa_{xx} \\ \kappa_{yy} \\ \kappa_{xy} \end{bmatrix} \tag{4.10}$$

Unlike the matrix in equation 4.7 the first element of the first column is equal to the second element of the second column which has to do with the fibre alignment. This does not hold for the matrix related to the bending moments and torsion, being the matrix in equation 4.10, since the fibres in the outer layer are aligned in longitudinal direction while the internal leverage arm of the fibres aligned in transverse direction is smaller, being the second layer from the neutral axis instead of the fourth. The bending stiffness in longitudinal direction is around a factor 2.9 higher than for the transverse direction ($9.2951 * 10^6 / 3.2343 * 10^6 = 2.9$). The terms which couple the bending moments to the twisting deformation and torsional moment to the curvatures are negative, meaning that a positive curvature results in a negative torsional moment and a positive twisting deformation results in negative bending moments in the laminate.

When the elements of these two matrices are divided by the same elements in the stiffness matrices in equation 4.7 and 4.8 the following relative stiffness matrices are found:

$$\begin{bmatrix} 0.42 & 131 & - \\ 131 & 7.48 & - \\ - & - & 3.89 \end{bmatrix} \tag{4.11}$$

$$\begin{bmatrix} 0.68 & 82.21 & -\infty \\ 82.21 & 4.25 & -\infty \\ -\infty & -\infty & 2.80 \end{bmatrix} \tag{4.12}$$

Since not all the fibres are aligned in longitudinal direction both bending stiffness and axial stiffness decrease significantly, as can be found in the first element of the first column in both matrices. All other parameters are significantly improved for the laminate built up of layers with different fibre directions. For a laminate with layers in only one direction there has been no coupling between curvatures and bending moments and torsional moments, while there is a coupling for the layered material with fibres in different directions.

## 4.6. CONCLUSIONS

Based on the performed analysis the following conclusions can be drawn:

- When based on deflection requirements composite HGs show higher natural frequencies in comparison to a steel HG (solid plate). The bending moment capacity of these HGs may approximately be a factor six larger than for a steel HG with equivalent bending stiffness.
- When based on strength requirements composite HGs show lower natural frequencies than a steel HG with similar bending moment capacity. Deformations are found to be up to fourteen times larger than for a steel HG due a significantly lower (up to 14 times) bending stiffness.
- The Young's modulus of FRP is lower than the Young's modulus of steel whilst the ultimate limit strength is higher than that of steel. Therefore, an FRP structure dimensioned on deflection requirements will have a higher bending strength than an FRP structure dimensioned on bending strength requirements. Including a deflection requirement results in
- The influence of added water mass results in a larger decrease of the natural frequencies for the composite HG when compared to a steel HG due to their higher added water mass over dry mass ratio.
- It is possible to construct a plate made out of CFRP which when compared to a steel plate has the same bending stiffness, approximately the same thickness and higher natural frequencies, also including the influence of the surrounding water. This would imply that it would be less susceptible to flow-induced vibrations than a steel structure since flow-induced vibrations usually have low excitation frequencies. But since dimensioning a hydraulic gate on strength requirements rather than deflection requirements results in a thinner and therefore cheaper structure, a CFRP structure will most likely not have this benefit.
- Beam mode shapes in longitudinal direction have significantly lower natural frequencies for higher mode shapes due to the lower stiffness in transverse direction.
- Frequencies found by using FEM software including orthotropic material properties are lower than those found using analytical formulas for natural frequencies of a beam.
- Due to orthotropic properties of the composite materials mode shapes in transverse direction will have significantly lower frequencies, making them more susceptible to flow-induced vibrations.
- Including layers of fibres in directions other than in longitudinal direction results in a thicker plate with a larger mass and therefore a lower natural frequency.
- Using a layered structure with fibres aligned in different directions, such as $[45°/90°/135°/0°]_s$ results in a lower axial stiffness and bending stiffness in longitudinal direction while improving the stiffness in other directions.
- In this chapter simple solid plates are assessed. The use of other composite construction elements such as honey combs and box girders can improve the effectiveness of the material by increasing the distance between the material and the neutral axis. This results in stiffer and stronger structures while using less material and therefore may lead to structures with higher natural frequencies and a decreased susceptibility of flow-induced vibrations when compared to a simple composite HG while increasing the thickness of the HG.

It is expected that these conclusions will also hold as long as the FRP structure is similar to a steel HG in terms of construction elements, e.g. plate structures other than a solid plate. The influence of a larger thickness for GFRP HGs, as it is applied the most, and the influence of the different design / geometry of a steel and GFRP HG will be further addressed in chapter 5.

# 5

# RESEARCH ANALYSIS

Distinct differences between a steel HG and an FRP HG are found in chapter 4. The most important ones regarding the possible difference between the susceptibility to "galloping-type" vibrations can be sought for in the following properties:

- The thickness of an FRP HG is most likely larger than the thickness of a steel HG. A difference in thickness greatly influences the hydrodynamic forces acting on the gate underside;
- An FRP HG generally has a different design (laminates or sandwich panel) than a classic steel HG (plate with stiffeners).

The goal of this research is to assess the influence of the use of FRP as a construction material for hydraulic gates with a vertical degree of freedom on the susceptibility to undesired galloping-type vibrations. The analysis of vertical vibrations of FRP HGs is recommended by Gómez [26] as mentioned in section 2.5.

The approach that is used to answer the research question is addressed in section 5.1. Designs used to identify the influence of the different properties of an FRP HG and a steel HG are elaborated in section 5.2. The CFD model that is used in this research is elaborated in section 5.3. The influence of the (flowing) water surrounding the HG in terms of a hydrodynamic water mass, stiffness and damping is addressed in section 5.4. The further processing of results of CFD is elaborated in section 5.5. Conclusions drawn based in this approach are mentioned in section 5.6.

## 5.1. APPROACH

Vertical hydraulic gate vibrations can be simulated as a one degree of freedom system in which the HG with a certain mass is supported by a suspension with a certain stiffness and a damper with a certain damping coefficient. An overview of the dynamic system is shown in figure 5.1.

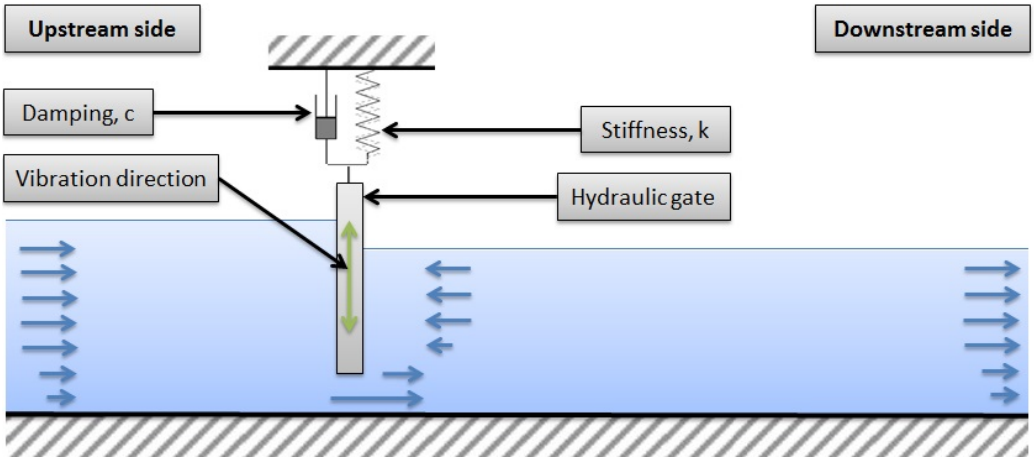


Figure 5.1: Schematic overview of the dynamic system at hand

The force acting on this system is the upward force felt on the bottom of the hydraulic gate. This upward force depends on the upstream and downstream water levels, gap height, flow velocity in the gap and the thickness of the gate. For a certain thickness of the gate and steady water levels the force acting on the system becomes dependent of the position of the gate and it's velocity. The one degree of freedom system of the hydraulic gate therefore becomes:

$$m\frac{d^2y}{dt^2} + c\frac{dy}{dt} + ky = F(y, \frac{dy}{dt}) \tag{5.1}$$

A solution to the equation for an undamped, i.e. c equals zero, of motion can be sought in the form: $y = A(t) * sin(\omega * t + \phi(t))$, with A(t) and $\phi(t)$ being slowly varying coefficients in time. The Krylov-Bogoliubov method of averaging, abbreviated as KB method, is used to determine the variation of these coefficients. The method is valid for slowly varying coefficients. More on this topic in section 5.5.

As mentioned in section 3.5.2 galloping can be modelled using the quasi-static approach in which the movement of a hydraulic gate is mimicked by placing the hydraulic gate under an angle (see figure 3.13) in order to have the same relative flow direction as for a hydraulic gate with a certain velocity. At the time when this research was performed it was not yet possible to use CFD-software to determine $C_L$-curves as a function of the gap ratio or inclination angle. Today CFD-software is capable to replace the static model tests in order to determine the $C_L$-curves. The force, being $F(y, \frac{dy}{dt})$, is a matrix whose elements are determined using CFD-software based on different combinations of possible gap heights and accompanying vertical velocity of the hydraulic gate.

CFD-software is able to take a moving structure into account at much larger computational costs than for the quasi-static approach. Also the model for the quasi-static approach is more stable and convergence is achieved much quicker than for a CFD model with a moving structure and accompanying deformable mesh. Therefore the quasi-static approach is deemed to be as close to reality as possible taking the feasibility of completion within the available time into account, as long as the quasi-static approach as described in section 3.3 remains applicable.

Included in the force matrix (right hand side of equation 5.1) are the vertical stiffness of a floating body, stiffness due to flow and damping due to flow perpendicular to the vibration direction. The added mass and sudden stiffness depends on the gap height.

The quasi-static approach has the following limitations:

- No friction due to roughness of the walls is taken into account, except for applying no-slip conditions on certain boundaries which mean that the flow velocity at these interfaces are zero;
- By placing the hydraulic gate under an angle the gap decreases. For a structure in unconfined flow this issue is not present;
- The flow velocity of the water upstream from the hydraulic gate is not equal to the flow velocity downstream from the hydraulic gate, which is the case for a structure in unconfined flow

## 5.2. DESIGNS OF THE HGS THAT ARE ASSESSED IN CHAPTER 6

The influence of the thickness of a HG on the susceptibility to galloping-type vibrations is assessed using the geometry of the HGs mentioned in section 5.2.1. A design of both an FRP HG and a steel HG is made in section 5.2.2. These designs will be used in chapter 6.

### 5.2.1. USED GEOMETRY OF THE TWO HGS USED TO ASSESS THE INFLUENCE OF A DIFFERENT THICKNESS

A water level up to 1.1 metre is modelled in CFD and an extra height of the HG of twenty centimetres is chosen, the total height of the HG becomes 1.3 metre. The thin HG and thick HG have a thicknesses of five centimetres and ten centimetres respectively to check the influence of the a thicker HG on the susceptibility to galloping-type vibrations. Results for the HG with a thickness of ten centimetres will be used in section 6.2 in the design of an FRP HG. Figure 5.2 shows the geometry of the two HGs that are assessed in section 6.1.


Figure 5.2: Geometry of the two HGs

### 5.2.2. DESIGN OF THE TWO HGS USED TO ASSESS THE INFLUENCE OF A DIFFERENT DESIGN

In order to check the influence of a different design on the susceptibility to galloping-type vibrations an FRP HG design and a steel HG design are assessed. An FRP laminate design is made after which a steel plate with stiffeners is designed having the same bending stiffness as the FRP laminate.

#### FRP HG

As GFRP is the most commonly used FRP material, as mentioned in section 2.3, this section also uses that material. Used material properties of GFRP can be found in table 4.3 in section 4.2.2. As mentioned in section 4.5.4 the fibre directions are chosen as $[45°/90°/135°/0°]_s$. Figure 5.3 shown an image of a cross section and the distribution of fibre directions over the thickness of the HG.

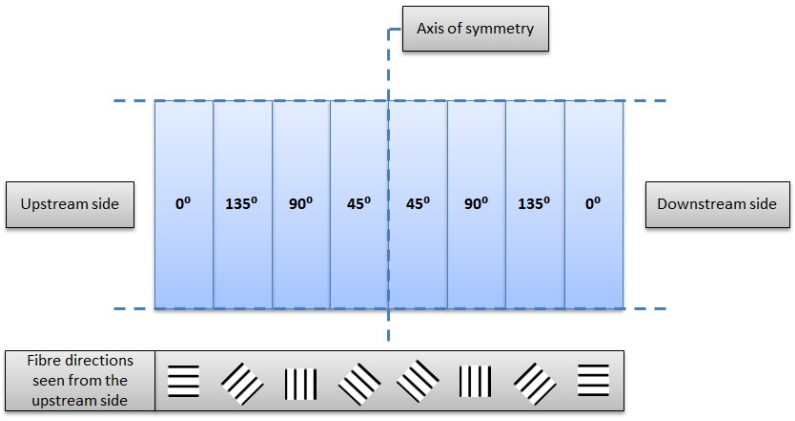


Figure 5.3: Cross section and fibre directions of the GFRP HG

The stiffness matrix resulting from this design for this is shown in matrix 5.2. The theory behind this matrix is elaborated in section 2.4.2

$$\begin{bmatrix} M_{xx} \\ M_{yy} \\ M_{xy} \end{bmatrix} = \begin{bmatrix} 2.6332 * 10^6 & 0.2946 * 10^6 & -0.1762 * 10^6 \\ 0.2946 * 10^6 & 1.4589 * 10^6 & -0.1762 * 10^6 \\ -0.1762 * 10^6 & -0.1762 * 10^6 & 0.6253 * 10^6 \end{bmatrix} \begin{bmatrix} \kappa_{xx} \\ \kappa_{yy} \\ \kappa_{xy} \end{bmatrix} \tag{5.2}$$

In which the bending stiffness is determined by multiplying the first element of the first column, being $2.6332 * 10^6$ Newton metre, with the height of the HG, being 1.3 metres, one obtains the bending stiffness in flow-direction of $3.4232 * 10^6$ Newton metre squared.

As mentioned in equation 4.2 the density of GFRP is 2,000 kilogram per cubic metre. The mass of the GFRP HG per of metre width is then computed as:

$$mass per meter width = height * thickness * density = 1.3 * 0.1 * 2,000 = 260 kg \tag{5.3}$$

The stiffness is chosen to be 26.000 Newton per metre since a suspension elongation of ten centimetres is deemed acceptable. This elongation can be computed as:

$$\Delta L = \frac{mg}{k} = \frac{260 * 9.81}{26.000} = 9.81 * 10^{-2} [m] \tag{5.4}$$

| | | | | |
|---|---|---|---|---|
| In which: | $\Delta L$ | = | Elongation of the suspension | [m] |
| | m | = | Mass of the HG | [kg] |
| | g | = | Gravitational acceleration | $[m/s^2]$ |
| | k | = | Stiffness of the suspension | [N/m] |

Since the influence of the thickness is to be researched the thin HG will have the same mass and suspension stiffness as the FRP HG.

### STEEL HG

A design of a steel HG is made, having the same bending stiffness as the FRP HG designed in section 5.2.2. The steel HG consists of a steel plate and three identical stiffeners which consist of a horizontal plate and a vertical plate. The designs of both HGs are shown in figure 5.4.

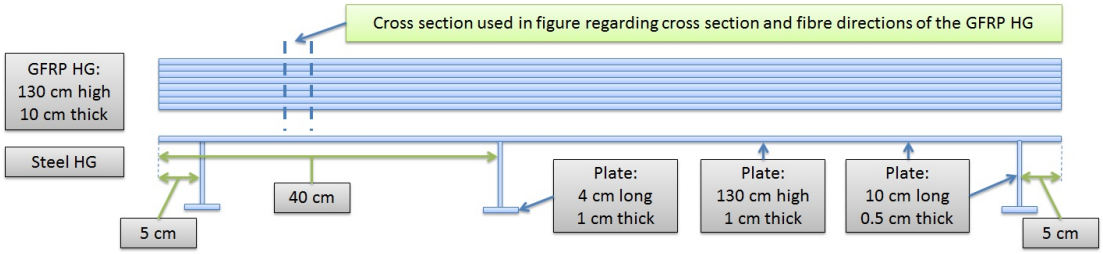


Figure 5.4: Designs of the GFRP HG and steel HG

The mass of the steel HG is computed by multiplying the cross-sectional area by the density of steel. Therefore, the mass becomes 123.2 kg. The same ratio between the stiffness and mass as used in section 6.1 is applied, i.e. the chosen stiffness of the suspension is 12,300 N/m. The cross-sectional area is computed as:

$$cross-sectional\ area = A_{vertical\ plate} + n_{stiffeners} * (A_{horizontal\ part\ stiffener} + A_{vertical\ part\ stiffener}) \tag{5.5}$$

$$cross-sectional\ area = 1.3 * 0.01 + 3 * (0.1 * 0.005 + 0.04 * 0.01) = 0.0157\ [m^2] \tag{5.6}$$

Then the accompanying mass per metre width of the steel HG becomes:

$$mass per meter width = cross-sectional area * density = 0.0157 * 7,850 = 123.2 kg \tag{5.7}$$

## 5.3. CFD MODEL

This section elaborates the CFD model used in this research. The set-up of the model is presented in section 5.3.1. The CFD model is partially validated in 5.3.2. Preliminary results regarding the influence of the thickness on the lift-coefficients acting on the HG are shown in section 5.3.3 after which the final CFD model that is used in chapter 6 is discussed in section 5.3.4.

### 5.3.1. MODEL SET-UP

Since the quasi-static approach is used a moving gate in the CFD model is not required. Also when a moving gate is modelled the discharge varies over time. At Deltares one of the ways to see if a CFD simulation is converged is to look at the discharge entering and leaving the domain; when the discharge has reached a constant value the simulation is converged and a steady state solution is achieved. Including a moving HG would mean that the discharge does not only vary in time due to the converging computations but also due to the movement of the gate. Therefore, it is easier to determine if a simulation is converged when a moving gate is not included. A two-dimensional model is used to limit the computational time that is required for the simulations. Therefore, the situation is deemed to be a two-dimensional problem in which three-dimensional effects are not taken into account. A small deviation in the downstream water level has a large impact in the computation of Cl. Therefore, the water surface elevation should be modelled as precise as possible. This is done using the Volume Of Fluid method that takes into account both water and air.

#### GEOMETRY OF THE MODEL AND BOUNDARY CONDITIONS

The HG is modelled as a rectangular plate with a thickness of five centimetres with a height being high enough to retain the water at the upstream side of the HG. Downstream and upstream boundary conditions (inlet and outlet) are positioned far away from the gate in order to prevent the possible influence of these boundary conditions on forces acting on the bottom of the gate [7]. The following boundary conditions are chosen:

- Based on experience with CFD at Deltares the upstream boundary condition is modelled as a pressure inlet. The inlet is placed eight metres upstream of the hydraulic gate. This is approximately eight times the water depth;
- As a downstream boundary condition a pressure outlet is chosen and is placed fourteen metres downstream of the hydraulic gate. This is approximately equal to fourteen times the water depth;
- The bottom boundary, being the floor is modelled as a wall without slip, meaning that the velocity next to the wall is equal to zero;
- The hydraulic gate itself is also modelled as a wall without slip.

The geometry including boundary conditions is shown in figure 5.5.

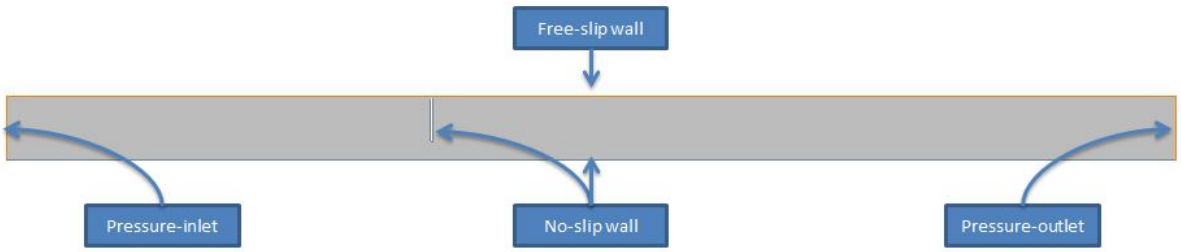


Figure 5.5: Geometry and boundary conditions for the model set-up

### 5.3.2. VALIDATION OF THE MODEL

Validation of the model is performed in two different ways. First of all results from the CFD computations are compared to experimental results performed by Thang and Naudascher [3] in a qualitative manner. This is done by comparing descriptions of three distinct gap ratio ranges, being: small gap ratios, intermediate gap ratios and large gap ratios. This qualitative comparison is performed in section D.1.1 in appendix D. After the qualitative comparison of results the curves of the lift coefficient as a function of the gap ratio and incidence angle is compared in a quantitative manner. This includes important aspects regarding the lift coefficient and its (even more important) derivatives. More on this top can be found in section 5.3.2 of appendix D.

#### HYDRAULIC CONDITIONS

Since almost no hydraulic conditions are given by Thang and Naudascher [3], these are derived from the given Reynolds number. It is noted that the graphs regarding the lift coefficient, which will be further addressed in

section 5.3.2, are composed for experiments in which the Reynolds number was equal to $2.3 * 10^4$ and is determined using:

$$Re = \frac{Vd}{\nu} \tag{5.8}$$

| In which: | | | | |
|---|---|---|---|---|
| | $Re$ | = | Reynolds number | $[-]$ |
| | $V$ | = | Velocity in the Vena Contracta | $[m/s]$ |
| | $d$ | = | Thickness of the hydraulic gate | $[m]$ |
| | $\nu$ | = | Kinematic viscosity | $[m^2/s]$ |

Since the Reynolds number is $2.3 * 10^4$, the thickness of the gate is equal to five centimetres and the kinematic viscosity of water is set as $10^{-6} m^2/s$, for water of $20°C$, the velocity in the Vena Contracta is computed to be:

$$V = \frac{Re\nu}{d} = \frac{2.3 * 10^4 * 10 * 10^{-6}}{0.05} = 0.46[m/s] \tag{5.9}$$

Using Torricelli's law one finds:

$$V = \sqrt{2 * g * \Delta h} \tag{5.10}$$

In which: $\Delta h$ = Hydraulic head $[m]$

Rewriting this expression in order to compute the hydraulic head results in:

$$\Delta h = \frac{V^2}{2g} = \frac{0.46^2}{2 * 9.81} = 0.011[m] \tag{5.11}$$

Which means that the hydraulic head for which the mentioned Reynolds number of $2.3 * 10^4$ [3] is present is only eleven millimetres.

As mentioned in Thang and Naudascher [3] the water levels are chosen high enough in order to avoid a strong influence of disturbances of the free water surface on the pressures underneath the hydraulic gate. It is mentioned that the water level was positioned about fourteen times the thickness of the gate away from the gate bottom in vertical direction.

For the largest gap, being thirty five centimetres, the water level is still chosen to be far away enough from the gap. Adding fourteen times the thickness, being seventy centimetres, to thirty five centimetres results in a water level of at least one metre and five centimetres which is rounded up to an upstream water level for the CFD computations of one metre and ten centimetres and a downstream water level of one metre and eighty nine millimetres.

Figure 5.6 shows an example of the overview of the flow velocity field of the whole domain for a gap of thirty-five centimetres.


Figure 5.6: Overview of the velocity field for a gap of thirty-five centimetres

### DESCRIPTION OF THE THREE GAP RATIO-RANGES

Thang and Naudascher [3] describe three gap-ratio ranges with each range having its specific properties. The main conclusion regarding the described gap-ratio ranges is that all qualitatively described properties in Thang and Naudascher [3] agree with computations using CFD performed in this research. Properties regarding the lift-coefficient are elaborated in section 5.3.2.

### $C_L$-CURVES

The $C_L$-coefficient is a measure of relative upward force acting on the HG's underside. The formula for determining the $C_L$-coefficient is already introduced in chapter 3 and shown in equation 5.12.

$$C_L = \frac{1}{d}\int_{x=0}^{d} \frac{h_i - h_2}{h_1 - h_2}\,dx \tag{5.12}$$

| In which: | | | | |
|---|---|---|---|---|
| | $C_L$ | = | Mean lift coefficient over the underside of the HG | $[-]$ |
| | $d$ | = | Thickness of the HG | $[m]$ |
| | $h_i$ | = | Local piezometric head at the HG's underside | $[m]$ |
| | $h_1$ | = | Upstream water level | $[m]$ |
| | $h_2$ | = | downstream water level | $[m]$ |

Results found using CFD computations for the $C_L$-curve as a function of the gap ratio are shown in figure 5.7. Thang and Naudascher [3] have described the following properties for the three different gap-ratio ranges:

- For small gap ratios the lift coefficient decreases (for increasing gap-ratio) up to a certain negative peak value;
- For intermediate gap-ratios the lift coefficient increases to a value close to zero;
- For large gap-ratios the lift coefficient becomes constant having a value close to zero.

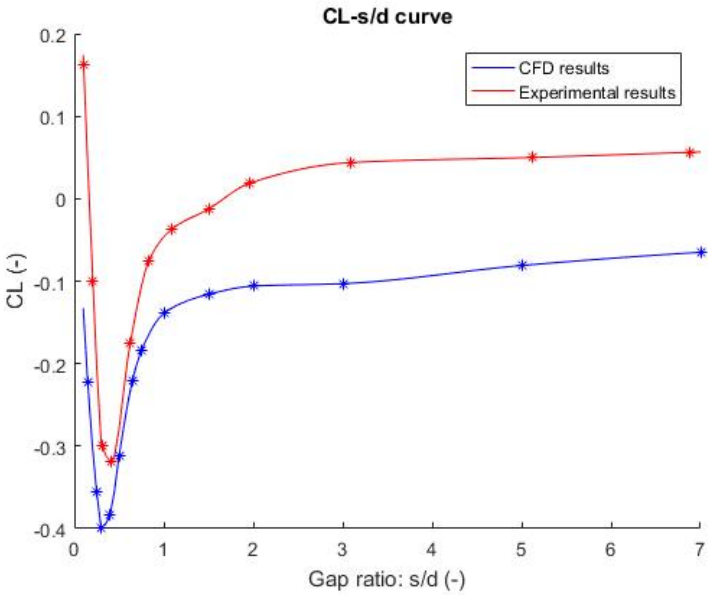


Figure 5.7: Lift coefficient, $C_L$, for different gap-ratios

Complying with Thang and Naudascher [3] for small gap ratios the lift coefficient indeed decreases up to a certain negative peak value. After which for increasing gap ratios the lift coefficient increases. Figure 5.7 also shows that the lift coefficient becomes nearly constant and close to zero for large gap-ratios. All of these results comply with results found by Thang and Naudascher [3].

The shape of the lift coefficient curve computed using CFD is similar to the one in Thang and Naudascher [3] although the average value of the lift coefficient is computed to be around 0.12 lower than resulting from experiments conducted by Thang and Naudascher [3]. More on this in section D.2. As mentioned in section 3.4 the definition of stiffness is the following:

$$k = \frac{\partial F_y}{\partial y} \tag{5.13}$$

| | | | | |
|---|---|---|---|---|
| In which: | $k$ | = | Stiffness | $[\frac{N}{m}]$ |
| | $F_y$ | = | Force in y-direction | [N] |
| | $y$ | = | Position | [m] |

Therefore, the spatial derivative of the $C_L - s/d$-curve, is a measure of the change in upward force over a length which translates to a measure of hydrodynamic stiffness. The most important comparison regarding figure 5.7 is that the spatial derivative of the $C_L - s/d$-curves, whose sign translates to the occurrence of positive or negative hydrodynamic stiffness, appear to be similar. Figure 5.8 shows a plot of the derivatives of both CFD computations and results of experiments performed by Thang and Naudascher [3] as presented in figure 5.7.

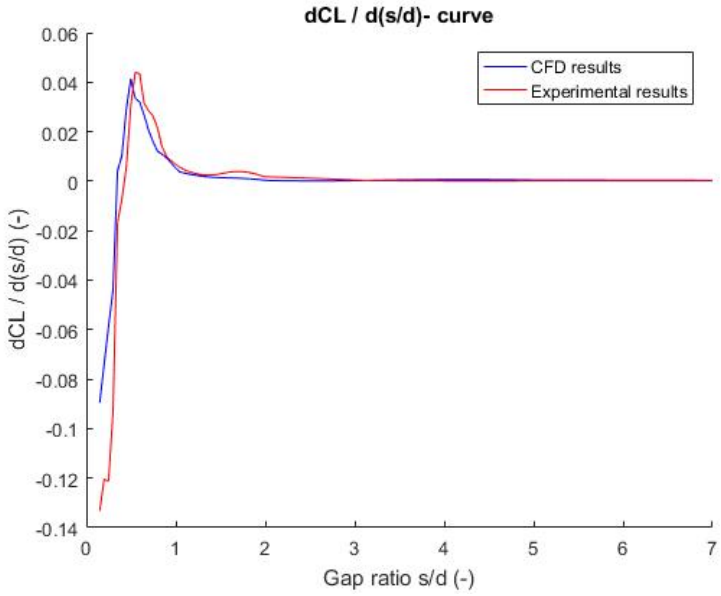


Figure 5.8: The spatial derivative of the lift coefficient for different gap-ratios

The figure 5.8 indeed shows that the derivative of the $C_L - s/d$-curve obtained by using the CFD model agrees well with experimental findings by Thang and Naudascher [3]. Therefore, the presence of positive or negative hydrodynamic stiffness due to flow as a function of the gap-ratio can be identified quite well using the CFD model.

Figure 5.9 shows the $C_L$-curves at the as a function of the gate inclination angle for both the experiments conducted by Thang and Naudascher [3] as well as results obtained in this research using CFD computations.

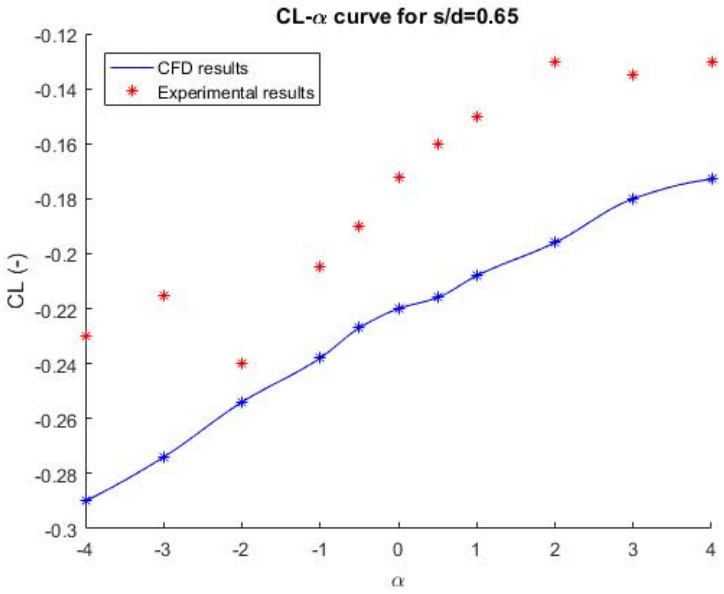


Figure 5.9: Liftcoefficient, $C_L$, at a gap ratio of 0.65 for different inclination angles, being $\alpha$

As for the $C_L - s/d$-curve the magnitude of the lift coefficient as a result of CFD computations is not equal to results obtained by Thang and Naudascher [3]. As mentioned in section 3.4 the definition of damping is the following:

$$c = \frac{\partial F_y}{\partial \frac{dy}{dt}} \tag{5.14}$$

In which: c = Damping $[\frac{N}{ms}]$
$F_y$ = Force in y-direction [N]
$\frac{dy}{dt}$ = Velocity in y-direction $[\frac{m}{s}]$

The derivative of the $C_L - \alpha$-curve is a measure of the change of the upward force as a function of the vertical velocity of the HG, which is modelled using the inclination angle. Therefore the derivative of the $C_L - \alpha$-curve is a measure of hydrodynamic damping. For the $C_L - \alpha$-curve the most important aspect is the sign of the derivative for $\alpha = 0$ since the sign of the $C_L - \alpha$-curve for $\alpha = 0$ determines whether or not negative damping due to water flow occurs for a HG which is not moving.

### SENSITIVITY ANALYSIS

Differences in the outcome of the $C_L$-curves can be the result of many uncertainties regarding the performed research by Thang and Naudascher [3]. In order to check the influence of some of the uncertainties and possible inaccuracies, parameters used in the determination of the $C_L$-curves are varied.

The largest uncertainties lie in the determination of the downstream water level, being $h_2$, and the determination of the pressure distribution, which was done by Thang and Naudascher [3] using only five pressure sensors. The latter is of lesser importance for the larger gap-ratios since the pressure distribution is equalised over the gate underside. When the downstream water level is measured one millimetre lower than the water level really is, the lift coefficient will be overestimated by approximately 0.1. This difference is in fact large enough to cause the differences between the computations using CFD and the research performed by Thang and Naudascher [3]. Water levels currently still are difficult to measure accurately, let alone determining accurate water levels back in 1986 during the research performed by Thang and Naudascher [3].

The sensitivity analysis is elaborated in more detail in section D.2 in appendix D.

### 5.3.3. COMPARISON OF THE LIFT CURVES FOR HGS WITH DIFFERENT THICKNESSES

This section is used as preliminary results regarding the influence of the thickness on the hydrodynamic forces. Two different thicknesses are used to determine the influence of the thickness on the susceptibility of galloping-type vibrations. The HGs that are assessed in this section and in chapter 6 are five and ten centimetres thick. Figure 5.10 shows the $C_L$-curves as a function of the gap-ratio obtained by performing CFD simulations.

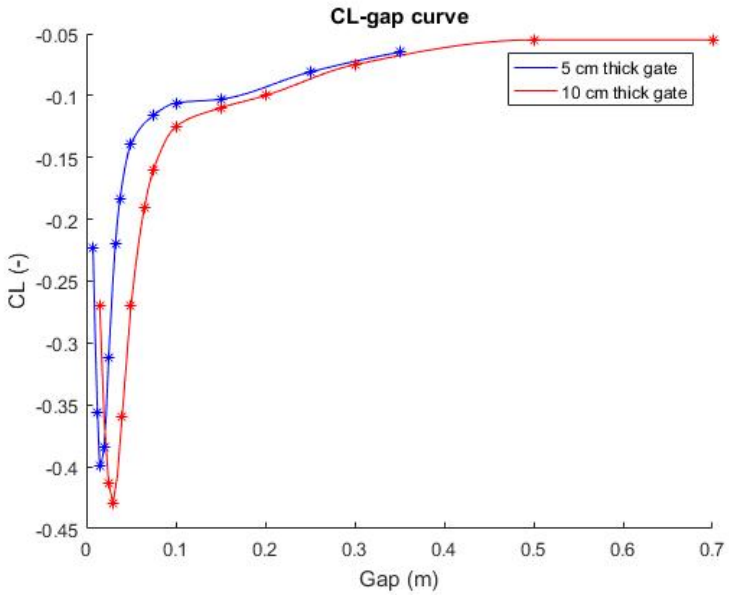


Figure 5.10: Lift curves as a function of the gap height

The plots in figure 5.10 are similar for the two thicknesses. Derivatives of the $C_L-$curves as a function of the opening height are plotted in figure 5.11. The figure shows similar behaviour for the two HGs, meaning that the $C_L$-coefficient as a function of the opening height is scalable with the thickness of the HG.

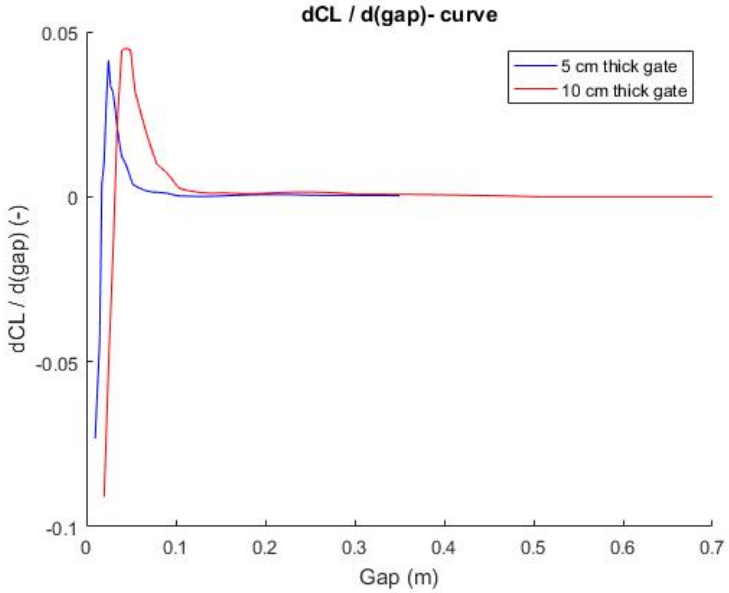


Figure 5.11: Derivatives of the curve of the lift-coefficient as a function of the gap height

When the x-axis is rewritten into the gap-ratio, being the opening height over the thickness of the HG, figure 5.12 is obtained. The $C_L-$curves as a function of the gap-ratio are equal for the two plots; as before the $C_L$-curve as a function of the opening height is scalable with the thickness of the HG.

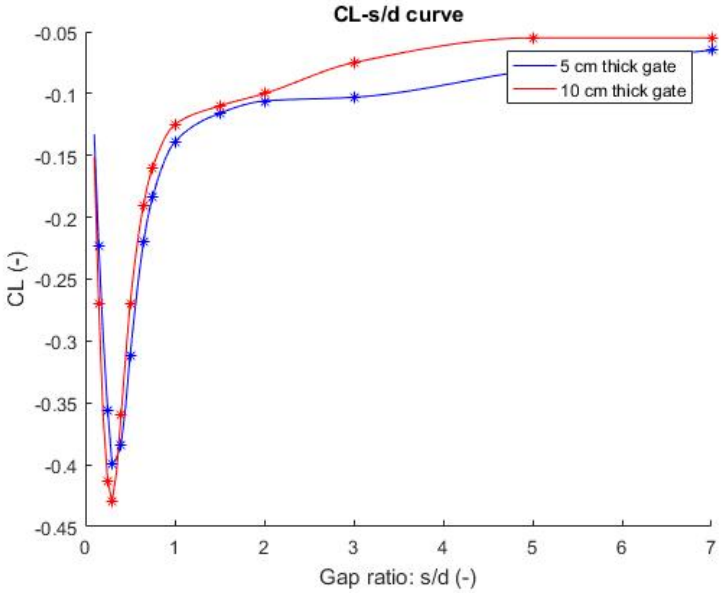


Figure 5.12: Lift curves as a function of the gap-ratio

### 5.3.4. FINAL CFD MODEL

The CFD model which is discussed in the validation of the CFD computations is modified to become more suitable for the analysis of vertical vibration. The adjustments are elaborated in appendix E and summarised in this section.

An FRP HG is designed having a thickness of ten centimetres after which a typical steel HG is designed having the same bending stiffness as the FRP design. This steel design is assessed using CFD.

The used hydraulic head is increased up to ten centimetres in order to obtain a larger flow velocity and therefore allowing for a larger maximum vertical velocity of the HG, since the vertical velocity of the HG is coupled to the flow velocity as mentioned in section 5.1 and in equation E.4 of appendix E. Gate inclinations are restricted to 2 % in order to limit the maximum of the relative gap decrease to 11.6 %. Combining the maximum inclination angle of the HG and the flow velocity in the vena contracta maximum absolute vertical velocities up to 0.05 metres per second can be simulated. As mentioned in section E.4 of appendix E.

## 5.4. ADDED HYDRODYNAMIC TERMS IN THE MODEL

The influence of the surrounding water on a HG is elaborated in this section. The flowing water impacts the vertically vibrating HG in terms of an added hydrodynamic mass, damping and stiffness.

### 5.4.1. ADDED HYDRODYNAMIC DAMPING

Since damping is equal to the derivative of a force as a function of the velocity, damping due to movement of the gate in flowing water can be derived from the force matrix, being the slope of the force parallel to the velocity-axis for the position and velocity at that time. Since water levels are far away from the underside of the HG damping due to wave radiation is not taken into account.

### 5.4.2. ADDED HYDRODYNAMIC STIFFNESS

CFD computations performed in this research will result in a force matrix as a function of the opening height and accompanying vertical velocity of the HG. Therefore, the influence of the water in terms of stiffness is depending on and can be derived for each combination of the opening height and vertical velocity. This means that for the slope of the force parallel to the position-axis for a certain opening height and velocity determines whether or not a positive of negative stiffness occurs due to the presence of water. Two stifnesses can be derived from the force matrix:

1. Stiffness due to buoyancy, see equation 3.17;
2. Stiffness due to flow, see equation 3.18.

The sudden stiffness as written in equation 3.20 is not included in the force matrix. This type of stiffness is present when due to large flow inertia a sudden change in position of the HG does not immediately change the discharge through the opening. Kolkman and Jongeling [2] state that this is the case for thick structure in which the inertia of the flow is large. Since the thickness of the HG at hand is in the order of only a few centimetres, the sudden stiffness is neglected.

### 5.4.3. ADDED HYDRODYNAMIC MASS

Unlike the hydrodynamic damping and stiffness (excluding the sudden stiffness) the added hydrodynamic mass is not incorporated in / cannot be derived from the force matrix. The influence of the added mass is maximal for a maximal added mass. The added mass for a vertically vibrating HG is maximal for the smallest opening heights as the force required to push away the water below the HG increases for smaller gap-ratios. The formulas used to possibly determine the added hydrodynamic mass are mentioned in figure 3.10 of section 3.4.

At first, in section 6.1, computations are performed without including the influence of the added mass. It is expected that the added mass does not influence the stability. Depending on the significance of the added mass with respect to the structural mass of the dynamic system, the added mas may or may not have a great influence on the natural frequency of the system.

## 5.5. PROCESSING OF CFD RESULTS TO DETERMINE THE DYNAMIC BEHAVIOUR OF A ONE DEGREE OF FREEDOM SYSTEM

Results obtained by performing CFD simulations are processed by using the Krylov-Bogoliubov method in Matlab. The theory behind this method is described in section 5.5.1 and further processed in section 5.5.3

### 5.5.1. KRYLOV-BOGOLIUBOV METHOD

As mentioned in section 5.1 (in equation 5.1) the equation of motion for the dynamical system at hand is written as:

$$m\frac{d^2y}{dt^2} + c\frac{dy}{dt} + ky = F(y, \frac{dy}{dt}) \tag{5.15}$$

In which the external damping coefficient, being c, is added to the right hand side. This equation is divided by the mass, being m, in order to come to the following form which is used in the Krylov-Bogoliubov technique:

$$\frac{d^2y}{dt^2} + \omega_0^2 y = \frac{F(y, \frac{dy}{dt}) - c\frac{dy}{dt}}{m} \tag{5.16}$$

In which $k/m$ is rewritten into the squared natural frequency of the system, being $\omega_0^2$, as mentioned in section 3.4 and appendix A.

The right hand side of equation 5.16 is denoted as:

$$\frac{F(y, \frac{dy}{dt}) - c\frac{dy}{dt}}{m} = RHS(m, c, y, \frac{dy}{dt}) \tag{5.17}$$

For cases in which the right hand side of equation 5.16 is equal to zero, being an unperturbed oscillator without damping, the solution becomes:

$$y = Acos(\omega_0 t + \phi) \tag{5.18}$$

| | | | | |
|---|---|---|---|---|
| In which: | $y$ | = | Position of the oscillator | $[m]$ |
| | $A$ | = | Amplitude of vibration | $[m]$ |
| | $\phi$ | = | Phase shift | $[rad]$ |

The KB method of averaging takes this solution form as the basis of the analysis. The solution of the KB method is in the form of equation 5.18 but then with a time dependent amplitude and phase shift. Therefore, the solution comes in the following form:

$$y = A(t)cos(\omega_0 t + \phi(t)) \tag{5.19}$$

#### GOVERNING EQUATIONS

In order to solve for the unknown time dependent amplitude and phase shift, two equations are to be solved, which will be done in section 5.5.2. First of all the the derivative of equation 5.18, being the solution of the velocity, is equal to:

$$\frac{dy}{dt} = -A\omega_0 sin(\omega_0 t + \phi) \tag{5.20}$$

The derivative of equation 5.19, being the velocity, using the KB method in which the amplitude and phase shift are time dependent becomes:

$$\frac{dy}{dt} = \frac{dA}{dt}cos(\omega_0 t + \phi(t)) - A(\omega_0 + \frac{d\phi}{dt})sin(\omega_0 t + \phi) \tag{5.21}$$

The second derivative of the location of the unperturbed oscillator, being the acceleration, becomes:

$$\frac{d^2y}{dt^2} = -A\omega_0^2 cos(\omega_0 t + \phi) \tag{5.22}$$

Using the KB method it is assumed that the amplitude and phase shift are slowly varying variables, allowing for the simplification in which the higher order derivatives are neglected. Which means that the acceleration of the oscillator using the KB method becomes:

$$\frac{d^2y}{dt^2} = -2\frac{dA}{dt}(\omega_0 + \frac{d\phi}{dt})sin(\omega_0 t + \phi) - A\omega_0^2 cos(\omega_0 t + \phi) \tag{5.23}$$

### 5.5.2. SOLVING FOR TIME DEPENDENT VARIABLES

The velocity of the unperturbed oscillator should be equal to the velocity obtained from using the KB method in which the amplitude and phase shift are time dependent. This results in the following equation:

$$-A\omega_0 sin(\omega_0 t + \phi) = \frac{dA}{dt}cos(\omega_0 t + \phi) - A(\omega_0 + \frac{d\phi}{dt})sin(\omega_0 t + \phi) \tag{5.24}$$

The next equation is that the formulae for the location and acceleration found for the KB method should comply with the adjusted equation of motion in equation 5.16. Resulting in:

$$\frac{dA}{dt}\omega_0 sin(\omega_0 t + \phi) - A\omega_0\frac{d\phi}{dt}cos(\omega_0 t + \phi) = RHS(m, c, y, \frac{dy}{dt}) \tag{5.25}$$

Using equation 5.24 equation 5.25 and solving for the unknown time dependent amplitude and phase shift, one finds:

$$\frac{dA}{dt} = \frac{RHS(m, c, y, \frac{dy}{dt})}{\omega_0} sin(\omega_0 t + \phi) \tag{5.26}$$

and

$$\frac{d\phi}{dt} = \frac{RHS(m, c, y, \frac{dy}{dt})}{\omega_0 A} cos(\omega_0 t + \phi) \tag{5.27}$$

For a numerical simulation of dynamic behaviour in MATLAB, using the force matrix $F(y, \frac{dy}{dt})$, which is a result of several CFD computations, equation 5.26 and equation 5.27 are computed for every time step, being $\Delta t$.

The updated amplitude and phase shift for the next time step become:

$$A(j+1) = A(j) + \frac{dA}{dt}\Delta t \tag{5.28}$$

and

$$\phi(j+1) = \phi(j) + \frac{d\phi}{dt}\Delta t \tag{5.29}$$

In which: $j$ = The $j^{th}$ time step
$j+1$ = The next time step

#### INSTABILITY INDICATOR

Instability is determined based on the situation in which the averaged absolute velocity is increasing over time. This is mathematically elaborated as shown in equation 5.30:

$$\frac{1}{n/2}\sum_{i=n/2}^{i=n}\left|\frac{dy_i}{dt}\right| \geq \frac{1}{n/2}\sum_{i=1}^{i=n/2}\left|\frac{dy_i}{dt}\right| \tag{5.30}$$

In which: n = Number of time steps [-]
i = The $i^{th}$ time step [-]

Using this equation of the averaged absolute velocity instability is found for:

$$\frac{\frac{1}{n/2}\sum_{i=n/2}^{i=n}\left|\frac{dy_i}{dt}\right|}{\frac{1}{n/2}\sum_{i=1}^{i=n/2}\left|\frac{dy_i}{dt}\right|} \geq 1 \tag{5.31}$$

### 5.5.3. ELABORATION OF NUMERICAL ANALYSIS OF GALLOPING IN MATLAB

The method as described in section 5.5 is elaborated using MATLAB. This section elaborates on the key steps required to apply the KB method on the dynamical system at hand. First the force matrix is composed based on results from CFD computations in section 5.5.3. After which the input parameters for the dynamical system are chosen in section 5.5.3. Numerical parameters and initial conditions are then set in sections 5.5.3 and 5.5.3. The time loop including steps is used to describe the KB method in terms of the application in a numerical scheme in section 5.5.3. Finally the interesting plots are mentioned in section 5.5.3.

#### FORCE MATRIX

First of all the force matrix is constructed which will form the basis of the analysis. Forces resulting from CFD computations for specific opening heights and inclination angles of the HG are read from imported csv-files (comma-separated value files ). Since the CFD computations are performed in a transient state an average force is obtained for the last twenty seconds of the physically modelled time. This is done for all performed CFD computations for different combinations of the opening height and inclination angle of the HG. The inclination angle of the HG is rewritten into a mimicked vertical velocity as written in equation E.4.

The force matrix is determined for a number vertical velocities (different angles at which the HG is placed) and a number of vertical positions. Therefore, the next step is to interpolate the force between chosen combinations of vertical velocities and the opening heights. This results in a matrix for all combinations between the ranges of the opening heights and vertical velocities. A three-dimensional graph for all combinations of the vertical velocity and opening heights can be plotted to visualise the changes of the force for a changing position of the gate (opening height) and accompanying velocity (upward or downward).

The rows of the matrix are used for different opening heights and the columns are used for different vertical velocities of the HG.

An important note regarding the interpolation is that for a matrix the first index denotes the row number and the second index denotes the column number, while for the two-dimensional interpolation function, being interp2, the first index denotes the column number and the second index denotes the row number. So the indices are switched between matrix(row,column) to matrix(column,row). Not knowing this resulted in an incorrect response of the system and consequently in a delay of approximately two weeks in the final stage of this research.

#### HYDRODYNAMIC DAMPING AND STIFFNESS

The hydrodynamic damping and hydrodynamic stiffness can be derived from the force matrix in the previous step as explained in section 5.4. This is done by determining the derivative of the force matrix in direction of the vertical velocity and the derivative of the force matrix in direction of the opening height respectively. The obtained hydrodynamic damping and hydrodynamic stiffness are then plotted in a figure as a function of the vertical velocity and opening height.

#### INPUT PARAMETERS DYNAMICAL SYSTEM

Since the dynamical model consists of a mass-spring-damper system with a vertical degree of freedom, the stiffness and mass are set. The natural frequency is computed for the combination of mass and stiffness. It is important to note that the natural frequency of the system should result in a reduced velocity between five and sixty, as mentioned in Thang and Naudascher [3], since that is the range of reduced velocities in which galloping has been observed. Another note is that equation 5.16 shows that the RHS of the equation of motion used in the KB method is equal to the force, being an element of the force matrix as described in section 5.5.3 divided by the mass, e.g. increasing the mass by a factor two reduces the RHS of equation 5.16 by a factor two.

#### PARAMETERS REGARDING NUMERICAL COMPUTATIONS

The total physical time which is to be modelled is set, being $t_{tot}$. Also the time step, being $\Delta t$, is set. As the KB method assumes a slowly varying amplitude and phase shift, a small time step of one millisecond is deemed appropriate. The number of time steps is computed by dividing the physical time time to be modelled by the size of the time step (in seconds): $n = t_{tot}/\Delta t$.

#### LOOP FOR DIFFERENT INITIAL OPENING HEIGHTS

There are two initial conditions to be set. First of all the initial opening heights, being $y_0$, are changed in the loop. Secondly the initial velocity is set. The combination of these initial conditions is used to find the initial force at t=0. Since the opening height at t=0 is chosen to be the y-coordinate around the which the dynamic system will oscillate the position of the bottom of the hydraulic gate is written as:

$$y_{t=0} = A_0 cos(\phi_0) + y_0; \tag{5.32}$$

Since the position of the bottom of the gate at t=0 is equal to $y_0$, $\phi$ at t=0 is equal to $-1/2\pi$ The initial amplitude, being $A_0$ is determined based on the initial velocity.

The initial force is then computed by first determining the required element in the matrix. Based on the initial opening height a matrix row value is determined. The same is done for the initial vertical velocity of the HG. Computation of the required row and column is done as follows:

$$Row_{t=0} = ((y_0 - y_{min})/\Delta y)(nn-1)+1; \tag{5.33}$$

| | | | | |
|---|---|---|---|---|
| In which: | $y_0$ | = | Initial opening height | $[m]$ |
| | $y_{min}$ | = | Minimal used opening height | $[m]$ |
| | $\Delta y$ | = | Difference between the maximal and minimal used opening height | $[m]$ |
| | $nn$ | = | Number of rows in the force matrix | $[-]$ |

and

$$Column_{t=0} = ((\frac{dy}{dt}_0 - \frac{dy}{dt}_{min})/\Delta\frac{dy}{dt})(mm-1)+1; \tag{5.34}$$

| | | | | |
|---|---|---|---|---|
| In which: | $\frac{dy}{dt}_0$ | = | Initial vertical velocity | $[m/s]$ |
| | $\frac{dy}{dt}_{min}$ | = | Minimal used vertical velocity | $[m/s]$ |
| | $\Delta\frac{dy}{dt}$ | = | Difference between the maximal and minimal used velocities | $[m/s]$ |
| | $mm$ | = | Number of columns in the force matrix | $[-]$ |

Interpolating for the specific initial row number and column number in the force matrix results in the initial force.

#### LOOP FOR DIFFERENT APPLIED EXTERNAL DAMPING COEFFICIENTS

Now the applied external damping is varied within the loop for initial opening heights.

#### TIME LOOP

Now a for-loop is being used within the loop for different applied external damping to determine the position and velocity of the mass-spring system for all time steps in combination with the applied damping and initial opening height.

First of all the position and velocity at the beginning of the time step is determined using formulae given in section 5.5.

Now the force acting on the system is determined based on the same principles as mentioned in section 5.5.3, being the interpolated combination of the position and vertical velocity. The force acting on the system is now determined although we are interested in the difference between this force and the initial force. Therefore, the initial force is subtracted from the force found using interpolation.

As mentioned in equation 5.26 and equation 5.27 the amplitude ($A$) and phase shift ($\phi$) are computed to be used in the next time step.

In order make the computations more time efficient in case of an exceedance of the range of possible positions and the range of vertical velocities, related to the required row and column in the force matrix, the loop breaks when the required row or column becomes smaller than one or if the required row or column is larger than the number of rows resp. columns.

#### CHECK ON STABILITY

As mentioned in section 5.5.2 stability of the system is analysed by comparing the average vibration velocity of the first half of the simulated time with the second half of the simulated time. If the average vibration velocity is increasing over time this indicates instability. The check written in equation 5.31 is then performed for a range of initial opening heights (more on this in chapter 6) and a range of applied external damping coefficients (from zero to a certain value, also more on this in chapter 6). After the check on stability for each combination of initial opening heights and applied external damping coefficient the loops regarding the different applied damping coefficients and initial opening heights are finished.

#### PLOTS

Plots of the upward hydrodynamic force acting on the HG are made after which the distribution of the hydrodynamic damping and stiffness are plotted. Plots are made of the position of the HG as a function of time and a comparison of the required damping for the different HGs is plotted.

## 5.6. CONCLUSIONS

Conclusions regarding the research approach are mentioned in section 5.6.1. Concerning the validation of the model conclusions are drawn in section 5.6.2.

### 5.6.1. GENERAL CONCLUSIONS

An FRP hydraulic gate will most likely have a different thickness than a steel hydraulic gate. The thickness of the hydraulic gate greatly influences the pressure distribution underneath the hydraulic gate. Consequently it may be the case that a smaller or larger relative under pressure may lead to a smaller or larger susceptibility to undesirable vibrations;

A larger thickness also means that the critical gap height is larger, resulting in a longer period of time in which self excitation may occur and consequently a larger impact velocity in case of collision with the floor underneath the hydraulic gate;

The low deformation capacity of FRP might result in failure of the hydraulic gate in case of an impact with the structure underneath the hydraulic gate.

### 5.6.2. VALIDATION OF THE MODEL

In general it can be stated that results from CFD computations agree well with findings performed by Thang and Naudascher [3]. Qualitative descriptions by Thang and Naudascher [3] for three different gap ratio ranges are confirmed and elaborated further.

The shapes of the obtained $C_L$-curves agree well with results from experiments albeit a bit shifted. Most importantly the derivatives of these curves are practically the same for the experiments and for results from CFD computations. What it means if the derivatives are equal is that for both cases, CFD computations and experimental results [3], self-excitation, being galloping, will occur for the same situations.

Since the $C_L$-curves do not perfectly match results from Thang and Naudascher [3] a sensitivity analysis has been performed. Uncertainties in the performed experiments are found in the use of only five pressure sensors at the bottom of the gate.

It is also not unlikely that measurements of the water levels may have been inaccurate. Even today, being over thirty years after the experiments performed by Thang and Naudascher [3] it is not easy to obtain accurate water levels. A deviation of the measured downstream water level of one millimetre may influence an obtained value of the lift coefficient by as much as 0.1. This may have led to a overestimation of the found $C_L$ values. Underestimating the downstream water level with one millimetre for a gap of thirty five centimetres increases the value of $C_L$ from -0.05 to 0.05. It is a plausible assumption that the water levels may not have been measured with accuracies of one millimetre.

The location of the down stream water level, being $h_2$ has been mentioned to be measured "about 15 cm behind the gate" [3]. Analysis shows that measurements of the downstream water level at ten and twenty centimetres behind the gate instead of fifteen centimetres, results in deviations of the $C_L$ values of not even one percent. This makes the influence of inaccuracy of the position of measurements of the downstream water level negligible.

A similar conclusion can be drawn for the measurements of the upstream water level. Locations of measurements are not mentioned in Thang and Naudascher [3]. Therefore, a wide variety of positions has been tested for the influence of the position of measurements on the resulting values of $C_L$. Deviations from the average value of $C_L$ for these positions has a maximum of only 1.2 %, meaning that also the influence of the location of measurement of the upstream water level on results of the $C_L$-curves can be neglected.

Performing the physical experiments (Thang and Naudascher [3]) using CFD is not the easiest due to the lack of data of the performed physical experiments. There were knowledge gaps in the paper regarding hydraulic conditions, positions of the pressure sensors and locations of measurements. Luckily some missing data, such as the experimental water levels, have been derived from figures presented in Thang and Naudascher [3].

# 6

# ANALYSIS OF GALLOPING-TYPE VIBRATIONS

In this chapter the influence of two distinct differences between an FRP HG and a steel HG, as mentioned in the introduction of chapter 5, on the susceptibility to galloping-type vibrations are assessed using the method described in chapter 5. Since a two-dimensional CFD model is used the third dimension, being the width of the HG is not included. Therefore, forces, damping coefficients and stiffness coefficients shown in this chapter are values per metre width of the HG.

First of all, the influence of a larger thickness on the susceptibility to galloping-type vibrations is assessed using a case study in section 6.1. Secondly, the case study to determine the influence of a different design for FRP HGs than for steel HGs on the susceptibility to galloping-type vibrations is elaborated in section 6.2. Based on the two case studies conclusions regarding the dynamic stability of FRP HGs are drawn in section 6.4.

The following hydraulic input parameters are used:

| | | | |
|---|---|---|---|
| Upstream water level | = | 1.1 | $[m]$ |
| Downstream water level | = | 1 | $[m]$ |

## 6.1. INFLUENCE OF A LARGER THICKNESS ON THE HYDRODYNAMIC FORCES ACTING ON THE HG

In this section the differences between the forces acting on the two HGs with different thicknesses are elaborated. The geometry of the two HGs is mentioned in section 5.2.1 and shown in fig 6.1.


Figure 6.1: Geometry of the two HGs

Figure 6.2 illustrates the velocity field of the HG with a thickness of five centimetres, an upstream water level of one point one metre, a downstream water level of one metre and an opening height of ten centimetres. Figure 6.3 shows a similar velocity field for the HG with a thickness of ten centimetres.

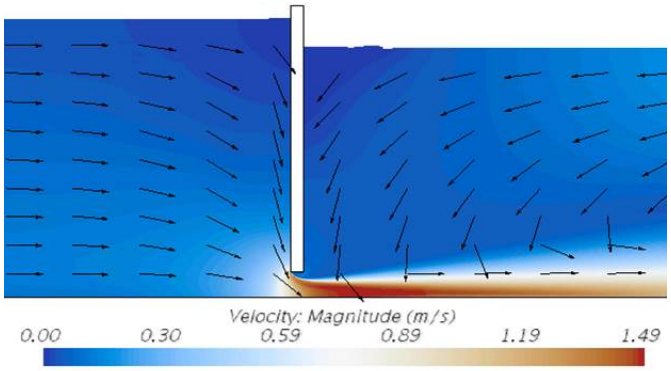


Figure 6.2: Velocity field of the thin HG

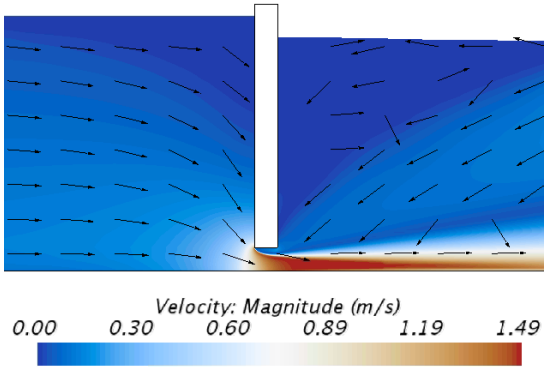


Figure 6.3: Velocity field of the thick HG

### 6.1.1. HYDRODYNAMIC FORCES

After all chosen combinations of the opening height and accompanying vertical velocity are simulated in STAR-CCM+ the resulting upward forces are exported into a comma separated value (csv) file. This file is loaded into Matlab after which the upward force is averaged over the last twenty seconds of the simulation to remove small force fluctuations over time. Figure 6.4 shows plots of the force as a function of the position, being the opening height, and vertical velocity of the HG.

| | | | | |
|---|---|---|---|---|
| In which: | $F$ | = | Upward force acting the HGs | $[N]$ |
| | $s$ | = | Opening height | $[m]$ |
| | $dy/dt$ | = | Vertical HG velocity | $[m/s]$ |

For rectangular plates the distinct local minimum for the small opening height agrees well with the plots of the $C_L$-curve in section 5.3.2. The plots clearly show that the upward force of the thick HG is approximately a factor two larger than the upward force resulting from computations using the thin HG. This can be attributed to the fact that the thick HG displaces twice as much water as the thin HG, i.e. the upward force due to buoyancy is twice as large. This buoyancy term translates to a stiffness term which is further elaborated in section 6.1.3.

When the upward force is divided by the thickness of the HG and the opening height is rewritten into the gap-ratio, being the opening height over the HG thickness, figure 6.5 is obtained. figure 6.5 clearly shows that the force is scalable with the thickness of the HG.

### 6.1.2. HYDRODYNAMIC DAMPING

As mentioned in section 5.4 the hydrodynamic damping can be derived from the force matrices in the previous section. This is done by computing the derivatives of these force matrices in the direction of vertical velocity of the HG and results in figure 6.6. The colour bar at the right side of the figures indicates the value of the hydrodynamic damping coefficient.

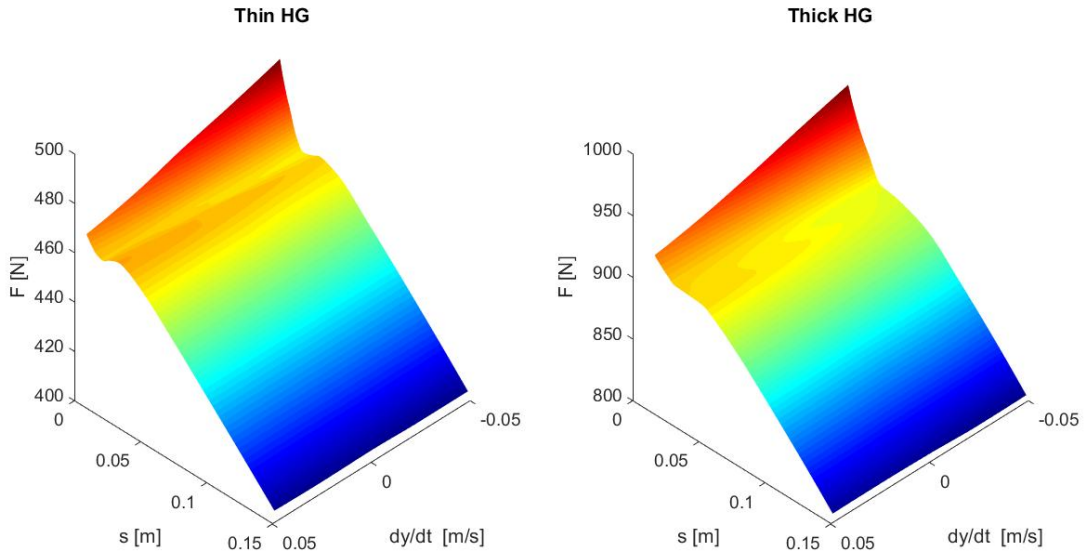


Figure 6.4: Force plots as a function of the HG opening height and vertical velocity of the HG

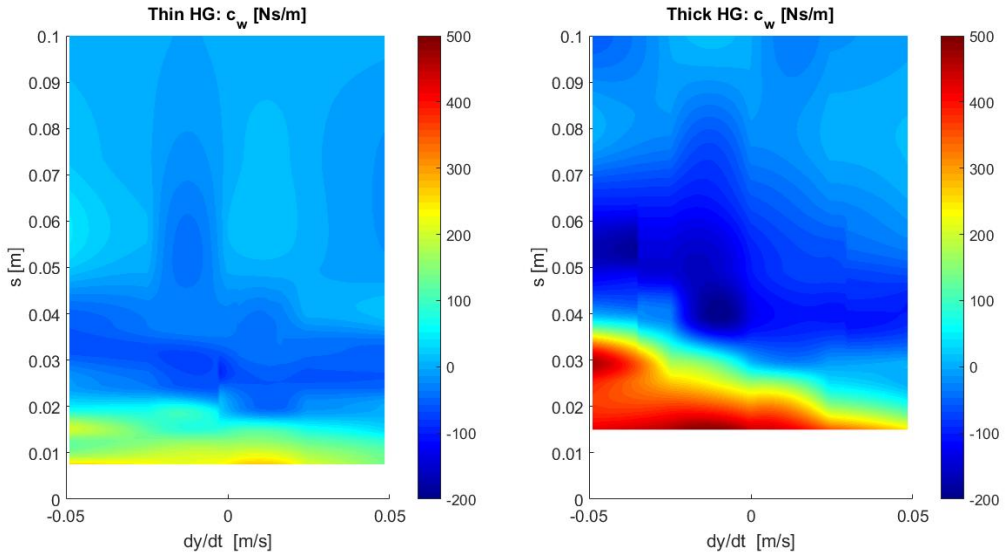


Figure 6.6: Hydrodynamic damping plots as a function of the HG opening height and vertical velocity of the HG

| | | | | |
|---|---|---|---|---|
| In which: | $c_w$ | = | Hydrodynamic damping coefficient | $[N]$ |
| | $s$ | = | Opening height | $[m]$ |
| | $dy/dt$ | = | Vertical HG velocity | $[m/s]$ |

Based on figure 6.6 the maximum negative hydrodynamic damping for the thin HG is found to be 100 Ns/m and the maximum negative hydrodynamic damping for the thin HG is 200 Ns/m. Therefore, it is expected that applying an external damping coefficient being a bit larger than the negative hydrodynamic damping would yield a stable HG. Section 6.3 will further elaborate the required damping coefficients to prevent galloping-type vibrations and return to this hypothesis.

When the figure 6.6 is rewritten in the same manner as done in rewriting figure 6.4 in order to obtain figure 6.5, figure 6.7 is obtained.

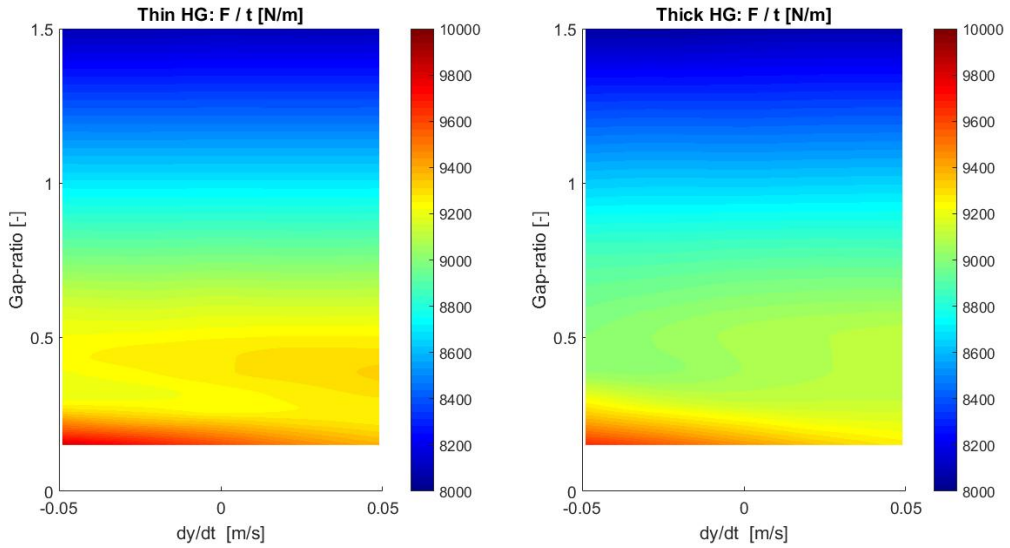


Figure 6.5: Hydrodynamic force plots as a function of the HG gap-ratio and vertical velocity of the HG scaled with the thickness of the HG

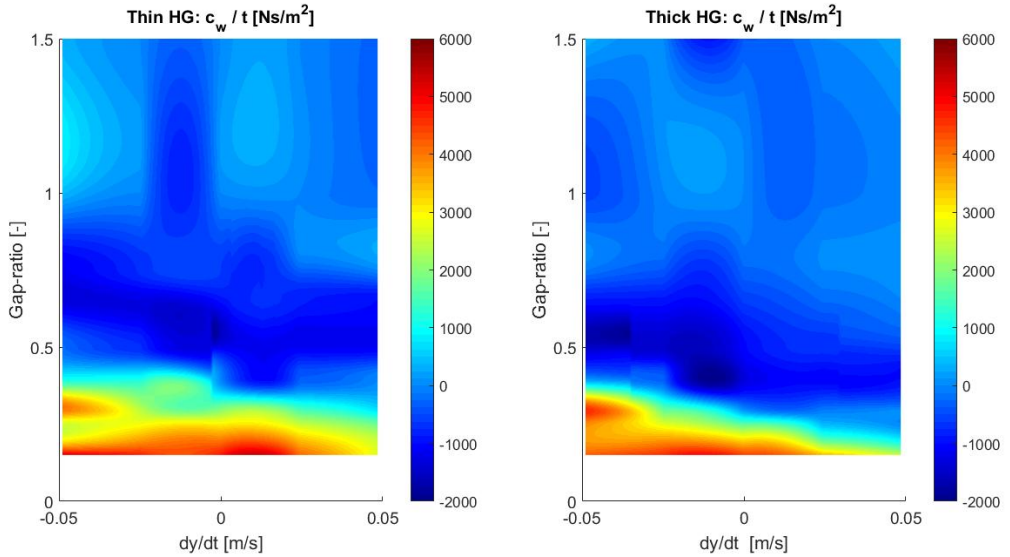


Figure 6.7: Hydrodynamic damping plots as a function of the HG gap-ratio and vertical velocity of the HG scaled with the thickness of the HG

As for figure 6.5 results scale nicely with the thickness of the HG since similar plots are shown for the thin and thick HG. The linear scaling of the damping coefficient with the thickness as a function of the gap ratio is an important result. Furthermore, figure 6.7 shows that the range of opening heights at which negative damping occurs is scalable with the thickness of the HG.

### 6.1.3. HYDRODYNAMIC STIFFNESS

The hydrodynamic damping coefficients are determined based on the force matrices. The same method is applicable to determine the hydrodynamic stiffness, but now the derivative of the force matrices is computed in direction of the opening height. Plots of the hydrodynamic stiffness are shown in figure 6.8.

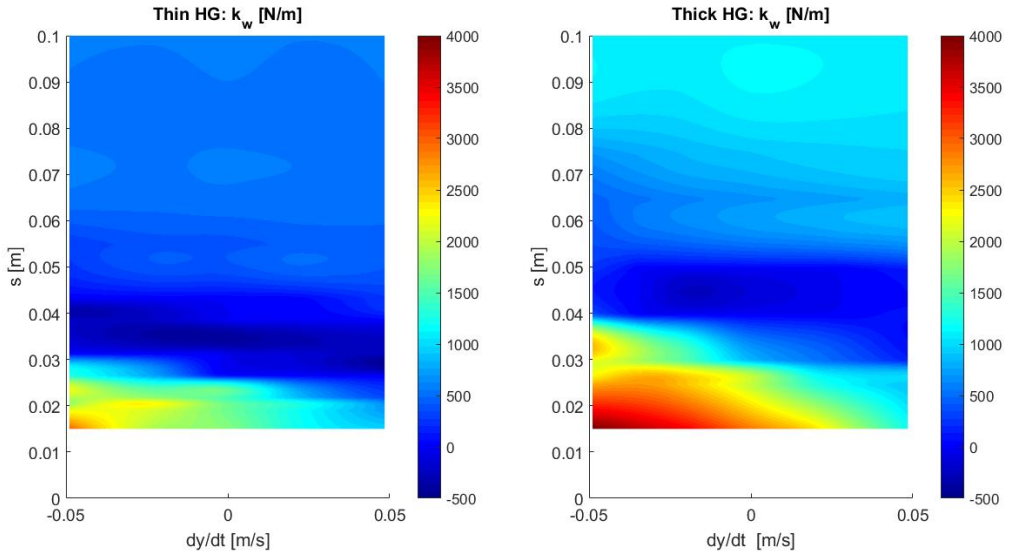


Figure 6.8: Hydrodynamic stiffness plots as a function of the HG opening height and vertical velocity of the HG

| | | | | |
|---|---|---|---|---|
| In which: | $k_w$ | = | Hydrodynamic stiffness coefficient | $[N]$ |
| | $s$ | = | Opening height | $[m]$ |
| | $dy/dt$ | = | Vertical HG velocity | $[m/s]$ |

As mentioned in the section regarding the two force matrices the hydrodynamic stiffness for the larger opening heights, being an almost static situation, the hydrodynamic stiffness is approximately a factor two higher for the thick HG than for the thin HG (around 1000 N/m and 500 N/m respectively). The thin HG has a larger area of negative hydrodynamic stiffness although the hydrodynamic stiffness is quite small compared to the applied mechanical stiffness of the HG suspension in section 6.3.

Figure 6.9 shows a plot of the scaled hydrodynamic stiffness. As expected for larger gap-ratios the hydrodynamic stiffness values become the same. The thin HG shows a larger range of the gap-ratio of negative hydrodynamic stiffness and a relatively larger positive hydrodynamic stiffness for small gap-ratios.

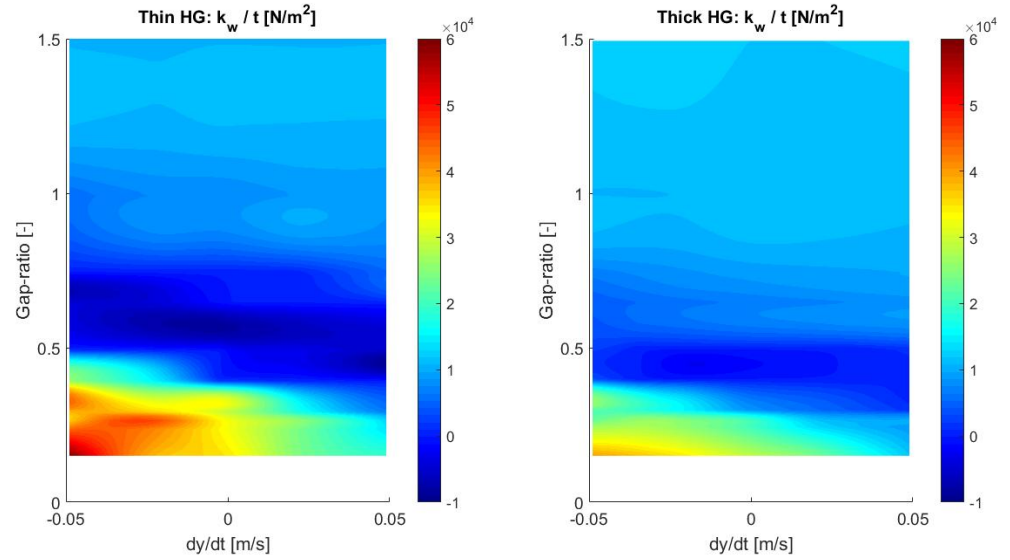


Figure 6.9: Hydrodynamic stiffness plots as a function of the HG gap-ratio and vertical velocity of the HG scaled with the thickness of the HG

## 6.2. INFLUENCE OF A DIFFERENT DESIGN ON THE HYDRODYNAMIC FORCES ACTING ON THE HG

In this section the influence of a different design for an FRP HG than for a steel HG on the hydrodynamic loading is discussed. In section 5.2.2 a design is made. The design of the two HG is shown in figure 6.10.

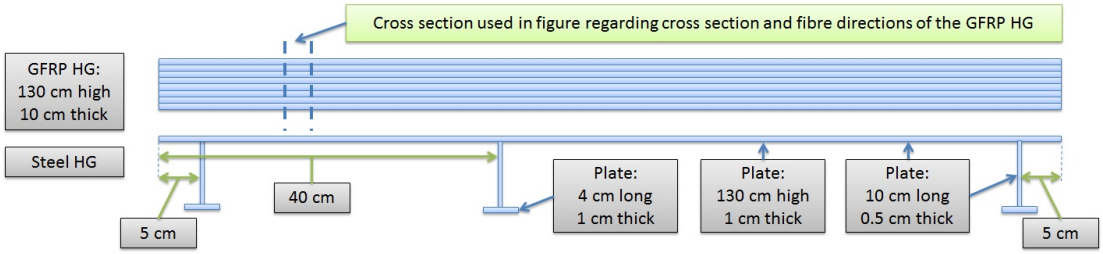


Figure 6.10: Designs of the GFRP HG and steel HG

Hydrodynamic forces are computed using CFD for both the FRP HG and a steel HG. Figure 6.11 illustrates the velocity field of the steel HG, an upstream water level of one point one metre, a downstream water level of one metre and an opening height of ten centimetres.

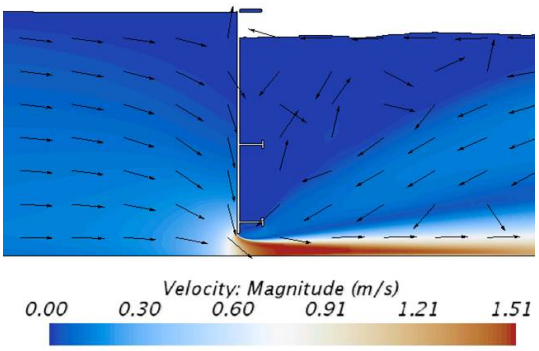


Figure 6.11: Velocity field for the steel HG

### 6.2.1. HYDRODYNAMIC FORCES

Upward forces are determined for this steel structure for different positions and accompanying vertical velocities to obtain the new force matrix presented in the right plot of figure 6.12. This is performed in the same manner as for the thin and thick HG.

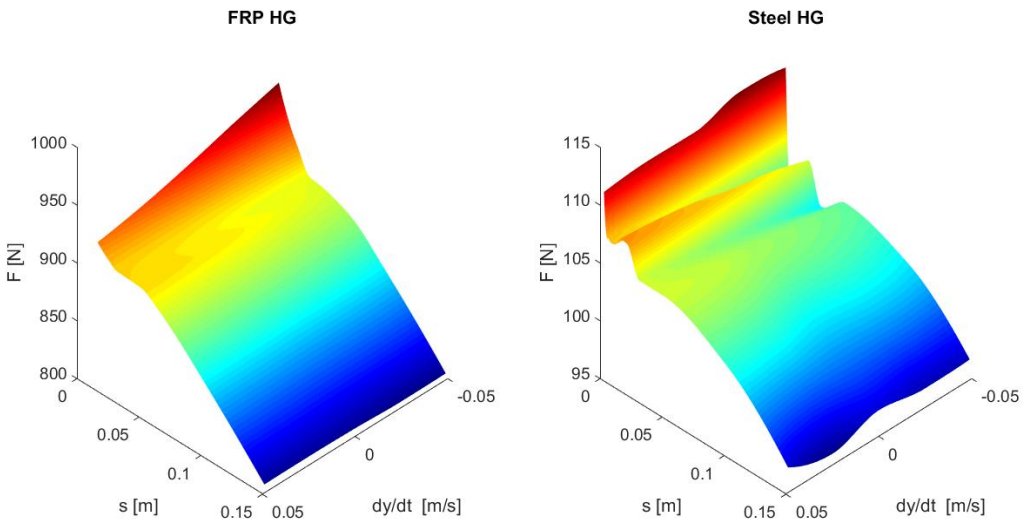


Figure 6.12: Force plots as a function of the HG opening height and vertical velocity of the HG

| | | | | |
|---|---|---|---|---|
| In which: | $F$ | = | Upward force acting the HGs | $[N]$ |
| | $s$ | = | Opening height | $[m]$ |
| | $dy/dt$ | = | Vertical HG velocity | $[m/s]$ |

Clearly for the steel HG design the upward hydrodynamic force does not vary as much as the thin or thick HG. This has to do with the fact that the upward (buoyancy) force is a lot less and changes less due to the small thickness of the vertical plate, being one centimetre thick. Therefore, the steel HG has a different scaling of the colours than the FRP HG, i.e. thick HG. The range of the upward force is scaled with a factor ten.

Another difference between the two plots is that the distinct local minimum for the small opening heights that is present for the thin and thick HG in figure 6.4 is not present for the steel design. The steel design has two local minima instead.

The hydrodynamic forces scaled by the thickness of the HG as a function of the gap-ratio and vertical velocity of the HG are plotted in figure 6.13.

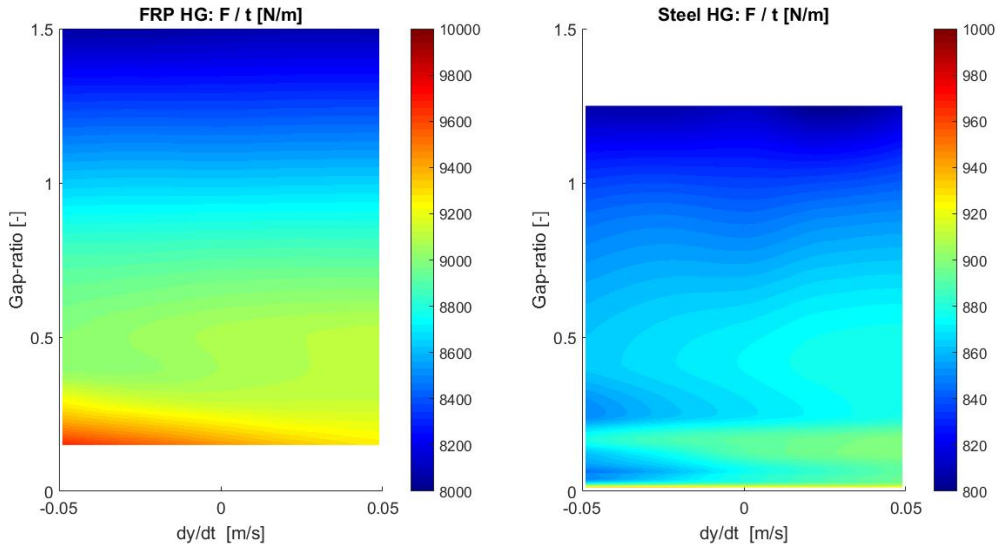


Figure 6.13: Hydrodynamic force plots as a function of the HG gap-ratio and vertical velocity of the HG scaled with the thickness of the HG

As for figure 6.12 the plots of the hydrodynamic force are completely different due to the difference in the design of an FRP HG and a typical steel HG.

### 6.2.2. HYDRODYNAMIC DAMPING

Performing the same procedure as before in section 6.1.2 the hydrodynamic damping coefficients are determined by computing the derivative of the force matrix in direction of the vertical velocity of the HG and result in the right plot in figure 6.14.

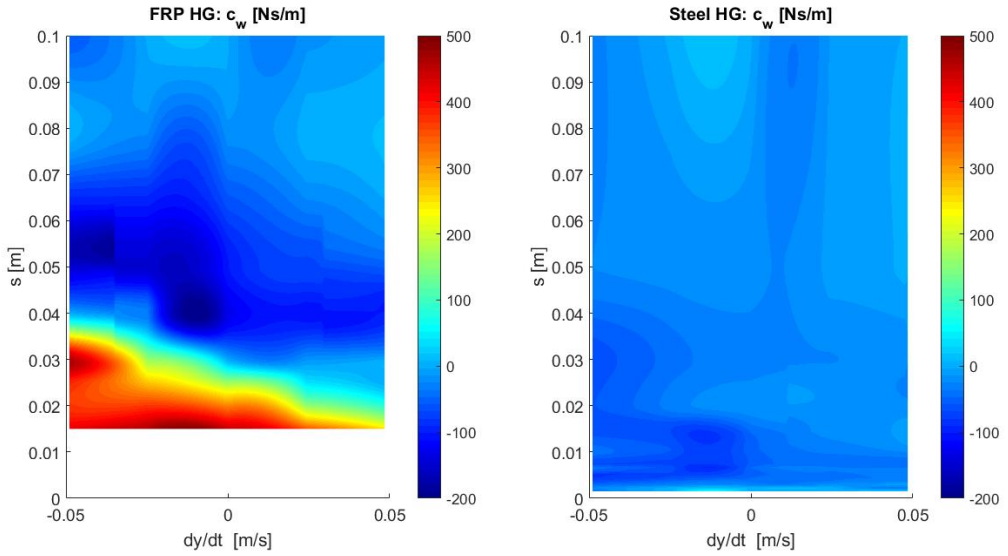


Figure 6.14: Hydrodynamic damping plots as a function of the HG opening height and vertical velocity of the HG

| | | | | |
|---|---|---|---|---|
| In which: | $c_w$ | = | Hydrodynamic damping coefficient | $[N]$ |
| | $s$ | = | Opening height | $[m]$ |
| | $dy/dt$ | = | Vertical HG velocity | $[m/s]$ |

The maximum negative hydrodynamic damping coefficient in case of the steel HG can be derived from figure 6.14 as mentioned before in section 6.1.2 and is found to be 90 Ns/m whereas the same negative hydrodynamic damping coefficient for the FRP HG is a factor two higher, begin 200 Ns/m. The scaled plot of the hydrodynamic damping is plotted in figure 6.15.

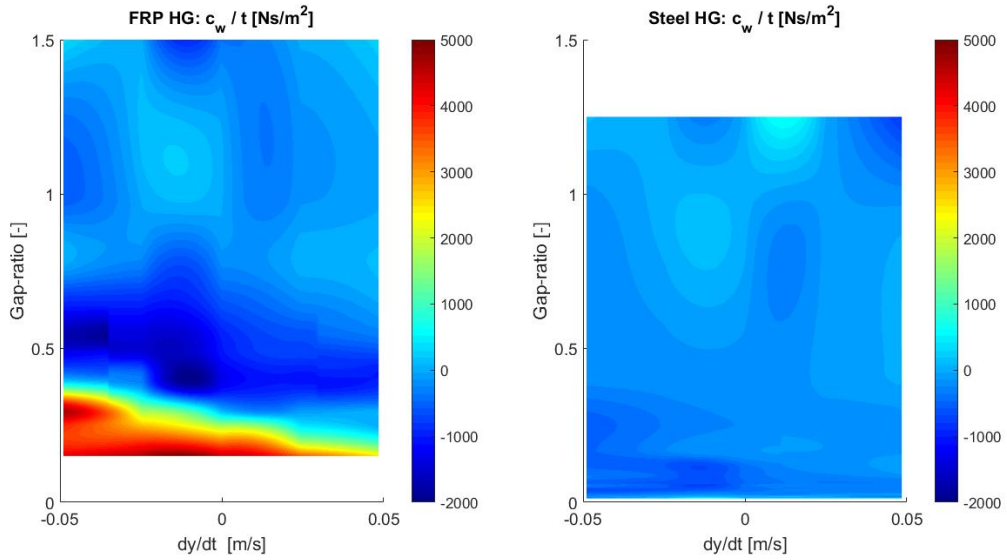


Figure 6.15: Hydrodynamic damping plots as a function of the HG gap-ratio and vertical velocity of the HG scaled with the thickness of the HG

Figure 6.15 shows that the scaled hydrodynamic damping is much higher for the FRP HG for small gap-ratios than for the steel HG and much lower for gap-ratios around 0.5.

### 6.2.3. HYDRODYNAMIC STIFFNESS

Computing the derivative of the force matrix in direction of the opening height results in the hydrodynamic stiffness of the steel HG as shown in the right plot of figure 6.16

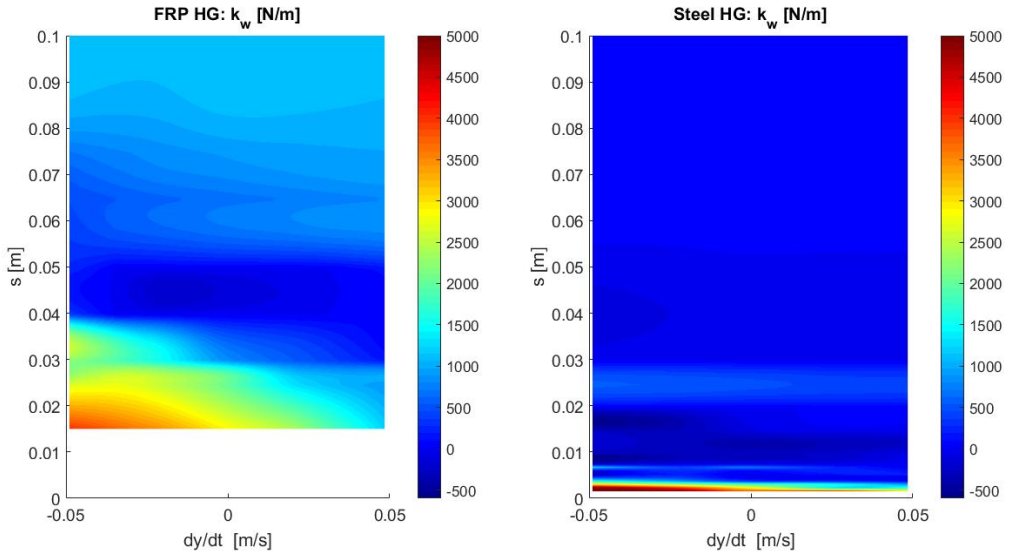


Figure 6.16: Hydrodynamic stiffness plots as a function of the HG opening height and vertical velocity of the HG

| | | | | |
|---|---|---|---|---|
| In which: | $k_w$ | = | Hydrodynamic stiffness coefficient | $[N]$ |
| | $s$ | = | Opening height | $[m]$ |
| | $dy/dt$ | = | Vertical HG velocity | $[m/s]$ |

The plots in figure 6.12 have shown that the upward force is much lower for the steel HG than for the FRP HG, primarily due to the lower cross-sectional area of the HG. Therefore, the upward force due to buoyancy and consequently the hydrodynamic stiffness are lower for a steel HG with respect to the FRP HG, as can be seen in figure 6.16. Figure 6.17 shows the scaled hydrodynamic stiffness. For figure 6.17 the same conclusions hold as for figure 6.16

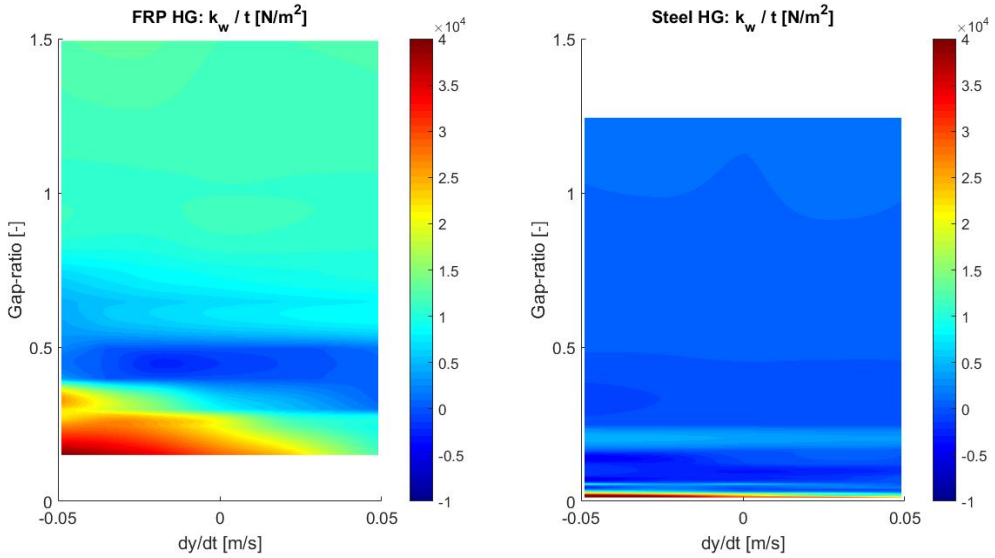


Figure 6.17: Hydrodynamic stiffness plots as a function of the HG gap-ratio and vertical velocity of the HG scaled with the thickness of the HG

## 6.3. RESPONSE AND STABILITY OF THE HGS TO THE FLOW-INDUCED LOADING

The response of the three HGs that are used in the previous sections are determined based on different initial opening heights and are given a small disturbance, being an initial vertical velocity in upward direction of 0.005 m/s. Input parameters regarding the dynamic properties of the three HGs are shown in table 6.1. The applied external damper is varied in this section.

Table 6.1: Dynamic input parameters for the three assessed HGs

| **Dynamic parameter** | | **Thin HG** | **Thick/FRP HG** | **Steel HG** |
|---|---|---|---|---|
| Mass | = | 260 kg | 260 kg | 123 kg |
| Stiffness | = | 26,000 N/m | 26,000 N/m | 13,200 N/m |

As mentioned in section 5.4.3 the added hydrodynamic mass is not yet taken into account. This section will first assess the response of the HGs to the hydrodynamic loading without an added hydrodynamic mass. In case that it appears that the mass of the dynamic system has an influence on the susceptibility to galloping-type vibrations, the added mass will be included in the computations.

### 6.3.1. RESPONSE OF THE HGS TO THE HYDRODYNAMIC LOADING

The maximum negative hydrodynamic damping that have been found for the thin HG as well as for the steel HG is approximately 100 Ns/m, whereas the maximum negative hydrodynamic damping found for the FRP HG is equal to 200 Ns/m. The response of the one degree of freedom systems for the undamped situation, and an applied external damper with a damping coefficient of 100 Ns/m and 200 Ns/m respectively is shown in figure 6.18, figure 6.19 and figure 6.20. The response of the thin HG (being 5 cm thick), the thick / FRP HG (being 10 cm thick) and the steel HG are plotted in red, blue and green respectively. For situation in which the vertical velocity of the HG falls beyond limits of the vertical velocities which can be simulated, as explained in section E.4, the plot response is not plotted for the whole simulation time.

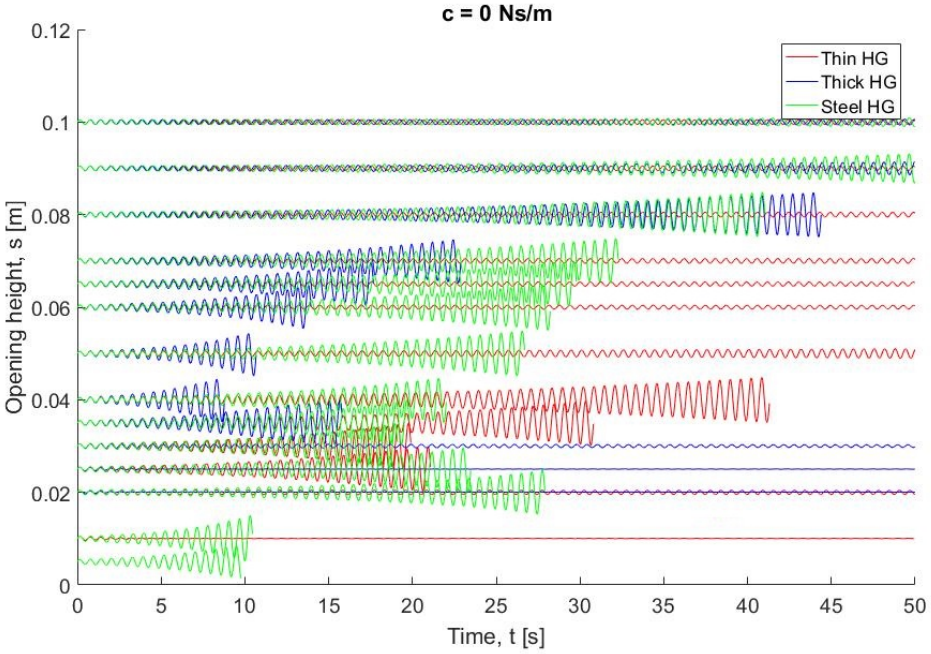


Figure 6.18: Response for c = 0 Ns/m

First of all figure 6.18shows that the thick HG shows an earlier reach of the vibration velocity limits, due to a larger negative damping, than the thin HG or the steel HG. Secondly the starting positions at which instability occurs is different for the three HGs as expected looking at the comparison of the $C_L$-curves for the thick and thin HG in section 5.3.3 in appendix E.

Figure 6.18 shows that the opening height at which the vibration intensity is increased the most are roughly, 4 cm, 2.5 cm and 0.5 cm for the thick/FRP HG, thin HG and steel HG respectively. Based on visual inspection of figure 6.18 the instability regions are shown in table 6.2.

Table 6.2: Instability regions of the three assessed HGs based on visual inspection

| **Thin HG** | **Thick/FRP HG** | **Steel HG** |
|---|---|---|
| $2cm \leq s \leq 6cm$ | $3cm \leq s \leq 9cm$ | $0.5cm \leq s \leq 10cm$ |

As mentioned by Thang and Naudascher [3] the critical critical gap-ratio is equal to 0.65. For the thin HG and thick/FRP HG this would yield a critical opening height of 3.25 cm and 6.5 cm respectively. Although the critical gap-ratio expressed by Thang and Naudascher [3] falls within the boundaries presented in table 6.2, a visual inspection of 6.18 has already shown that the opening height at which the vibration is amplified the most, i.e. the critical opening height, is not the same as the critical opening height using the critical gap-ratio mentioned by Thang and Naudascher [3].

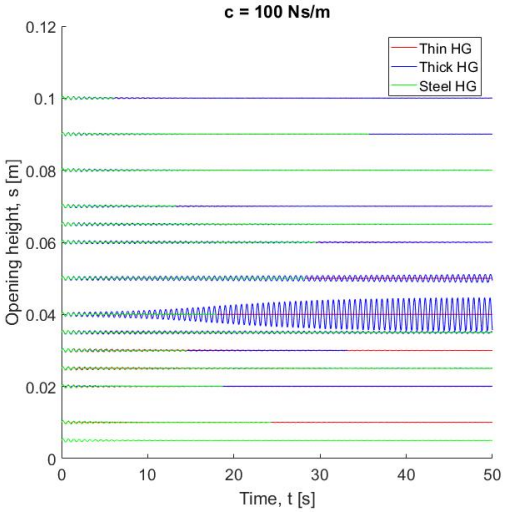


Figure 6.19: Response for c = 100 Ns/m

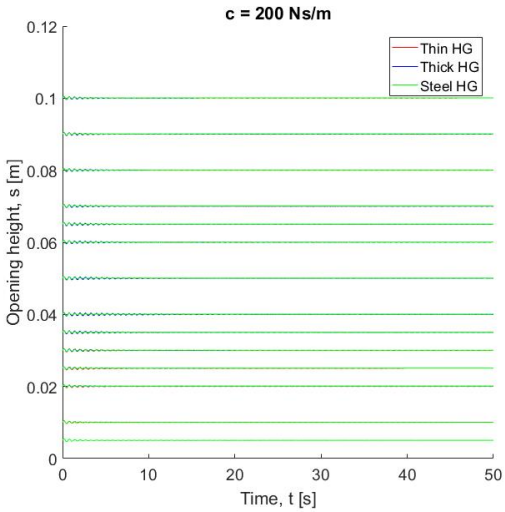


Figure 6.20: Response for c = 200 Ns/m

Figure 6.19 shows that the thin HG and steel HG are completely stable for all opening heights whereas the thick HG has reached an equilibrium vibration amplitude at which the maximum occurring negative hydrodynamic damping is compensated for by means of the external damper with a damping coefficient of 100 Ns/m. More on this matter in section 6.4.4

Figure 6.20 shows that the presence of an external damper with a damping coefficient of 200 Ns/m renders a completely stable system for the thick/FRP HG as well, i.e. the initial disturbance of 0.005 m/s in upward direction is quickly damped out.

As mentioned in section 3.3 the validity of the quasi-static approach is valid for cases in which the reduced velocity is much larger than the displacement number, i.e. $U_r \gg D$. This is usually the case since vibrations with small amplitudes should already be prevented. A check is performed to show that the application of the quasi-steady approach is indeed valid.

$$\frac{T_s U_0}{t} \gg \frac{\xi_0}{h_{gate}} \tag{6.1}$$

| | | | | |
|---|---|---|---|---|
| in which | t | = | Thickness of the HG: | 0.12 [m] |
| | $U_0$ | = | Flow velocity: | 1.5 [m/s] |
| | $T_s$ | = | Timescale of the HG: | 0.6 [s] |
| | $\xi_0$ | = | Vibration amplitude | 0.005 [m] |
| | $h_{gate}$ | = | Height of the HG: | 1.3 [m] |

The maximum used thickness yields the minimum reduced velocity. Therefore, the thickness of the steel HG is governing. The time scale of the system is determined by determining the time between two local maxima in figure 6.18, being approximately 0.6 seconds. The maximum of the vibration amplitudes is approximately 0.5 centimetres. These values yield the requirement: $6 \gg 3.8 * 10^{-4}$, which is true. Therefore, the quasi-static approach is indeed valid.

### 6.3.2. STABILITY PLOTS

It is interesting to compare the required damping for the three HGs for the whole range of opening heights and express it in one figure. Figure 6.21 shows the plots of the required damping based on the computation using the one degree of freedom system (solid line) and the required damping coefficient based on the occurring negative hydrodynamic damping coefficients for a HG at rest (dashed line). Figure 6.21 also includes the required damping coefficient for compensating the maximum occurring negative hydrodynamic damping coefficient (dash-dot line) over the whole range of the vertical velocities of the HG, being $-0.05m/s \leq \frac{dy}{dt} \leq 0.05m/s$. Once again the thin HG, thick/FRP HG and steel HG are plotted in red, blue and green respectively.

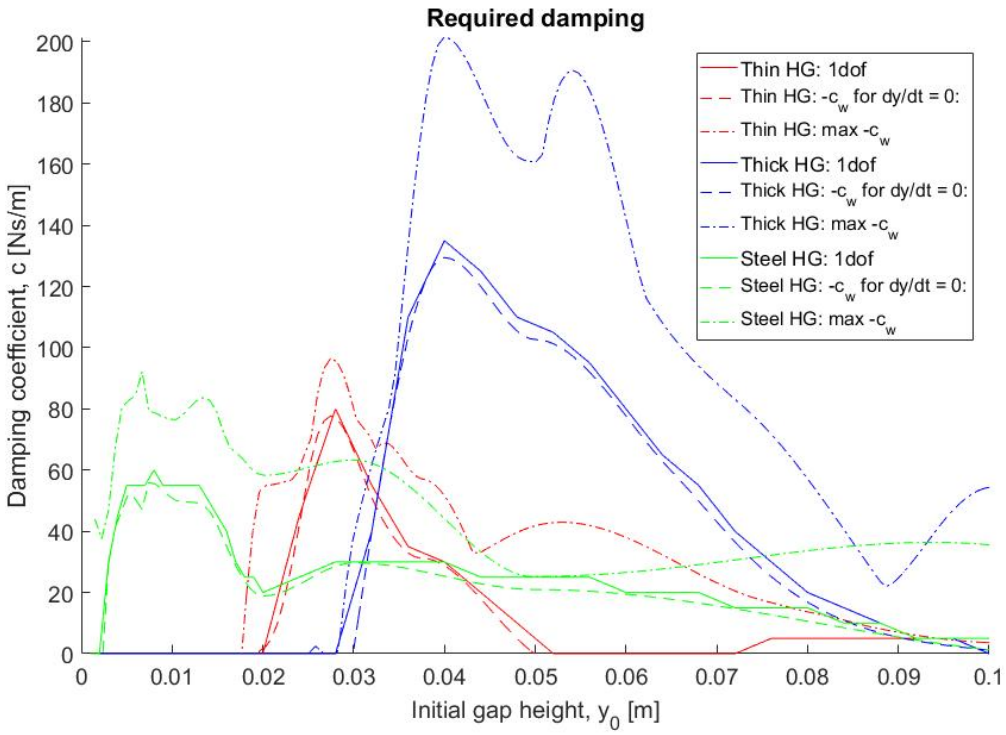


Figure 6.21: Computed required damping coefficients

As expected the required damping to prevent galloping-type vibrations has to be slightly higher than the maximum negative hydrodynamic damping coefficient due to flow. For a HG in rest it can be stated that the steel HG requires an external damper with a damping coefficient of 60 Ns/m. This is much less than the required damping for the FRP HG with the same bending stiffness, which required an external damper with a damping coefficient of 130 Ns/m. Furthermore, the maximal occurring negative hydrodynamic damping coefficient for the

As expected the only dynamic property of the one degree of freedom that is of interest in galloping-type vibrations is the occurring hydrodynamic damping and the applied mechanical damping. The influence of the mass, both the mass of the HG and the added hydrodynamic mass, and the stiffness on the susceptibility to galloping-type vibrations is negligible.

When figure 6.21 is rewritten by dividing the required damping and the initial opening height by the thickness of the HGs figure 6.22 is obtained.

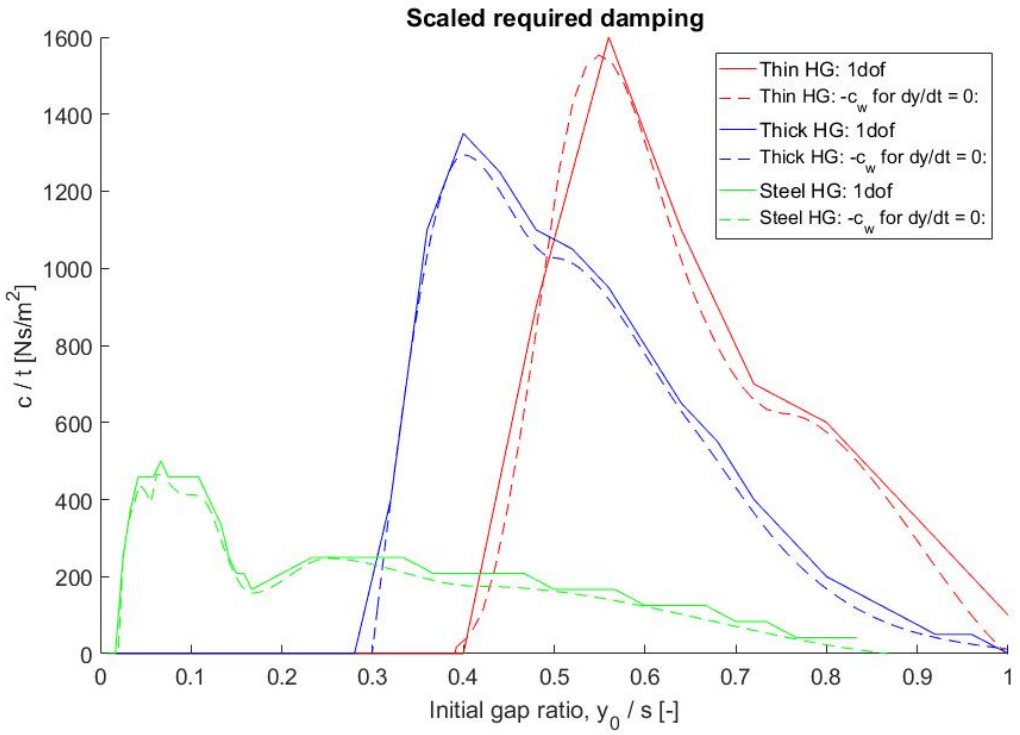


Figure 6.22: Computed required damping coefficients

Furthermore, figure 6.22 shows that the critical opening height for HGs with a rectangular cross-section regarding galloping-type vibrations lies somewhere around 0.4 (as found for the thick HG) and 0.55 (as found for the thin HG). The assessed design of a typical steel HG, i.e. a vertical plate stiffened by ribs, shows a critical gap-ratio range between $0.03 \leq s_{critical} \leq 0.1$. More on this subject in section 6.4.4.

## 6.4. CONCLUSIONS

General conclusions are drawn in section 6.4.1. Based on differences between a thick and a thin HG conclusions are drawn in section 6.4.2 and differences based on a different HG design in section 6.4.3. A comparison between results from this thesis and results obtained by Thang and Naudascher [3] is elaborated in section 6.4.4.

### 6.4.1. GENERAL CONCLUSIONS

For the susceptibility to galloping-type vibrations the only important part of the hydrodynamic forces acting on the HG is the hydrodynamic damping. As long as a mechanical damper is applied with a damping coefficient larger than the possibly occurring negative hydrodynamic damping coefficients for the range of required opening heights and range of accompanying vertical velocities of the HG during the opening and closing procedure.

HGs are susceptible to galloping-type vibrations for the combination of ranges of the opening height and vertical velocities at which the negative hydrodynamic damping is larger than the applied mechanical damping.

### 6.4.2. CONCERNING THE DIFFERENCES BETWEEN A THIN AND A THICK HG:

- A thick HG results in larger upward forces than a thin HG;
- The occurring negative hydrodynamic damping coefficient scales with the thickness of the HG, i.e. increasing the thickness by a factor two results in an increase of the maximum negative hydrodynamic damping with a factor two. Therefore, the external damping that is required to avoid galloping-type self-excitation also scales with an increasing thickness.

- As for the value of the occurring negative hydrodynamic damping the range of opening heights at which negative hydrodynamic damping occurs also scales with the thickness.
- A thick HG has larger positive hydrodynamic stiffness and smaller negative hydrodynamic stiffness than a thin HG, although this does not influence the stability to galloping-type vibrations since the maximum negative hydrodynamic stiffness is much smaller than the mechanical stiffness of the suspension;
-

### 6.4.3. CONCERNING THE DIFFERENCES BETWEEN AN FRP PLATE HG AND A STEEL HG CONSISTING OF A PLATE AND STIFFENERS:

- A FRP HG has a smaller range of opening heights and vertical velocities of the HG in which negative hydrodynamic damping occurs than a steel HG consisting of a plate stiffened by ribs;
- The FRP HG is subjected to larger negative hydrodynamic damping than a steel. The maximum occurring negative hydrodynamic damping computed for the FRP HG is found to be twice as high as the maximum occurring hydrodynamic damping of the steel HG. Therefore much more damping is required to avoid galloping-type vibrations for an FRP HG than for a steel HG;
- A smaller negative stiffness occurs for a thicker gate. This becomes important for cases in which the negative hydrodynamic stiffness is not negligible compared to the mechanical stiffness of the dynamic system. In this research the negative hydrodynamic stiffness appeared to be much smaller than the structural stiffness. Therefore, the negative hydrodynamic stiffness did not influence the susceptibility to galloping-type vibrations.

### 6.4.4. COMPARISON OF RESULTS OBTAINED BY THANG AND NAUDASCHER [3] AND RESULTS OBTAINED IN THIS RESEARCH

The plot at the bottom of figure 3.14 concerns $A_1$, which is an indicator of the present hydrodynamic damping for a HG in a fixed position, as a function of the gap-ratio.

Thang and Naudascher [3] mentions that the critical gap ratio is equal to 0.65. Interestingly the maximum value of $A_1$ is not found to be at a gap-ratio of 0.65 but for a gap-ratio of 0.5

The equilibrium vibration amplitude found in figure 6.19 agrees well with results obtained by Thang and Naudascher [3] as presented in figure 6.23 in which "a" indicates that the vibrations started for the HG in rest (not moving).

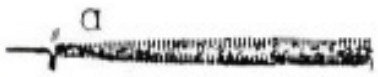


Figure 6.23: Records of vibrations shown in Thang and Naudascher [3]

Among other conclusions the following conclusions are drawn by Thang and Naudascher [3] and mentioned in section 3.5.2:

1. The gate was stable for negative slopes of $C_L$ as a function of $(s/d)$ or negative values of $A_1$ both in rest as with large trigger amplitudes;
2. A positive slope for $C_L$ as a function of $(s/d)$ can be used as an instability indicator;.

Based on results obtained in this chapter it can be stated that conclusion 1 is indeed true. The slope of the $C_L$-curve is a measure of the hydrodynamic stiffness. The maximum negative hydrodynamic stiffness found in the assessment of the three HGs in this chapter is approximately 500 N/m, which is small compared to the minimal used stiffness of the suspension of 13,200 N/m. Therefore the stiffness does not influence the stability of the HGs as much as stated in conclusion 2. The $C_L$-curve as a function of the gap ratio, being s/d, is useful as an indicator of the presence of negative hydrodynamic damping since they are related, as shown in figure 3.14 in which the top figure concerns the hydrodynamic stiffness and the bottom figure is related to the hydrodynamic damping.

# 7

# DISCUSSION

First of all the different methods that are applicable in predicting flow-induced vibrations are discussed in section 7.1. The used models in this thesis are discussed in section 7.2. Section 7.3 discusses the validation of the CFD model that is used in this research. In section 7.4 the used method for computing the response of the dynamic system using the Krylov-Bogoliubov method of averaging is discussed.

## 7.1. METHODS TO PREDICT FLOW-INDUCED VIBRATIONS OF HGS

CFD computations offer a means to determine the susceptibility to flow-induced vibrations. Results using the method used in this research show that it is possible for engineering companies with employees experienced in using CFD to predict the susceptibility to galloping-type vibrations in the design. On the other hand CFD models are not yet sophisticated enough. Therefore, a validation step is still required to prove that CFD results are really valid. Companies experienced in performing hydraulic experiments, such as Deltares, can provide the necessary validation step of the research. Further elaboration of the applicability of CFD and the simulation of vibrations using a one degree of freedom system are presented in section 8.2.

It is also possible to apply a fully coupled model between the fluid dynamics, simulated in CFD, and the dynamics of the HG in a Fluid-Structure Interaction (FSI) model. This coupled model is primarily important when the neither the speed of the fluid dynamics nor the speed of the solid dynamics can be neglected. For this research the more computationally expensive fully coupled FSI model is not required.

Experiments also offer a means to predict flow-induced vibrations. Experiments can become quite expensive an can only be performed by specialised companies, such as Deltares, that have the required knowledge and necessary facilities such as flumes to perform these experiments.

Finally it is expected that flow-induced vibrations are difficult to predict using analytical computations due to the large complexity of the flow and accompanying forces acting on the HG, as seen in the force plots of chapter 6.

## 7.2. MODELS USED IN THIS THESIS

The dynamic system used in this research, being a one degree of freedom system, is discussed in section 7.2.1. The used CFD model is discussed in section 7.2.2.

### 7.2.1. SCHEMATISATION OF THE STRUCTURE INTO A DYNAMIC SYSTEM

The one degree of freedom system is a well known dynamic model in which the dynamic properties of a system is discretised in a mass, stiffness and damping. HGs with a vertical degree of freedom are suspended by cables and stabilised by external dampers. The weight of the cables and dampers is negligible to the weight of the HG, the suspension stiffness is negligible to the bending stiffness of the HG in vertical direction and the damping in the system comes from the external dampers. Therefore, the dynamic system for vertical vibrations can be modelled as a one degree of freedom system. The simplification of the system into a one degree of freedom system is supported by Erdbrink [7]: "...the assumption of a rigid body with a massspring suspension is a very reasonable and generalisable analogy for true structural flow-induced responses, while many simplifying assumptions for the modelling of the fluid flow are disastrous for capturing the flow field and therefore the flow load on the structure." The advantages and disadvantages of a one degree of freedom are the following:

+ The simplification into a one degree of freedom system has a well known solution to its equation of motion, which makes it easy to find the response of the system to the external loading;

+ Since the natural frequencies of HGs generally are higher than vibration of excitation sources one is primarily interested in the first natural frequency of the system, which can be determined by modelling the dynamic system as a one degree of freedom system;

- When natural frequencies of a structure higher than the first natural frequency, e.g. fundamental frequency, are of interest the one degree of freedom system is not applicable and other more sophisticated models are required;

- The model is not applicable when the loading and the dynamic properties in terms of mass, damping and stiffness cannot be discretised in one point, then a multiple degree of freedom system or continuous system is required;

If the dynamic properties and loading can be discretised in a number of points instead of only one, a multiple degree of freedom system may be applied. This system has a number of natural frequencies equal to the degrees of freedom. The advantage of a multiple degree of freedom system with respect to the one degree of freedom system is that higher natural frequencies and accompanying mode shapes can be determined

For systems in which the dynamic properties are continuously distributed, i.e. it has an infinite number of degrees of freedom, and/or the force is location-dependent, the continuous model can be used. An example of theory which describes continuous systems is the Timoshenko beam theory. Simple continuous systems can be solved relatively easily by hand calculations. More complicated structure geometries and / or orthotropic material properties can be assessed using Finite Element method software. The latter is especially interesting for FRPs with layers in different fibre directions when the HG is loaded in bending, shear or normal force. In this research vertical gate vibrations are assessed for a situation in which the use of a one degree of freedom system suffices. Therefore, FEM simulations are not required for the research elaborated in chapter 6. General advantages and disadvantages of the use of FEM when compared to the one degree of freedom system are:

+ Complicated structure geometries can be assessed;

+ The influence of orthotropic material properties can be taken into account;

+ Higher natural frequencies and accompanying vibration modes can be computed;

- Computationally expensive;

### 7.2.2. USE OF DIFFERENT CFD MODELS

The used CFD model in this thesis takes the quasi-static approach as a starting point. For the quasi-static approach to be valid the dynamics of the HG has to be slow compared to the fluid dynamics, i.e. the HG moves slow enough for the water flow to adjust to the change in position of the structure. Computations performed in this thesis show that the quasi-static approach is valid. The advantages and disadvantages of a CFD model that does not take a moving HG into account compared to one that does are the following:

+ A moving HG is not required for cases in which the quasi-static approach is valid;

+ A moving HG would require re-meshing in between time steps which makes simulations more computationally expensive and unstable;

+ Not including a moving gate makes it easier to determine whether or not the simulation is converged and a steady state situation is achieved;

- The quasi-static approach is not valid for cases in which the dynamics of the HG is not negligible compared to the fluid dynamics;

- The sudden stiffness cannot be derived from the resulting force matrix for different opening heights and vertical velocities since a moving HG is required for this.

The research performed in this thesis concerns a simplified two-dimensional model. This model is valid for situations in which the geometry of the structure and geometry of the fluid-domain does not vary in the third dimension, i.e. the cross section of the model is constant in the third dimension. The advantage and disadvantages of a two-dimensional CFD model compared to a three-dimensional CFD model are the following:

+ The number of grid cells is much lower than in a three-dimensional CFD model, i.e. the computational time required to perform the simulation is a lot less;

- Disturbances can only spread out in x- and y-direction instead of the z-direction as well. This means that recirculation zones and the influence of the boundary conditions are present for a longer distance than for a more computationally demanding three-dimensional model;

- Turbulence intensity is underestimated for a two-dimensional model, since the turbulence intensity in z-direction is absent (also stated by Erdbrink [7]);

- A three-dimensional model can take the static deformations into account, being variable over the width of the HG due to the influence of the supports;

The CFD model included the use of the Volume of Fluid (VOF) method in which not only water but also the presence of air is included. It is also possible to perform computations in which only one phase, being water, is present in the model. In a model that contains only water instead of water and air the water level is modelled as a so-called "rigid lid", which means that it has a fixed position. The advantages of the VOF method when comparing it to a method which only takes water into account are the following:

+ Using the VOF method changes in the water level can be simulated accurately. This means that the pressure distribution at the HG's underside can be modelled more accurate;

+ The water level and pressure distribution at the HG's underside can be simulated more accurate using the VOF method. Therefore, these two aspects are of great importance in the computation of the lift-coefficient and validation part of the CFD model in chapter 5.

In this research CFD simulations have been computed using a transient solver. A steady-state solver is also available but has a few drawbacks. At Deltares the comparison between these two solvers is made and only transient solvers are used since. The following advantages of a transient solver compared to a steady-state solver are the following:

+ A transient solver is much more stable;

+ The initial condition is not necessarily close to the final solution. Therefore, the water levels change during the CFD simulation. A transient solver can, when including the VOF method, take the changing water levels into account while steady-state solver is unable to do this;

+ Experience at Deltares shows that the transient solver is less computationally expensive.

## 7.3. PARTIAL VALIDATION OF THE CFD MODEL

The CFD model that is used in this research is partially validated by comparing results from Thang and Naudascher [3] to results found in this thesis. Comparison of results of the CFD model that is used in this thesis to results obtained by Thang and Naudascher [3] has given some trust in the outcome of the CFD model. It is only a partial validation since not all experimental data has been documented. For instance experimental parameters such as the water levels were not mentioned in Thang and Naudascher [3] but have been derived in this thesis based on the given Reynolds number. Also the positions at which water levels were measured were not clearly mentioned in Thang and Naudascher [3]. The partial validation has been performed for a HG of five centimetres thick and a water level difference of 1.1 centimetre. The water level difference of the final CFD model that has been used in chapter 6 is increased up to ten centimetres in order to simulate vertical velocities of the HG up to five centimetres per second. This has to do with the linear scaling of the vertical velocity of the HG with the flow velocity of the water as mentioned in section 3.5.2. Also a HG with a thickness of ten centimetres and a HG with a typical design (for a steel HG) have been modelled in CFD. The increased water level difference and different HG designs have not been validated using experimental data. Recommendations regarding further validation of the CFD model is elaborated in section 8.3

## 7.4. KRYLOV-BOGLIUBOV METHOD OF AVERAGING

In this research the Krylov-Bogoliubov method of averaging is used to solve the differential equation presented in the equation of motion (equation 5.1. Other methods such as the forward Euler method can also be used to solve this equation of motion. This method has been applied during this research but required much smaller time steps in order to obtain a stable solution, when comparing it to the method using the Krylov-Bogoliubov method of averaging. The well-known solution to an undamped natural vibration, i.e. both the damping and the right hand side of equation 5.1 are equal to zero, is compared to results found by computations using the Krylov-Bogoliubov method of averaging and the forward Euler method. The forward Euler method required time steps as small as $10^{-}4$ seconds whereas the Krylov-Bogoliubov method of averaging was already stable for time steps of $10^{-}2$ seconds. Therefore, the Krylov-Bogoliubov method of averaging is further used in this research.

# 8

# CONCLUSIONS AND RECOMMENDATIONS

This chapter is dedicated to conclusions drawn in this thesis regarding the research questions, in section 8.1. The practical applicability of the approach used in this thesis is discussed in section 8.2. Recommendations are stated in section 8.3 and concern further validation and verification of the CFD model, design recommendations when designing an FRP HG and possible further research in the field of flow-induced vibrations and the influence of FRP on this matter.

## 8.1. CONCLUSIONS

First of all the answer to the research question is given after which the sub-questions are addressed.

**Research question:** What influence does the choice for Fibre-Reinforced Polymer (FRPs) have on the occurrence of flow-induced galloping-type vibrations of hydraulic gates (HGs) with underflow?

The use of FRP as a building material for HGs has a negative influence on the stability regarding galloping-type vibrations. FRP HGs experience larger negative hydrodynamic damping than steel HGs. Therefore, they are more susceptible to galloping-type vibrations than steel HGs and require more mechanical damping to prevent galloping-type vibrations. This is explained in the two paragraphs below.

First of all, steel has a higher Young's modulus than FRPs, i.e. steel has a higher stiffness. This lower stiffness results in a larger required thickness of an FRP HG than for a steel HG. This increase of the thickness has a large impact on the hydrodynamic (upward) force acting on the HG and results in higher negative hydrodynamic damping occurring in a larger range of opening height. The range of opening heights at which negative hydrodynamic damping occurs and the magnitude of this negative hydrodynamic damping is scaled with the thickness of the HG. In other words it means that increasing the thickness with a certain percentage increases the range at which negative hydrodynamic damping occurs and the magnitude of this negative hydrodynamic damping with the same percentage. Consequently an increase of the thickness results in more required mechanical damping to compensate for the larger negative hydrodynamic damping or require an adjusted shape of the HG's underside to prevent galloping-type vibrations. One of the possible solutions is a bevelling of the HG's underside. Design recommendations for preventing galloping-type vibrations are elaborated further in section 8.3.3

Secondly, HGs made of FRP will most likely not have the same design as steel HGs. HGs made of steel usually come in the form of a plate stiffened by ribs. Structures made of FRP quite often come in the form of a sandwich panel or other forms in which the flanges consist of FRP laminates and the centre is either empty or filled with a filling material in order to improve the effectiveness of the material. When comparing an FRP laminate HG to a typical steel HG (with the same bending stiffness) the FRP HG, being slightly thinner than the steel HG (10 cm for the FRP HG and 12 cm for the steel HG), has a smaller range of opening heights and accompanying vertical HG velocities in which negative hydrodynamic damping occurs, albeit with a much higher negative hydrodynamic damping coefficient. Therefore, in general it be stated that the FRP HG is more susceptible to galloping-type vibrations than a typical steel HG and requires more mechanical damping than a typical steel HG.

### 8.1.1. RESEARCH QUESTIONS

In this section the sub-questions of this research are addressed.

**Sub-question 1:** What does the choice of FRP mean for the dynamic properties of a plate loaded in bending?

In general it can be stated that the use of solid FRP laminates in HGs results in lighter structures when compared to a solid steel HG. Using sandwich panels will further increase the efficiency of FRP while increasing the thickness and decreasing the specific density.

In the past HGs were primarily designed for strength rather than deformation requirements as the stiffness has not been the issue. FRPs have high strength but medium to low stiffness. When comparing a steel plate loaded in bending with an Glass Fibre-Reinforced Polymer (GFRP) and Carbon Fibre-Reinforced Polymer (CFRP) plate, with fibre alignment in span direction, having the same bending moment capacity as the steel plate a much lower natural frequency in dry and submerged condition is found. As mentioned by Kolkman and Jongeling [2] a lower natural frequency in general increases the susceptibility to flow-induced vibrations since excitation frequencies generally are lower than vibration frequencies of HGs.

When the Glass-Fibre Reinforced Polymer (GFRP) and Carbon-Fibre Reinforced Polymer (CFRP) plate are dimensioned in such a way that they have the same bending stiffness as the steel plate their thickness is larger than for the plates dimensioned on the same bending strength as the steel plate. Their natural frequency in dry condition is higher than the steel plate but in submerged condition the natural frequencies will be roughly the same as the steel plate, meaning that regarding their natural frequency they are equally susceptible to flow-induced vibrations.

When taking into account that FRPs are usually built up from layers with fibres in different directions, the required thickness increases which increases the natural frequency both in dry and submerged conditions. This is favourable but will not compensate for the plates which have the same bending moment capacity as a steel plate. Since FRP HGs are now also designed for stiffness requirements instead of only a bending moment capacity they have approximately the same bending vibrations frequency, making them equally susceptible to flow-induced vibrations.

**Sub-question 2:** How can the dynamic behaviour of a HG with underflow be predicted?

Vibrations of HGs with a vertical degree of freedom can be simulated as a dynamic one degree of freedom system in which the HG with a certain mass is suspended by a suspension with a certain stiffness and stabilised using a certain damper. The external force is the upward force felt on the bottom of the HG which for steady flow conditions is a function of the position and vertical velocity of the HG, as described in section 5.1.

The upward force acting on the bottom of the HG for different combinations of the vertical position and accompanying vertical velocity of the HG can be determined using CFD software. This can be done in a quasi-static manner as described in section 3.5.2, elaborated further in chapter 5 and applied in chapter 6. Using the quasi-static manner certain ranges of the vertical position and vertical velocity of the HG can be simulated. The advantage of the quasi-static method is that the presence of a moving structure is not required, since the moving structure is modelled in a static manner, decreasing the computational costs.

The HG is positioned at certain initial opening heights, especially those below a gap ratio (gap ratio = opening height / thickness of the HG) of one at which the largest negative hydrodynamic damping occurs, and given a certain initial disturbance, being an initial velocity. The response of the dynamic system can be simulated using a time-loop in software such as MATLAB. A dynamic system is stable regarding flow-induced galloping-type vibrations when the following two rules apply:

1. The mechanical stiffness of the dynamic system, being the suspension stiffness, is much larger than the possibly occurring negative hydrodynamic stiffness;

2. The applied mechanical damper has a larger damping capacity than the possibly occurring negative hydrodynamic damping.

**Sub-question 3:** What is the influence of the vertically moving structure on the flow-induced loading?

The vertically moving structure influences the incidence angle of the flow velocity. This translates to a different flow separation and possible reattachment and accompanying pressure distribution at the underside of the HG. Depending on the accompanying position of the HG underside a vertical velocity of the HG may result in an increase or decrease of the upward force and therefore a damping or an amplification of the vibration respectively. An amplification of the movement, due to self-excitation occurs for instance in the case where a downward moving HG (negative velocity) results a decrease of the upward force, resulting in an amplification of movement.

**Sub-question 4:** Which added terms can be computed using transient CFD computations?

The force matrix resulting from CFD computations shows the dependency of the vertical force on the vertical position and vertical velocity. This research has proven to be successful in deriving the added hydrodynamic stiffness and damping from this matrix. Stiffness and damping are basically the derivative of the force over the vertical position and derivative of the force over the vertical velocity respectively. Therefore, the stiffness due to buoyancy, stiffness due to flow and damping due to water flow can be determined using transient CFD computations and are therefore included in the force mtrix.

## 8.2. PRACTICAL APPLICABILITY OF THE METHOD USED IN THIS THESIS

The use of CFD models in combination with the quasi-static aeroelasticity approach is capable to predict the susceptibility to galloping-type vibrations. Hydrodynamic damping coefficients can be determined based on CFD computations. Based on hydrodynamic damping plots as a function of the opening height and accompanying vertical velocity of the HG in combination with the desired opening and closing velocity of the HG, the occurring hydrodynamic damping as a function of time can be determined. These plots may also provide insight in the ideal opening and closing velocity of the HG. Also in case of partially opening of the HG, such as for drainage sluices, opening heights at which the HG should not be placed can be predicted.

Further elaborating the upward force in one degree of freedom system, as performed in this research, can be used to determine if the HG will hit the obstruction beneath the HG, such as a concrete floor or a sill, when galloping-type vibrations occur.

Also force plots as a function of the opening height and accompanying vertical velocity of the HG in combination with the opening and closing velocity of the HG can be used to determine the required lifting force as a function of time.

## 8.3. RECOMMENDATIONS

The following recommendations are given regarding ways to further validate the CFD results in this research, compare results with other CFD models, design recommendations and possible further research when designing a HG made of FRP.

### 8.3.1. VALIDATION OF THE CFD COMPUTATIONS

The CFD computations performed in this thesis can be validated by conducting physical experiments in a flume. Upward forces found by performing these physical experiments could then be compared to the force matrices found in chapter 6. Also the response of the HG to an initial disturbance can be performed in the flume and compared to the response of the dynamic system as performed in section 6.3, including the influence of the added hydrodynamic mass.

### 8.3.2. VERIFICATION OF THE CFD COMPUTATIONS

It is interesting to compare the resulting force matrices to a CFD model which includes a moving HG. Comparing the resulting force matrix for different opening heights and velocities of the transient CFD computations to results for CFD computations with a moving HG. Based on the comparison between results from CFD computations for a static HG (in this thesis) and CFD computations including a moving HG, one could say something about the necessity of adding a moving HG in the computations. It is expected that since the quasi-static approach is valid for the CFD computations conducted in this research a moving gate is not required. Also the difference in the required computational time can be checked, which is unknown at this moment.

Also it is recommended to compare the resulting force matrices using the two-dimensional CFD model to a three-dimensional CFD model. A three-dimensional CFD model is more accurate than a two-dimensional CFD model due to the lack of turbulence in the third dimension. Also the influence of boundary conditions is smaller for three-dimensional models since disturbances can spread out in the third dimension.

### 8.3.3. DESIGN RECOMMENDATIONS

It is expected that regular countermeasures for avoiding self-excitation of HGs with a vertical degree of freedom, as mentioned by Kolkman and Jongeling [2], will also apply to FRP HGs. These countermeasures include but are not limited to applying a downstream bevelling (inclination) of the HG's underside of the HG up to an angle of 60°. Thang and Naudascher [3] have researched the influence of an upstream bevelling of the underside of the HG. Their research has shown that if the HG's underside is inclined under an angle of 45° a completely stable HG is achieved. Erdbrink [7] has shown that a ventilated HG with a horizontal underside also results in a more stable solution. This solution is also applicable to FRP HG's.

FRP is a material which offers a large design freedom. Therefore, it is recommended to research if adaptations of a FRP design, other than those described above, may decrease the susceptibility to flow-induced vibrations.

### 8.3.4. POSSIBLE FURTHER RESEARCH

The method used in this thesis as described by Thang and Naudascher [3] may also be applied to HGs other than vertical lift gates. It is recommended to try this method on other HGs with underflow such as sector gates and Tainter-gates.

It is recommended to compare results found in this research regarding galloping-type vibrations to the assessment of the HGs using Kolkman and Jongeling [2]. By doing this it can be checked whether or not the instability can also be predicted using Kolkman and Jongeling [2].

The HGs assesed using CFD in chapter 6 did not include the static deformations of the HG due to the water level difference. It is recommended to include the static deformation when performing CFD computation to determine the susceptibility to galloping-type vibrations.

As the use of FRP in HGs will require more attention to combat galloping-type vibrations than steel HGs it is recommended to research the influence of these design adjustments in terms of dimensions, weight, costs etcetera.

In this thesis only limited time is spent on the influence of the presence of (flowing) water on the properties of the dynamic system in terms of an added mass, added hydrodynamic damping and hydrodynamic stiffness. Kolkman and Jongeling [2] provides means to determine the added mass for certain limit cases but not for situations which ly in between these limit cases. The added mass does not influence the susceptibility galloping-type vibrations although it does influence the natural frequency of the dynamic system which has an impact on flow-induced vibrations due to turbulence and vortex shedding. Therefore, it is recommended that more research is performed regarding the influence of the thickness of a HG and opening heights on the added mass.

This research has been focussed on vertical vibrations. It is recommended to research the influence of the use of FRPs on (horizontal) bending-type vibrations, including the influence of added mass.

# List of Figures

# List of Tables

# BIBLIOGRAPHY


[1] B. Edmondson, *Collision Resistance of Fibre Reinforced Poly- mer Lock Gates,* .

[2] P. A. Kolkman and T. H. G. Jongeling, *Dynamic behaviour of hydraulic structures. Part A: Structures in flowing fluid* (2007).

[3] N. D. Thang and E. Naudascher, *Self-excited vibrations of vertical-lift gates,* Journal of Hydraulic Research **24**, 391 (1986).

[4] A. Korevaar, *Vertical Flow-Induced Vibrations of Valves in Navigation Locks*, Master thesis, Delft University of Technology (2016).

[5] H. M. Westergaard, *Water pressures on dams during earthquakes,* (1933).

[6] O. C. Tieleman, *The dynamic behaviour of pump gates in the Afsluitdijk*, Master thesis, Delft University of Technology (2015).

[7] C. D. Erdbrink, *Modelling flow-induced vibrations of gates in hydraulic structures*, Ph.D. thesis, Universiteit van Amsterdam (2014).

[8] K. Anami, N. Ishii, C. W. Knisely, and T. Oku, *Hydrodynamic Pressure Load on Folsom Dam Tainter-Gate at Onset of Failure Due to Flow-Induced Vibrations,* in *ASME 2005 Pressure Vessels and Piping Conference* (2005) pp. 557–564.

[9] Unknown, *Folsom Dam (California, 1995) | Case Study | ASDSO Lessons Learned,* .

[10] R. W. V. Straten, *Feasibility study on fibre reinforced polymer slides in the Eastern Scheldt storm surge barrier*, Master thesis, Delft University of Technology (2013).

[11] J. J. W. M. Veraart, *Glasvezelversterkte kunststof schuiven als alternatief voor de schuiven in de Oosterscheldekering*, Master thesis (1998).

[12] E. A. Ross, *Flow-induced dynamic behaviour of fibre reinforced polymer hydraulic gates*, Master thesis, University of Southern Denmark (2013).

[13] *Renovatie stuwensemble Nederrijn en Lek,* .

[14] P. V. Vijay, P. R. Soti, H. V. S. GangaRao, R. G. Lampo, and J. D. Clarkson, *Design and evaluation of an integrated FRP composite wicket gate,* Composite Structures **145**, 149 (2016).

[15] N. Ishii and E. Naudascher, *A design criterion for dynamic stability of Tainter gates,* Journal of Fluids and Structures **6**, 67 (1992).

[16] P. A. Kolkman, *Flow induced gate vibrations Kolkman*, Ph.D. thesis, Technische Hogeschool Delft (1976).

[17] J. P. den Hartog, *Mechanical Vibrations* (Dover Publications, Inc., New York, 1956).

[18] M. Kolstein, *Fiber reinforced polymer structures* (2008).

[19] I. C. P. Gómez, *Dynamic Behaviour of Large Hydraulic Structures in FRP: Literature study*, Master thesis, Delft University of Technology (2014).

[20] F. P. van der Meer and M. Pavlovic, *Lecture slides TU-Delft: Fiber Reinforced Polymer structures (CIE5128)* (2016).

[21] T. Tomiyama and I. Nishizaki, *Applicability of fiber reinforced plastics to hydraulic gates,* in *Third International Conference on FRP Composites in Civil Engineering* (2006) pp. 453–456.

[22] G. Marsh, *Reinforced plastics prevail on the waterfront,* Reinforced Plastics (2002).

[23] S. L. Donaldson and D. B. Miracle, *ASM Handbook: Composites*, Vol. 21 (2001) p. 3470.

[24] A. Zorgdrager, *Feasibility study on the application of fiber- reinforced polymers in large lock gates*, Master thesis, Delft University of Technology (2014).

[25] L. Kok, *Feasibility study for FRP in large hydraulic structures 21 January 2013*, Master thesis, Delft University of Technology (2013).

[26] I. C. P. Gómez, *Dynamic Behaviour of Large Hydraulic Structures in FRP: Thesis*, Master thesis, Delft University of Technology (2014).

[27] H. Tuin, *New Canalization of the Nederrijn and*, Master thesis, Delft University of Technology (2013).

[28] M. Versluis, *Hydrodynamic pressures on large lock structures*, Master thesis, Delft University of Technology (2010).

[29] R. R. Craig Jr. and A. J. Kurdila, *Fundamentals of Structural Dynamics*, 2nd ed. (JOHN WILEY & SONS, INC., 2006) p. 744.

[30] J. M. J. Spijkers, E. C. Klaver, and A. W. C. M. Vrouwenvelder, *Dynamics of Structures – CT 4140: Vibrations of Structures*.

# A

# BACKGROUND STRUCTURAL DYNAMICS

## A.1. MULTI MASS-SPRING-DAMPER SYSTEM

In order to perform the dynamical assessment of a structure, dynamic situations can often be simplified to a multi mass-spring-damper system in which rigid bodies with a certain mass have a number of degrees of freedom. The degrees of freedom are displacements of the structure which are not fixed, i.e. admissible displacements such as the translation or a rotation of (a part of) a structure. These vibrations are also called rigid body vibrations. Figure A.1 shows an example of a signpost with three degrees of freedom.

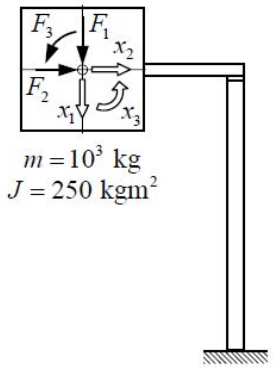


Figure A.1: A system with three degrees of freedom [30]

| | | | | |
|---|---|---|---|---|
| In which: | $x_i$ | = | The three degrees of freedom with i being, 1, 2 or 3 | [m] and [°] |
| | $F_i$ | = | Force in direction of the three degrees of freedom | [N] and [Nm] |
| | m | = | Mass of the system | [kg] |
| | J | = | Mass moment of inertia | [$kgm^2$] |

According to Erdbrink [7] the simplifying assumption of rigid body vibrations is justified in certain situations since it allows for the flow to be modelled more accurately:

> " Although putting a detailed geometry of the barrier in a computer model is doable (albeit timeconsuming), the modelling goal in chapters 3-6 is not to look at the structural response side in detail (i.e. by including trusses or beams and computing all stresses, etcetera). This is because the assumption of a rigid body with a massspring suspension is a very reasonable and generalisable analogy for true structural flow-induced responses, while many simplifying assumptions for the modelling of the fluid flow are disastrous for capturing the flow field and therefore the flow load on the structure."

When a situation is observed in which the system has only got one degree of freedom, such as a admissible translation in the vertical direction, the system can be schematised as a mass connected to a roller, spring and dashpot, as shown in figure A.2.

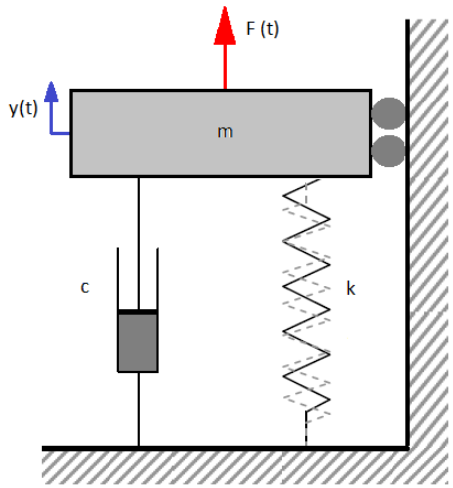


Figure A.2: Model of a mass-spring-damper system

This schematisation yields the equation of motion as shown in equation A.1. This equation consists of four terms, all with the dimension of a force.

$$m\frac{d^2y}{dt^2} + c\frac{dy}{dt} + ky = F(t) \tag{A.1}$$

| | | | | |
|---|---|---|---|---|
| In which: | y | = | Displacement | [m] |
| | t | = | Time | [s] |
| | m | = | Mass of the system | [kg] |
| | c | = | Damping coefficient of the system | [Ns/m] |
| | k | = | Stiffness of the system | [N/m] |
| | F(t) | = | Time dependent force acting on the system | [N] |

In case of an undamped one degree of freedom system, i.e. c=0 kgs, in absence of a load, i.e. F(t)=0 [N], the equation of motion is reduced to: $md^2y/dt^2 + ky = 0$ with the following harmonic vibration as a result: $y = Ysin(\omega_n t)$ In which Y represents an unknown integration constant, being the amplitude of vibration, and the natural angular velocity, is denoted as $\omega_n$. The natural angular frequency and natural frequency at which the system will vibrate (in Hz) are computed as shown in equation A.2.

$$\omega_n = \sqrt{\frac{k}{m}} f_n = \frac{\omega_n}{2\pi} = \frac{1}{2\pi}\sqrt{\frac{k}{m}} \tag{A.2}$$

In which the natural angular frequency has the dimension of rad/s and the natural frequency has the dimension of Hz (or 1/s). The second formula shows that the natural frequency of the vibrating structure will increase with an increase in stiffness and/or a decrease in mass.

The mass and stiffness in the equation of motion result in the conservation of energy due to the fact that the kinetic energy of the mass is transformed into potential energy as stored in the spring and vice versa. Damping results in a dissipation of energy in the system. In general a system can be damped in three different ways, being: under damped, critically damped and over damped. In practice the system is almost always under-damped.

Without damping a structure would keep on vibrating due to the conservation of energy in the kinematic and potential energy. The conservation of energy is written in equation A.3.

$$E_{tot} = E_{kin} + E_{pot} = \frac{1}{2}m(\frac{dy}{dt})^2 + \frac{1}{2}ky^2 = constant \tag{A.3}$$

In which the kinetic and potential energy are denoted as $E_{kin}$ and $E_{pot}$ respectively. Using the conservation of energy on free vibration, i.e. without applied force, it is noted that the total energy of the system is equal to: $\frac{1}{2}ky_{max}^2$ in which $y_{max}$ is the maximum vibration amplitude. This is true since the maximum potential energy occurs at the point in time where the kinetic energy is zero, i.e. the maximum deflection occurs at the point in time when the velocity is zero. Both the mass and spring stiffness have positive values and they are multiplied with the squared time derivative of the displacement and squared displacement respectively, values of both the kinetic and potential energy range between zero and the maximum.

Dissipation of energy over time due to damping can be formulated as shown in equation A.4.

$$\Delta D = \int_{t=0}^{t=T} \left( c\frac{dy}{dt} \right) \frac{dy}{dt} dt \tag{A.4}$$

## A.2. CONTINUOUS SYSTEMS

In the previous section systems with a finite number of degrees of freedom have been assessed. In case of a structure having continuously distributed parameters. When a structure is looked at as a system with an infinite number of degrees of freedom we talk about a continuous system. Due to the infinite number of degrees of freedom a continuous system can vibrate in infinitely many different frequencies and mode shapes.

There are different theories on how to look at a beam under transverse loading, each with their own assumptions and rules of application. The most commonly used theory is the Euler Bernoulli beam theory. A key assumption in this theory is the negligence of shear deformation. As mentioned by Tieleman [6] shear deformations can be neglected for length over thickness ratios of 5:1 The governing equation for a Euler Bernoulli bending beam is written as:

The first five mode shapes relating to the first five frequencies of a simply supported beam are shown in figure A.3, in which both ends are simply supported.

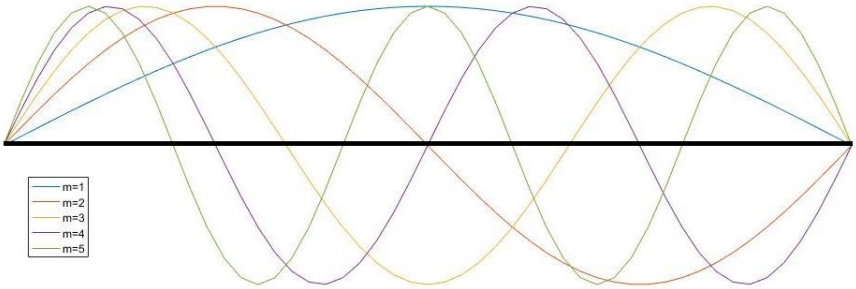


Figure A.3: First five mode shapes of a simply supported beam

As mentioned by Spijkers *et al.* [30] shear deformation is negligible for beams with high wave length over thickness ratios. Since higher vibration modes have smaller wave lengths the relative slenderness of the plate decreases for higher modes. This means that for higher modes shear deformation is not negligible any more. Spijkers *et al.* [30] mentioned that shear deformation will start to play a role for the following beam mode numbers:

$$n \leq \frac{2l}{5t} \quad or \quad \frac{l}{tn} \leq 2.5 \tag{A.5}$$

| | | | | |
|---|---|---|---|---|
| In which: | n | = | Beam mode number | [-] |
| | l | = | Length of the span. | [m] |
| | t | = | Thickness of the plate. | [m] |

## A.3. REWRITING OF CONTINUOUS SYSTEMS INTO 1-DEGREE OF FREEDOM SYSTEMS

Quite often people are only interested in the fundamental, e.g. first, natural frequency [30]. In this case quite often structures can be simplified to a system with one degree of freedom which has exactly the same fundamental frequency as the system with continuously distributed parameters. The distributed mass is concentrated in the point of interest, being the location of the degree of freedom of interest. First of all the stiffness of the structure is determined based on a concentrated load in the degree of freedom of interest using the so called "forget me nots" in structural mechanics. This is done by determining the relation: force over deflection or bending moment over rotation. Then the fundamental frequency of the continuous system is set equal to the fundamental frequency of the one degree of freedom system. Since the only unknown variable in the equation is the so called "equivalent mass" of the one degree of freedom system the value of the equivalent mass is found. A simple example will now be used to illustrate this equivalent mass.

A simply supported beam is analysed. The maximum deflection due to a concentrated load in the middle of a simply supported beam is equal to: $\delta_{max} = FL^3/(48EI)$ resulting in a stiffness of $k = 48EI/L^3$. When setting the fundamental frequency of the continuous system equal to the first (and only) natural frequency of the one degree of freedom system the following equation is obtained.

$$\pi^2 \sqrt{\frac{EI}{\rho L^4 th}} = \sqrt{\frac{48EI}{L^3 m^*}} \tag{A.6}$$

From this equation it follows that the equivalent mass, being $m^*$, is equal to: $m^* = 0.5\rho Lth$, being half of the total continuously distributed mass. The same can be done for structures with other boundary conditions or other degrees of freedom of interest. Figure A.4 shows three examples of boundary conditions and accompanying equivalent masses.

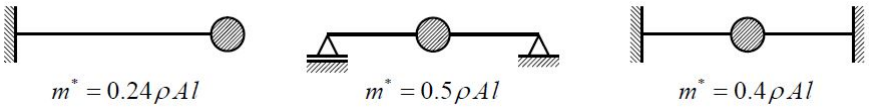


Figure A.4: Three examples of boundary conditions and accompanying equivalent masses [30]

# B

# A-Results of the research performed by Korevaar [4]

The results of the experiments concerning the rectangular shaped seal performed by Korevaar [4] are shown in table B.1 until table B.5. The final column represents the presence of a clear peak in the frequency domain in the following variables: vertical vibration amplitude, $\delta y$, pressure, p, and force, F. The following gradation is used:

- 1: Clear peak in all measured variables;
- 2: Clear peak in one or two of the measured variables;
- 3: No clear peak at all.

Figure B.1 is used to illustrate the meaning of the presence of peaks in the frequency domain, in which $G_{xx}$ is a dimensionless measure of the energy for a frequency spectrum.

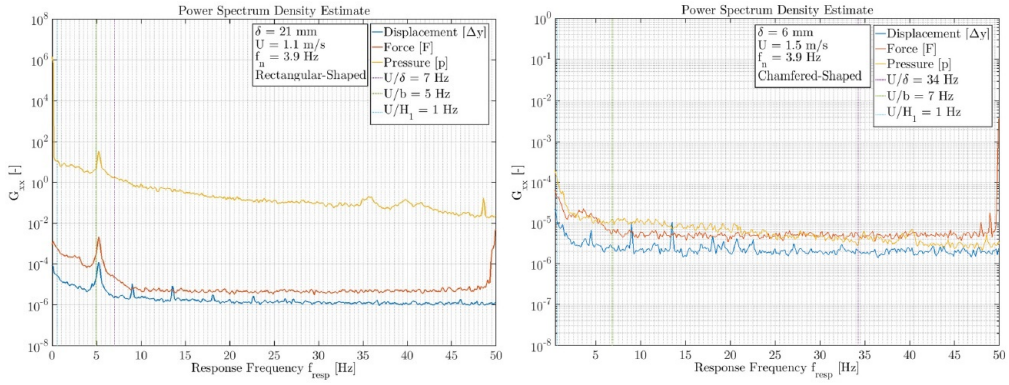


Figure B.1: (L) Clear peaks in all variables & (R) No clear peak in any of the variables [4]

H means that the vibrations occurred in the high frequency domain, being between 15 and 40 Hertz. Absence of H means that occurring vibrations had a frequency between 0 and 15 Hertz.

Table B.1: Results [4] for experiments conducted with a suspension stiffness of 1.16 N/mm

| **Gate Opening $\delta$ [mm]** | **Downstream Water Level H2 [mm]** | **Upstream Water Level H1 [mm]** | **Peak** |
|---|---|---|---|
| 13 | 178 | 292 | 1 H1 |
| 15 | 185 | 330 | 3 |
| 11 | 163 | 217 | 3 H1 |
| 10 | 151 | 171 | 3 |
| 28 | 158 | 172 | 3 |
| 31 | 186 | 246 | 1 |
| 33 | 206 | 321 | 3 |
| 46 | 208 | 274 | 3 |
| 48 | 221 | 318 | 3 |
| 50 | 231 | 360 | 3 |
| 44 | 165 | 176 | 3 |

Table B.2: Results [4] for experiments conducted with a suspension stiffness of 5.43 N/mm

| **Gate Opening $\delta$ [mm]** | **Downstream Water Level H2 [mm]** | **Upstream Water Level H1 [mm]** | **Peak** |
|---|---|---|---|
| 31 | 161 | 275 | Failed |
| 31 | 212 | 321 | 1 |
| 30 | 201 | 271 | 1 |
| 30 | 188 | 222 | 1 |
| 21 | 187 | 244 | 1 |
| 19 | 155 | 218 | 1 |
| 19 | 167 | 281 | 2 (F,P) |
| 20 | 199 | 304 | 1 |
| 22 | 214 | 289 | 1 |
| 21 | 222 | 341 | 1 |
| 22 | 229 | 370 | 3 |
| 8 | 204 | 350 | 3 |
| 8 | 176 | 351 | 3 |
| 6 | 136 | 218 | 3 |
| 7 | 203 | 241 | 3 |
| 51 | 233 | 248 | 3 |
| 52 | 224 | 271 | 1 |
| 52 | 199 | 282 | 1 |
| 31 | 203 | 255 | 1 |
| 31 | 192 | 217 | 1 |

Table B.3: Results [4] for experiments conducted with a suspension stiffness of 15.66 N/mm

| **Gate Opening $\delta$ [mm]** | **Downstream Water Level H2 [mm]** | **Upstream Water Level H1 [mm]** | **Peak** |
|---|---|---|---|
| 45 | 193 | 226 | 3 |
| 46 | 208 | 279 | 2 (F,P) |
| 46 | 231 | 365 | 2 (F,P) |
| 15 | 189 | 345 | 3 H1 |
| 15 | 172 | 238 | 2 (F,P),H1 |
| 15 | 157 | 184 | 1 |
| 27 | 146 | 171 | 3 |
| 27 | 176 | 211 | 1 |
| 27 | 207 | 365 | 3 |

Table B.4: Results [4] for experiments conducted with a suspension stiffness of 43.20 N/mm

| **Gate Opening $\delta$ [mm]** | **Downstream Water Level H2 [mm]** | **Upstream Water Level H1 [mm]** | **Peak** |
|---|---|---|---|
| 23 | 192 | 231 | 1 |
| 23 | 192 | 231 | 1 |
| 22 | 203 | 275 | 1 |
| 24 | 214 | 333 | 2 (F,P) |
| 11 | 181 | 332 | 2 (F,P),H1 |
| 11 | 173 | 281 | 3 H1 |
| 12 | 158 | 204 | 3 |
| 11 | 148 | 167 | 3 |
| 40 | 178 | 203 | 3 |
| 39 | 194 | 241 | 2 (F,P) |
| 39 | 209 | 300 | 2 (F,P), H2 |
| 38 | 216 | 333 | 2 (F,P) |

Table B.5: Results [4] for experiments conducted with an infinitely stiff suspension

| **Gate Opening $\delta$ [mm]** | **Downstream Water Level H2 [mm]** | **Upstream Water Level H1 [mm]** | **Peak** |
|---|---|---|---|
| 40 | 177 | 196 | - |
| 40 | 196 | 255 | - |
| 40 | 219 | 356 | - |
| 40 | 208 | 298 | - |
| 25 | 204 | 365 | - |
| 25 | 184 | 247 | - |
| 25 | 161 | 179 | - |
| 13 | 161 | 205 | - |
| 13 | 173 | 262 | - |
| 13 | 184 | 337 | - |
| 13 | 155 | 186 | - |
| 9 | 159 | 209 | - |
| 9 | 179 | 332 | - |

# C

# RESEARCH ON VERTICAL GATE VIBRATIONS PERFORMED BY ERDBRINK [7]

For this research two profiles have been tested in both a physical scale model and a Computational Fluid Dynamics (CFD) model, being a basic rectangular profile and an adapted profile with ventilation slots. The adapted profile resulted in much lower reduced velocities. Flow patterns are shown in figure C.1.

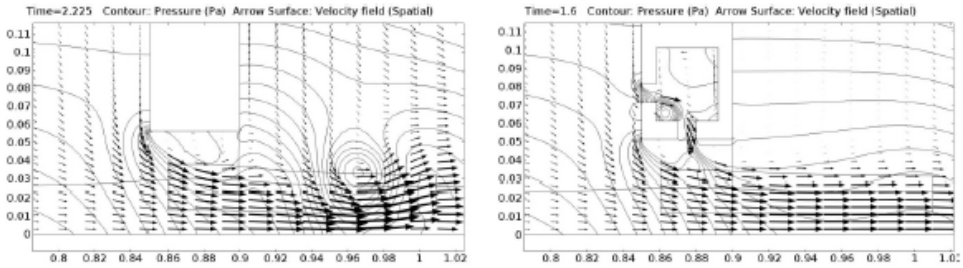


Figure C.1: CFD plots of the two different profiles [7]

In order to solve his hydraulic engineering problem Erdbrink [7] uses a framework to prepare the model or come to the right model choice. The framework as proposed by Erdbrink [7] is visualised as showed in figure C.2. This framework can be quite useful for the modelling of the case study as will be performed in this thesis on FRP hydraulic structures.

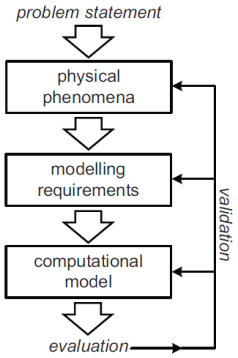


Figure C.2: CFD Framework as proposed by Erdbrink [7]

First of all the physical problem is identified after which a number of questions are stated which summarise the problem, this is called the problem statement. As mentioned by Erdbrink [7] three questions are interesting for a hydraulic gate, being:

- What are the maximum dynamic forces experienced by the gate?
- Given a set of flow conditions and gate positions, will the gate start vibrating or not?
- Which excitation mechanism can be expected to occur?

As stated by Erdbrink [7] the classes of physical phenomena in the case of a vibrating gate are: the influence of the free surface, turbulence and moving objects. Scales also come into play. Detail hydrodynamics are situations in which fluid dynamics occurs in a small volume and in which the flow length scales approximately the same in all three directions. In this case the pressure is not hydrostatic and the streamlines are not parallel. Flow around a structure is a part of the detail hydrodynamics while also being influenced by large scale conditions away from the structure.

Modelling requirements are set up based on the most important physical aspects and their level of detail in order to obtain a model which can provide a tailor made answer to the problem statement. Parametrisation is applied to simplify reality by using average values or estimations rather than the real physical quantity. The modelling requirements are proposed below by Erdbrink [7]. Crucial choices are made in the third, fourth and fifth modelling requirements.

**1: Time dependency.** Steady-state flow equations suffice in case of a static gate which experiences a quasi-stationary flow around the structure. In case of a moving gate the flow and therefore fluid-structure interaction becomes time-dependent.

**2: What is the degree of non-hydrostaticity?** Non-hydrostatic pressures occur in the recirculation zone behind the structure and in the contraction underneath the construction, resulting in the invalidity of the shallow-water equations due to their simplification concerning vertical acceleration. A 2D gate model may as well result in the underestimation of the turbulence, due to the absence of a turbulent velocity in the horizontal plane perpendicular to the flow direction, but is still an accurate model. A 3D model is capable to include this but the increase of computational costs outweighs its benefits when compared to a 2D model.

**3: How important is the free surface?** In case of a situation in which only fully submerged flow occurs and wave radiation is negligible, fluctuations of the free surface are not required to be modelled. This simplification is less applicable to situations with increasing Froude numbers.

**4: To which level of detail should turbulent effects be simulated?** The flow around a gate always includes turbulence. On the other hand turbulence is not a part of the mechanisms which result in strong vibrations. Therefore, it is important to consider the level of detail of turbulence modelling.

**5: Moving object.** The moving object, being modelled as a one degree of freedom system, vibrates at a certain frequency which influences the required number of time steps in order to get reliable results.

**6: What kind of boundary conditions are required?** According to Erdbrink [7] the lower boundary is best modelled as a rough wall, the upper boundary is modelled as a free surface, the upstream boundary is best modelled as a velocity profile and the downstream boundary condition is a hydrostatic pressure distribution. The upstream and downstream boundary conditions should be out of range of local disturbances.

The possible computational tools are determined for the case at hand. In this case a computational model is chosen in the form of a CFD model which includes detail hydrodynamics and more specifically the interaction between the vibrating gate and the flow. The benefits of a model with a high level of detail or short computational time should always be weighed.

In case of a successful numerical model run usable answers to the problem statement can be obtained. In order to obtain a reliable model one is required to go trough an iterative loop using the validation of all steps in the framework. It is checked whether or not the steps as mentioned in the framework are implemented in a correct manner, which is called verification. Calibration of the model is performed in order to prepare a model for a particular application.

# D

# VALIDATION AND SENSITIVITY ANALYSIS OF THE CFD MODEL

## D.1. VALIDATION OF THE CFD MODEL

### D.1.1. DESCRIPTION OF THE THREE GAP RATIO RANGES

#### SMALL GAP RATIOS

For small gap ratios (approximately: $s/d \leq 0.5$) the following is described by Thang and Naudascher [3]:

- Flow separation and stable reattachment at the underside of the hydraulic gate;
- An under pressure is present in the area between separation and reattachment.

Figure D.1 shows the flow velocity field for an intermediate gap of 1.5 centimetres (gap ratio of 0.3). Flow directly behind the gate moves in a downward direction.

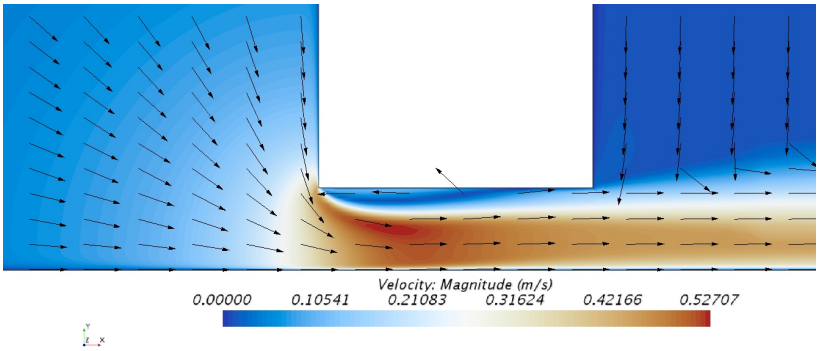


Figure D.1: Plot of the flow velocity for a gap of 1.5 centimetres (s/d = 0.3)

FigureD.2 shows positive flow velocities from the left side to the right side. White indicates that the flow direction is from right to left. In this manner the separation of the flow and the back flow can be shown.

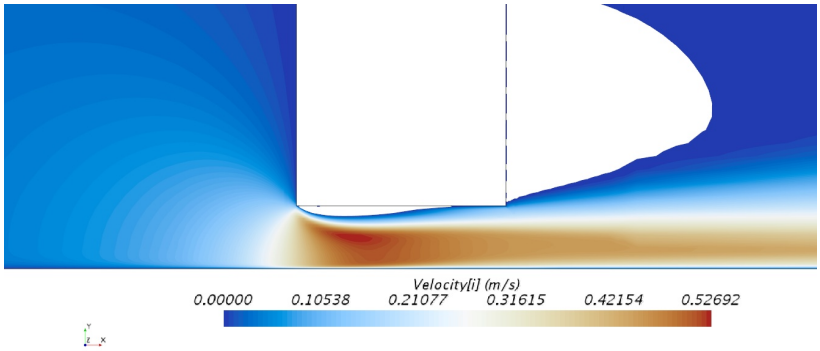


Figure D.2: Plot of the positive x-components of the flow velocity for a gap of 1.5 centimetres (s/d = 0.3)

Figure D.2 shows the separation of the streamline and reattachment further on at the underside of the hydraulic gate, agreeing with findings in Thang and Naudascher [3].

Figures D.3 shows the pressure distribution along the underside of the hydraulic gate. Due to large streamline curvature a large under pressure is generated after the point of separation. This relative under pressure is decreased along the underside of the hydraulic gate and can be seen due to the fact that the pressure builds up.

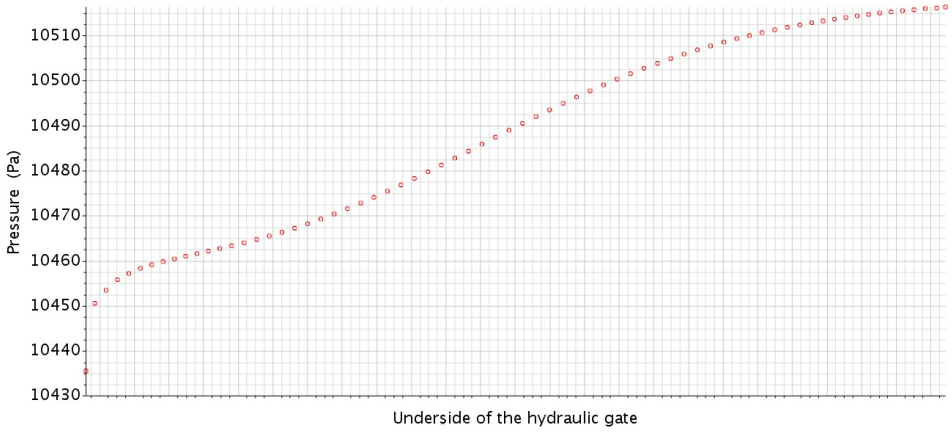


Figure D.3: Pressure distribution along the underside of the gate for a gap of 1.5 centimetres (s/d = 0.3)

### INTERMEDIATE GAP RATIOS

For intermediate gap ratios (approximately: $0.5 \leq s/d \leq 2$) the following is described by Thang and Naudascher [3]:

- A transitional state between complete flow separation and reattachment occurs. The separated layer passes close by the underside of the gate.

Figure D.4 shows the flow velocity field for an intermediate gap of 3.75 centimetres (gap ratio of 0.75). It can also be seen that return flow in the bore enters the area of relative under pressure underneath the gate. The flow directly behind the gate therefore approaches the underside of the hydraulic gate under an angle.

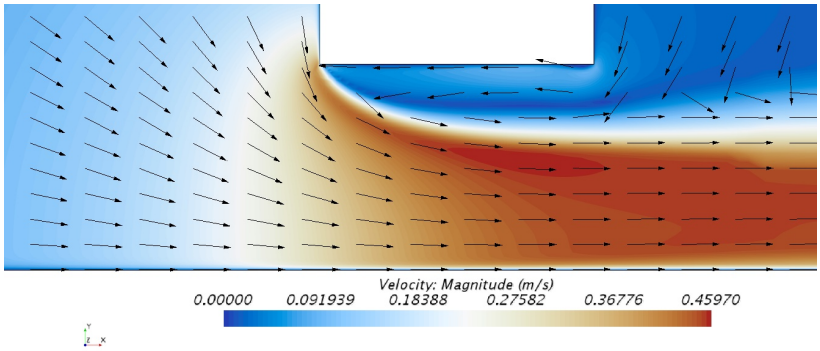


Figure D.4: Plot of the flow velocity for a gap of 3.75 centimetres (s/d = 0.75)

Figure D.5 indeed shows that the separated layer passes close by the underside of the hydraulic gate. Also the area of negative horizontal flow velocity, being a velocity directed to the left, becomes larger than for a smaller gap (figure D.2)

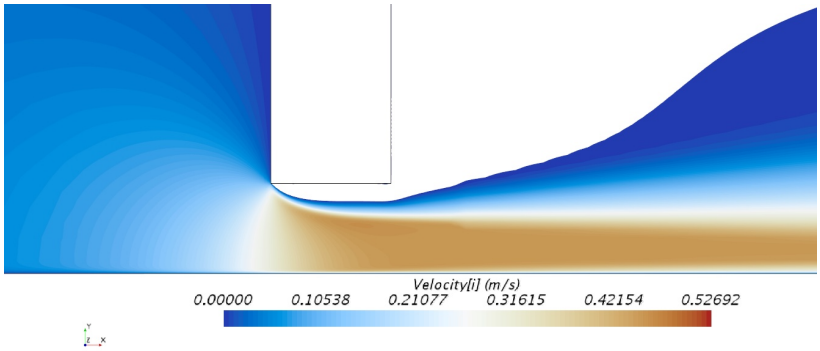


Figure D.5: Plot of the positive x-components of the flow velocity for a gap of 3.75 centimetres (s/d = 0.75)

Figure D.6 shows that the pressure distribution underneath the hydraulic gate is already quite equalised along the bottom of the hydraulic gate, albeit not as constant as the pressure distribution for large gap ratios (section D.1.1).

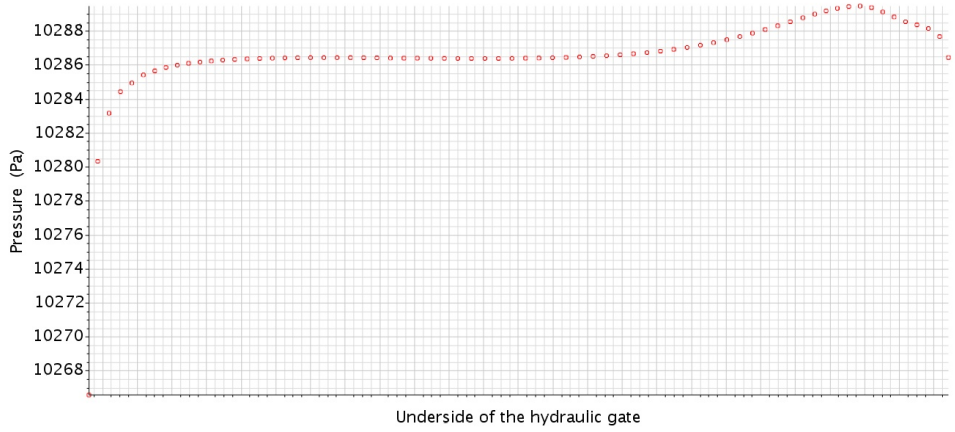


Figure D.6: Pressure distribution along the underside of the gate for a gap of 3.75 centimetres (s/d = 0.75)

### LARGE GAP RATIOS

For large gap ratios (approximately: $2 \leq s/d$) the following in described by Thang and Naudascher [3]:

- Complete flow separation takes place;
- Equalisation of pressures underneath and behind the gate occurs.

Figure D.7 shows the flow velocity field for a large gap of 25 centimetres (gap ratio of 5).

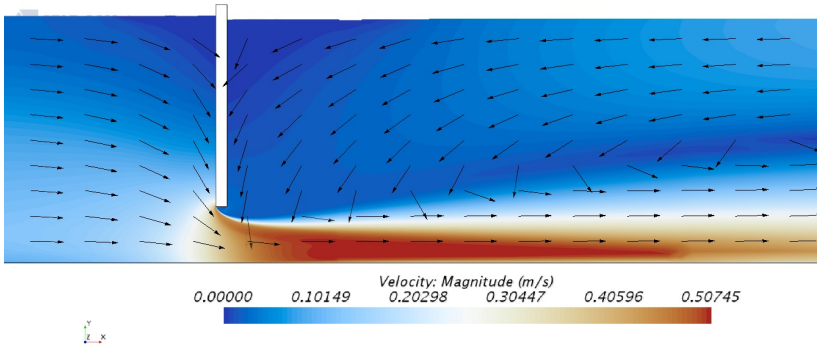


Figure D.7: Plot of the flow velocity for a gap of 25 centimetres (s/d = 5)

Agreeing with findings of Thang and Naudascher [3] figure D.8 indeed shows that complete flow separation is present. Also the size of the bore is further increased when compared to flow velocity fields of the smaller gap ratios.

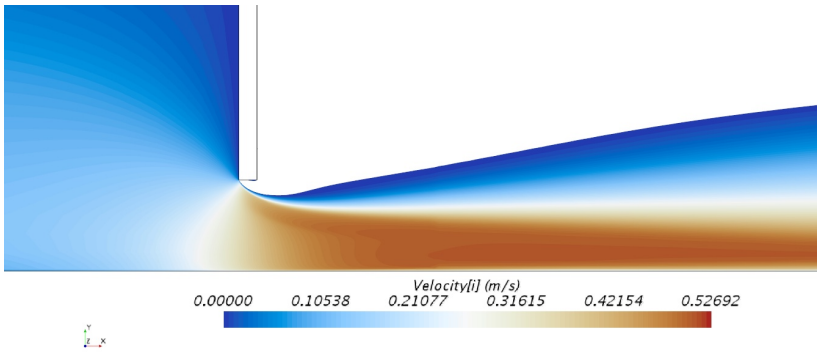


Figure D.8: Plot of the positive x-components of the flow velocity for a gap of 25 centimetres (s/d = 5)

Figure D.9 shows the pressure distribution at the underside of the hydraulic gate. These findings coincide with the description of Thang and Naudascher [3], being that the pressures are pretty much equalised over the complete underside of the hydraulic gate.

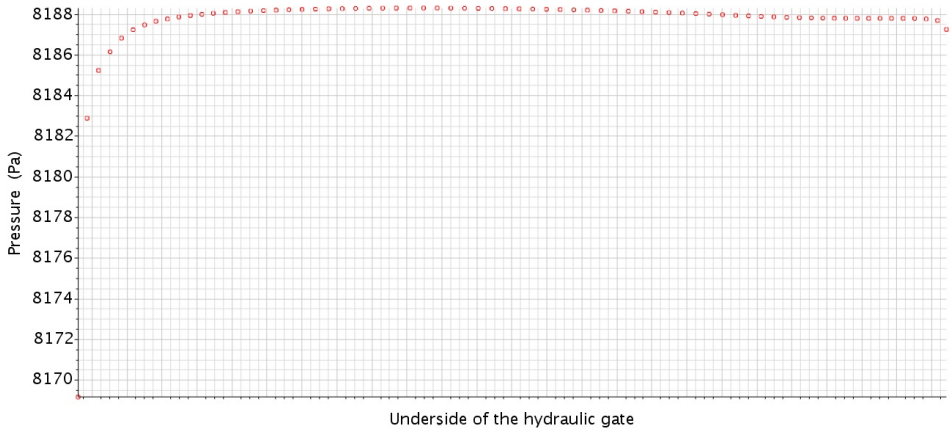


Figure D.9: Pressure distribution along the underside of the gate for a gap of 25 centimetres (s/d = 5)

## D.2. SENSITIVITY ANALYSIS

Since not all results of the CFD computations comply with results in Thang and Naudascher [3], it is important to check possible reasons for deviations from the experimental results. Possible explanations for the differences in the experimentally found $C_L$-curves and the ones found using CFD can be sought for in the sensitivity of the formula which is used to compute the lift coefficient, presented again in equation D.1.

$$C_L = \frac{1}{d}\int_{x=0}^{d} \frac{h_i - h_2}{h_1 - h_2}\,dx \tag{D.1}$$

It is clear to see that there are a few parameters in which uncertainties may be present. The only parameter of which one can be certain is the thickness of the hydraulic gate. There may be uncertainties in $h_i$, $h_1$ and $h_2$. These are elaborated in the following paragraphs.

### D.2.1. UNCERTAINTIES IN $h_i$

Thang and Naudascher [3] have used five pressure sensors for the determination of the pressures and therefore the computation of the $C_L$-values. In the CFD computations the pressure is measured for around fifty cells, deviations of the pressure over the gate underside are therefore more accurately measured. Since $h_i$ is in the numerator, the found local piezometric head influences the sign of $C_L$.

### D.2.2. UNCERTAINTIES IN $h_2$

Since the downstream water level is used twice in equation 5.12, the influence of an inaccuracy of this downstream water level greatly influences the resulting $C_L$-curve. Since $h_2$ is part of the numerator, it has an influence on the sign of the resulting value of $C_L$.

As mentioned in Thang and Naudascher [3] the downstream water level, being $h_2$ is measured approximately fifteen centimetres from the gate. In order to check the influence of the exact location at which the measurements are performed, the downstream water level is measured at two other distances downstream of the gate. The $C_L$-values for different gaps and positions of measurements in CFD are shown in figure D.10.

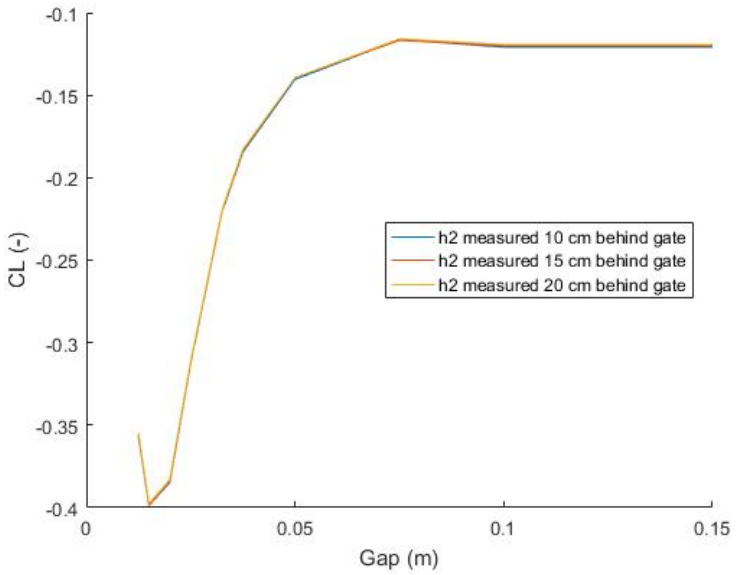


Figure D.10: $C_L$-values for different positions of $h_2$

Since the results are practically the same for different locations of $h_2$ a relative $C_L$-value plot is shown in figure D.11. $C_L$-values of the previous plot are now divided by the $C_L$-value at the location at which $h_2$ is measured, being fifteen centimetres downstream of the gate.

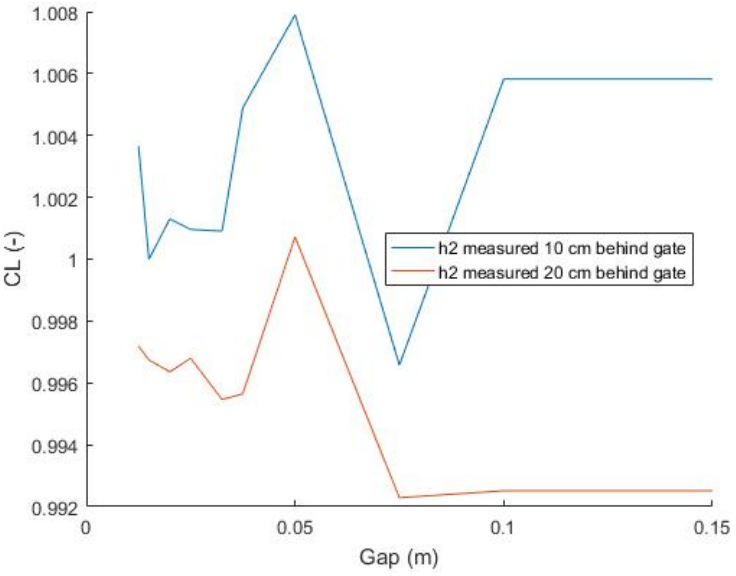


Figure D.11: Relative $C_L$-values for different positions of $h_2$

### D.2.3. UNCERTAINTIES IN $h_1$

The measured upstream water level, $h_1$, has only got a limited influence since an error in measuring $h_1$ may only result in a scaling of the $C_L$-value and can not possibly result in a switch of sign. It is therefore not the main concern to research this issue, although it is interesting to check the influence of the position at which this $h_1$ is measured. This is the case since the location of measuring the upstream water level, $h_1$, is not mentioned in Thang and Naudascher [3].

The following figure shows the influence of the location of measuring the upstream water level on the outcome of the lift coefficient.

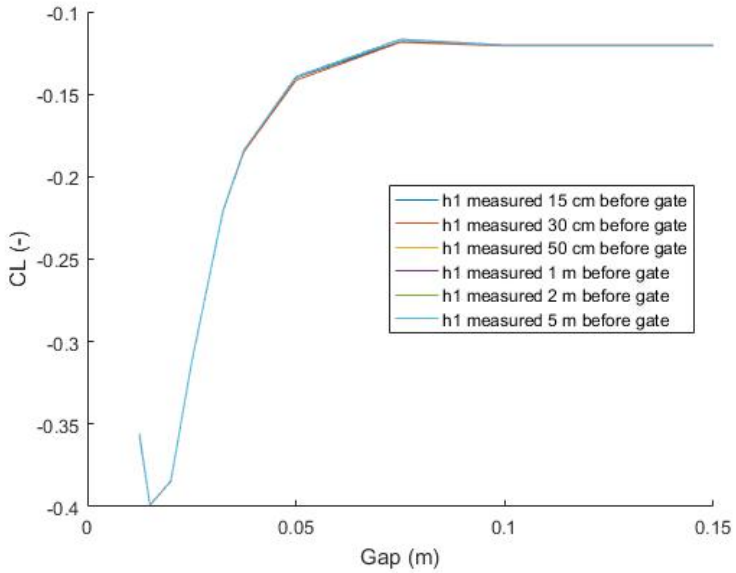


Figure D.12: $C_L$-values for different positions of $h_1$

As for different location of measuring the downstream water level in figure D.10, no real difference between the resulting $C_L$ can be distinguished. $C_L$-values as a function of the gap, from the previous plot, are now divided by the average $C_L$-values of all different locations of the measured $h_1$.

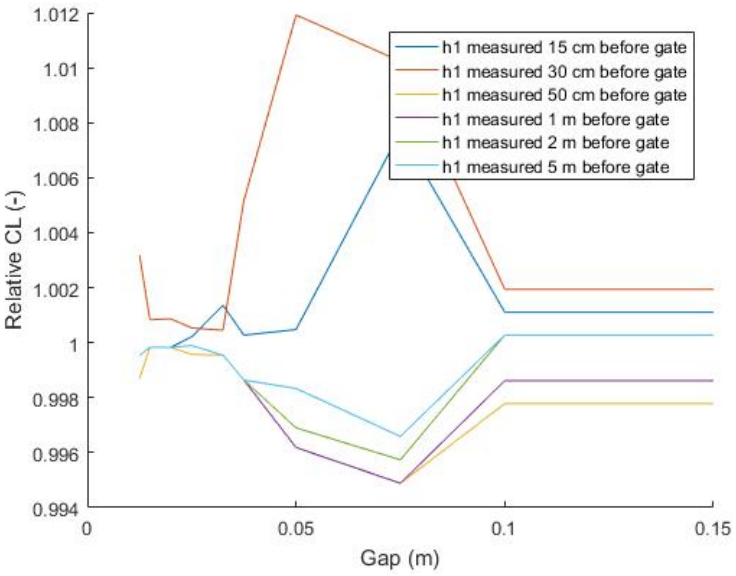


Figure D.13: Relative $C_L$-values for different positions of $h_1$

Since differences between $C_L$-values for different locations of the measured $h_1$ are not larger than 0.12 % one can conclude that measuring the $h_1$ at different locations does not significantly influence the outcome of the $C_L$-plots, which is an expected result.

# E

# FINAL MODEL SET UP

## E.1. HYDRAULIC HEAD

Since the simulated vertical velocity depends on the angle of inclination of the hydraulic gate and the flow velocity an increase of the flow velocity, by means of an increase of the hydraulic head, results in a larger simulated vertical velocity. Therefore, a larger range of vertical gate velocities can be simulated using MATLAB.

Summarised it means that small inclinations of the hydraulic gate and large flow velocities are desirable. An important note is that an increased flow velocity up to a value resulting in shooting water, for $Fr = V/\sqrt{hg} \geq 1$, has a large influence on fluctuating forces on the bottom of the hydraulic gate. Since a time average, over twenty seconds, is used for the computation of the forces, too large force fluctuations may occur due to the occurring bore, resulting in inaccurate post-processing.. An example of the velocity field for shooting water is shown in figure E.1 with an accompanying time dependent force in figure E.2. The upstream water level is equal to two metres whereas the downstream water level, being $h_2$, is equal to one metre. For the downstream part of the domain a the wave celerity, being $c_2$, can become:

$$c_2 = \sqrt{gh_2} = \sqrt{9.81} = 3.13[m/s] \tag{E.1}$$

The flow velocity of around five metres per second is therefore large enough to create a critical flow regime.

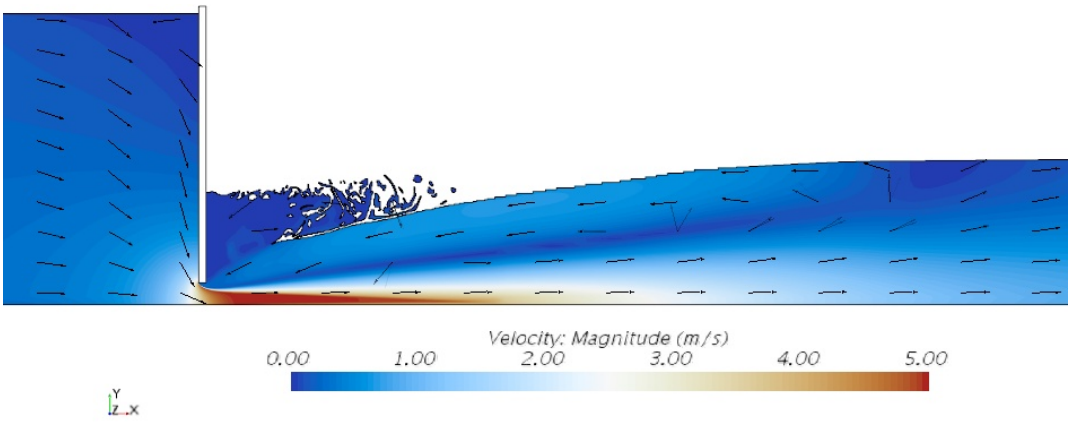


Figure E.1: An example of the velocity field for critical flow ($Fr \geq 1$)

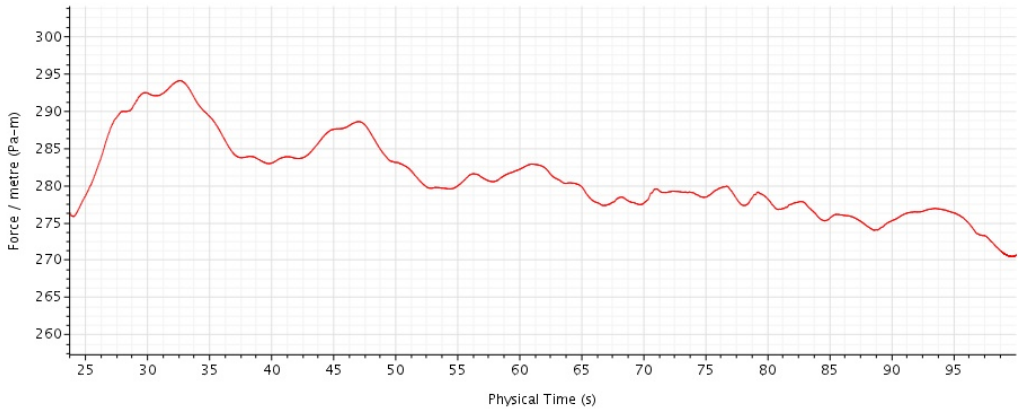


Figure E.2: An example of occurring forces for critical flow ($Fr \geq 1$)

It is clear that the force acting on the bottom of the hydraulic gate is not steady although the model has been converged in terms of the discharge at the inlet and outlet. The hydraulic head is chosen such that the Froude number stays below one.

A hydraulic head of ten centimetres is chosen with an upstream water level of one metre and ten centimetres and a downstream water level of one metre. A hydraulic head will result in an approximate flow velocity in the Vena Contracta of:

$$V = \sqrt{2g0.1} = 1.4[m/s] \tag{E.2}$$

## E.2. OPENING HEIGHTS

The CFD model is run for a number of opening heights in combination with certain inclination angles. The critical opening height is equal to 0.65 times the thickness of the hydraulic gate, as mentioned in Thang and Naudascher [3], being 3.25 centimetres for a hydraulic gate of five centimetres thick. Finding the upward forces acting on the bottom of the hydraulic gate for opening heights close to this critical opening height is therefore of great importance. When combining the knowledge that the lift coefficient becomes constant for larger opening heights and independent of the vertical velocity of the hydraulic gate one can conclude that the most interesting gap heights are below fifteen centimetres, being a gap ratio of three. Beyond a gap ratio of three the lift coefficient becomes practically independent of the gap and vertical velocity of the hydraulic gate.

## E.3. HYDRAULIC GATE INCLINATIONS

For the validation of the model in chapter 5 a water level difference of eleven millimetres was used. A large inclination of the hydraulic gate, in order to mimic the vertical velocity of the hydraulic gate, may result in flow patterns which do not agree with reality. The inclination of the hydraulic gate has the largest impact on the smaller gate opening ratio (gap/thickness) since a inclination of the hydraulic gate results in a larger relative decrease of the discharge. This has to do with the rotation of the hydraulic gate squeezing the flow through a narrower gap. The inclinations of the hydraulic gate should therefore be kept to a minimum. An inclination angle of two degrees for a gate thickness of five centimetres will result in a reduction of the gap of:

$$\delta gap = \frac{d}{2} tan(\frac{2\pi}{180}) = 0.87[mm] \tag{E.3}$$

The relative decrease of the effective gap is the most for the smallest gap, being 7.5 millimetres. The relative decrease of the effective gap in that case is equal to: $(1-(7.5-0.87)/7.5) * 100\% = 11.6\%$. Which is expected to be small enough to obtain realistic results. Figure E.3 illustrates the influence of the gate inclination inclination on the change of the gap. The inclination angles of the HG are chosen to be: $-2°, -1°, 0°, 1°, 2°$.

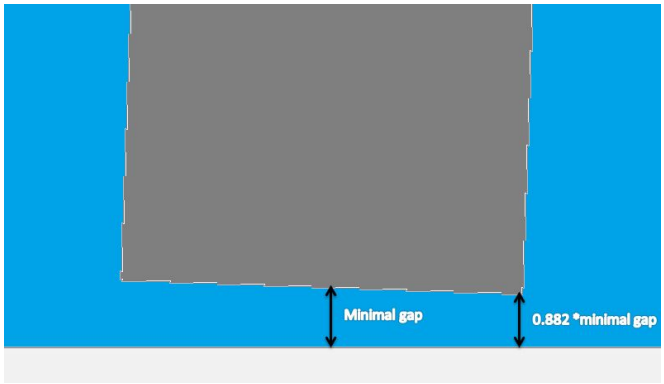


Figure E.3: Example of maximum decrease of the smallest gap

## E.4. BOUNDARIES OF THE GAPS AND VERTICAL GATE VIBRATION VELOCITY

An inclination angle of two degrees combined with the flow velocity of 1.4 metres per second results in a maximal absolute vertical hydraulic gate velocity of:

$$\frac{dy}{dt}_{max-absolute} = V\,tan(\frac{2\pi}{180}) = 1.4\,tan(\frac{2\pi}{180}) = 0.05[m/s] \tag{E.4}$$

In other words, upward forces on the bottom of the hydraulic gate can be simulated for vertical velocities up to 0.05 metres per second.

Opening heights are chosen between 0.75 centimetres and 30 centimetres for the thin gate (5 centimetres thick) and between 1.5 centimetres and 30 centimetres for the thick gate (10 centimetres thick).

Combining the opening heights and vertical velocities one can conclude that upward forces can be computed for the following ranges:

$$0.75\ cm \leq gap \leq 30\ cm \tag{E.5}$$

and

$$-0.05\ m/s \leq \frac{dy}{dt} \leq 0.05\ m/s \tag{E.6}$$

# F

# NOTES REGARDING CFD COMPUTATIONS

## F.1. REGARDING ACCURATE RESULTS

It is important go have a fine mesh in regions of great importance: in the gap, at point of separation, locations of water levels. Especially the water levels close to the gate are important, since an accurate simulation of the water levels results in accurate pressures underneath the gate and therefore an accurate computation of the lift coefficient.

Having a fine mesh at the water level does not contribute to accurate results for situations at which the computed water level falls beyond the limits of the this fine mesh.

## F.2. REGARDING EFFICIENT COMPUTATIONS

### F.2.1. MESH

A finer mesh will produce more accurate results, such as a better prediction of the separation layer, but will result in more cells and therefore a larger computation time with respect to a courser mesh. Another disadvantage of having a finer mesh is that the Courant number increases for a finer mesh, resulting in a required decrease of the computational time steps, which on its turn increases the time required for computations. The Courant number depends on the cell size, time step and flow velocity in a cell. As an example: keeping the same Courant number for a twice as fine mesh will result in a halving of the required time step.

Only apply a fine mesh when necessary. A fine mesh in regions at which a course mesh does not (significantly) influence results at the location of interest or at which no large deviations are occurring, such as curvature of streamlines, will only unnecessarily slow down computations.

### F.2.2. INITIAL CONDITIONS

By choosing initial conditions as close to the final results as possible one can significantly decrease the required computational time. Initial conditions include:

**Initial velocity.** This is based on the expected velocity in the domain for a certain head difference, contraction coefficient, gap height and water level. Since the water levels upstream and downstream are almost equal the initial velocity is set for the whole domain;

**Initial volume fraction.** Setting the initial volume fraction of water equal to one for the expected water column for two areas: upstream and downstream;

**Initial pressure.** Setting the initial pressure equal to the static pressure for the expected water depths for two areas: upstream and downstream.

An even faster convergence can be achieved by dividing the domain in two areas: upstream and downstream or even three areas: upstream, downstream and underneath the gate.

#### INFLUENCE OF AN INITIAL VELOCITY ON THE CONVERGENCE OF THE SIMULATION

Figure F.1 shows a plot of the relative specific discharge at the inlet and the influence of an initial velocity on the convergence for a gap of 1.25 centimetres. The relative specific discharge is determined by dividing the specific discharge at a certain time by the time-averaged discharge.

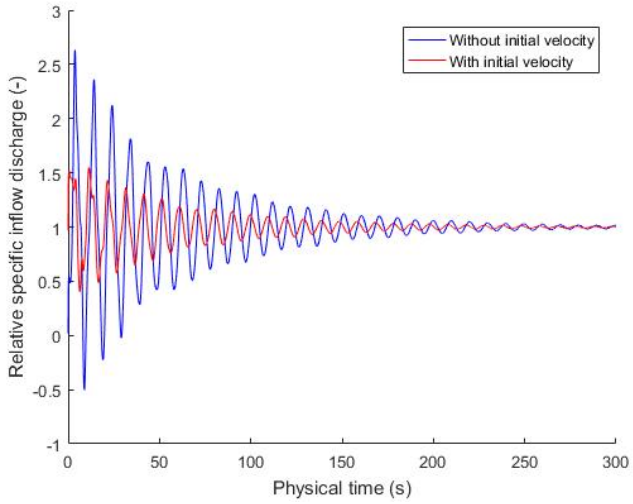


Figure F.1: Plot of the relative specific discharge at the inlet for the situation with and without initial velocity for a gap of 1.25 cm

It is clear to see that adding an initial velocity, close to the final velocity, to the computation has a large effect on the convergence of the simulation. The specific discharge at the inlet for the situation without initial velocity has a maximum equal to 2.5 times the eventual discharge. For the case including an initial velocity this is only 1.5 times.

Figure F.2 shows a similar plot of the convergence for the situation with and without estimated final velocity as an initial condition for a gap of 15 centimetres.

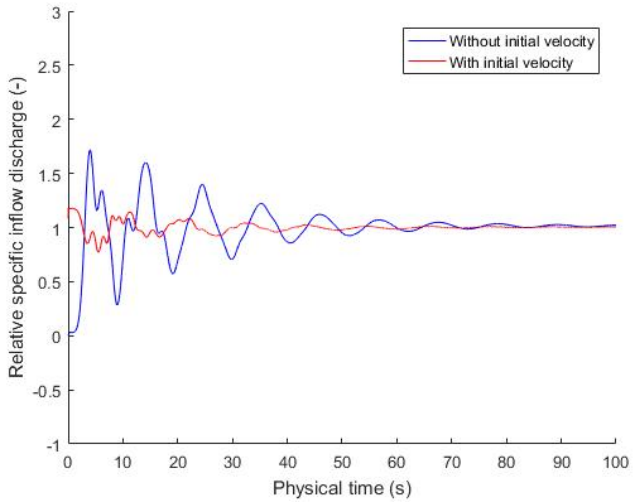


Figure F.2: Plot of the relative specific discharge at the inlet for the situation with and without initial velocity for a gap of 15 cm

When comparing figure F.1 to F.2 it seems that the initial velocity has a larger influence on the convergence of the large gap than the small gap, presumably since the final flow velocity of the situation with the large gap is larger than the final velocity for the situation with the small gap, due to a difference in discharge.

Another difference is that the maximum discharge at the inlet is only 1.7 times larger than the eventual discharge at the inlet for the case without initial velocity, while this was 2.5 times for the gap of 1.25 centimetres. For the situation with initial velocity the fluctuating discharge has a maximum of only 1.2 times the averaged discharge at the inlet.

Figure F.3 shows a plot of the relative specific discharge at the inlet for both a gap of 1.25 centimetres as 15 centimetres for the situation without initial velocity.

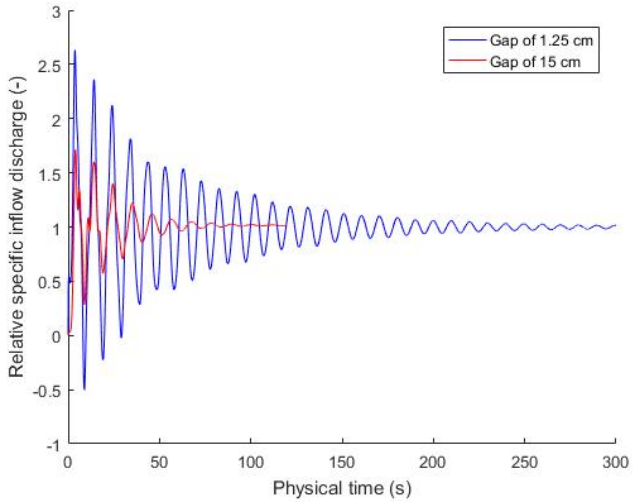


Figure F.3: Plot of the relative specific discharge at the inlet for the situation without initial velocity for two gaps

One can conclude that the simulation with a gap of 15 centimetres has a much faster convergence than the simulation with a gap of 1.25 centimetres. The simulation with the large gap has already converged after around 100 seconds of physical time while the simulation with the small gap is not fully converged after 300 seconds.

Figure F.4 shows a plot of the specific relative discharge at the inlet for the simulation including an initial velocity close to the final velocity.

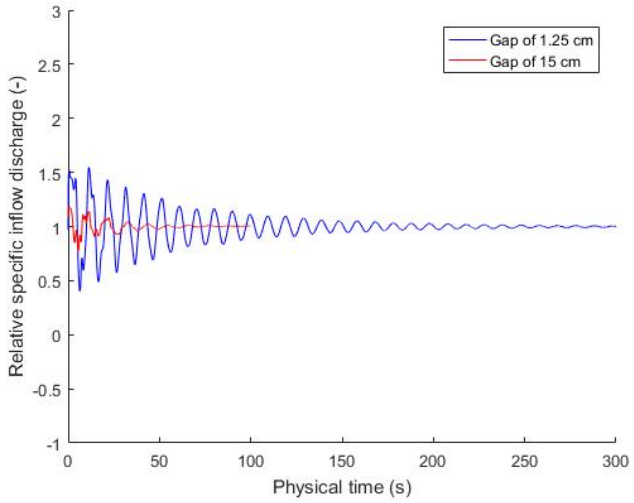


Figure F.4: Plot of the relative specific discharge at the inlet for the situation with initial velocity for two gaps

Figure F.4 and F.3 show similar behaviour regarding the influence of an initial velocity close to the estimated final velocity. When including an initial velocity close to the estimated final velocity the amplitude of the relative discharge at the inlet is dramatically decreased for both gaps. The speed of convergence for the small gap is not really different for the situation with an initial velocity close to the estimated final velocity.

### F.2.3. COMPUTATIONAL POWER PER SIMULATION

It is also important to note that an increase of the number of cores active on a computation does not linearly decrease the computational time. There is a certain minimum number of cells required for each core to be efficient. One can understand that having ten nodes, consisting of four cores each, working on a small-scale two-dimensional model would not be an efficient use of resources.

Research performed by Star-CCM+ has shown that having less than 20,000 cells per core will result in a decrease of efficiency per core. More cores, with less than 20,000 cells each, will still decrease the simulation time up to a certain point where the coupling between the used cores takes more time than the decrease in simulation time due to the decrease of the number of cells per core.

In a simulation consisting of approximately 50.000 cells, using eight nodes resulted only in a fourty percent decrease of the computational time compared to a similar simulation using two nodes whereas a linear relation should have resulted in a seventy-five percent decrease.

In another simulation the mesh consisted of approximately 40,000 cells. Using two nodes around seventy-five percent of the computational time was required when compared to a simulation using only one node. A linear relation should have resulted in a fifty percent decrease of the computational time.

Clearly the efficiency per core decreases rapidly for a decreasing number of cells per core.